

# Minimally Invasive Instrument for In Vivo Measurement of Solid Organ Mechanical Impedance

by

Mark Peter Ottensmeyer

B.Eng.Mgt Mechanical Engineering  
McMaster University, 1994

M.S. Mechanical Engineering  
Massachusetts Institute of Technology, 1996

Submitted to the Department of Mechanical Engineering  
in partial fulfillment of the requirements for the degree of

Doctor of Philosophy in Mechanical Engineering

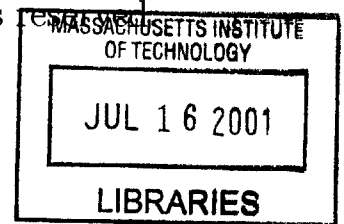
at the

MASSACHUSETTS INSTITUTE OF TECHNOLOGY

February 2001

**BARKER**

© Massachusetts Institute of Technology 2001. All rights reserved.



Author .....

Department of Mechanical Engineering  
January 11, 2001

Certified by...  
Dr. J. Kenneth Salisbury, Thesis Supervisor  
Principal Research Scientist, Mechanical Engineering, MIT  
Professor, Departments of Computer Science and Surgery, Stanford

Accepted by .....  
Prof. Ain A. Sonin  
Chairman, Committee on Graduate Students



# Minimally Invasive Instrument for In Vivo Measurement of Solid Organ Mechanical Impedance

by

Mark Peter Ottensmeyer

Submitted to the Department of Mechanical Engineering  
on January 11, 2001, in partial fulfillment of the  
requirements for the degree of  
Doctor of Philosophy in Mechanical Engineering

## Abstract

The medical field, and surgeons in particular, are turning to engineers to develop systems that help them learn their craft better. Mannequin-based systems, animal labs and surgery on cadavers each have drawbacks that could be addressed through realistic computer-based surgical simulation systems. To generate a simulation that includes both tactile/haptic and visual feedback, one must know what the material properties of tissue are, so that a finite element or other model can generate the proper predictions for interactions between surgical instruments and tissue.

This thesis presents the design, construction, characterization, and use of a minimally invasive surgical instrument designed to measure the linear visco-elastic properties of solid organs. The Tissue Material Property Sampling Tool, or TeMPeST 1-D, applies a small amplitude vibration normal to the surface of an organ such as liver or spleen, and records the applied force and displacement. It has a range of motion of up to 1mm, and can apply up to 300mN force with a 5mm right circular indenter. The open loop bandwidth of the system is approximately 100Hz, which is greater than the bandwidth of both the human visual and motor control systems.

The relationships between indentation force and displacement and material properties such as the elastic modulus of tissue are presented, and models are developed that show the expected response to a standard tissue model. Characterization and calibration tests demonstrate the response of the prototype components. Experiments performed on spring and mass elements and on silicone gel samples, which mimic tissue response, show that the TeMPeST 1-D can accurately measure their force-displacement responses.

The TeMPeST 1-D and its data acquisition system are intended to be portable, to be easily transported to and used in an operating room. The system was used in proof-of-concept experiments performed on live pigs; an example of the measured properties of porcine liver is presented.

The TeMPeST 1-D is the first in a series of instruments that will be developed to support the generation of a comprehensive atlas of tissue material properties.

Thesis Supervisor: Dr. J. Kenneth Salisbury  
Title: Principal Research Scientist, Mechanical Engineering, MIT  
Professor, Departments of Computer Science and Surgery, Stanford

**Thesis Committee:**

Dr. J. Kenneth Salisbury, Chairperson  
Principal Research Scientist, Mechanical Engineering, MIT  
Professor, Departments of Computer Science and Surgery, Stanford

Dr. Mandayam A. Srinivasan  
Principal Research Scientist, Department of Mechanical Engineering, MIT

Dr. David L. Trumper  
Associate Professor of Mechanical Engineering, MIT



# Acknowledgments

This work was supported in part by:

the Center for Innovative Minimally Invasive Therapy (CIMIT) at Massachusetts General Hospital (MGH), with funding from the Department of the Army, under contract number DAMD12-99-2-9001. The views and opinions expressed do not necessarily reflect the position or the policy of the government, and no official endorsement should be inferred;

a National Science and Engineering Research Council (NSERC) of Canada PGS-B scholarship.

There are probably more people than I can say who have helped me to complete this work and keep me on track. In particular, I'd like to thank:

my committee members, Prof. Ken Salisbury, Dr. Mandayam Srinivasan and Prof. Dave Trumper, for their support, advice, and good ideas, and especially for helping to define a realistic scope for this research;

Dr. Karen Moodie, Prof. Joe Rosen and Dr. William Laycock of Dartmouth Medical School and Onux Medical, Inc. for their assistance in gaining access to the Dartmouth Animal Resources Center pigs; and Karen again (especially for help with the paperwork), Greg Burke and Sam Weinstein for taking care of the pigs while my data was being acquired;

Joe Samosky (for being amazed with the work) and Rachel Oppenheimer of Dr. Martha Gray's cartilage biomechanics and imaging laboratory at the Harvard Institutes of Medicine, for assistance in measuring the properties of my standard materials;

Dr. Robert Howe of Harvard University and Dr. Parris Wellman for the idea for and data on the silicone gel that I used as a prelude to real tissue;

Professors Chris Scott and Anne Mayes, and You-Yeon Won, of the Department of Material Science and Engineering, for providing access to their materials testing apparatus and help in measuring the properties of the standard gels;

Dr. David Schloerb for assistance with the MIT Laboratory for Human and Machine Haptics tactile stimulator.

Dr. Steven Dawson and Dr. Stephane Cotin of the Simulation Group of CIMIT at MGH for their support and interest throughout the research, and CIMIT for the funding that supported it;

Ela, Jesse, Arrin, Andrew and Brian and the other Haptics Lab members who've passed through and made the stay more enjoyable – movie night anyone?

Ron Wiken of the Artificial Intelligence Lab, for advice, assistance, and keeping the shop facilities in such great shape – it's been a joy to build stuff here;

all of the other people whose paths I've crossed and have helped me get just that much farther;

and last, but certainly not least, my parents, Peter and Erika, my sisters, Susan and Andrea, and my girlfriend, Rene, who have seen me through the last four and a half years with love and understanding – I'm finally done!

“O frabjous day! Callooh! Callay!”

He chortled in his joy.

Lewis Carroll, Jabberwocky

# Contents

<b>1</b>	<b>Introduction</b>	<b>21</b>
<b>2</b>	<b>Background</b>	<b>29</b>
2.1	Basics of visco-elastic behavior . . . . .	30
2.2	Geometric Effects . . . . .	35
2.2.1	Semi-infinite body approximation . . . . .	38
2.3	Tissue property review . . . . .	42
2.4	Tissue property measurement techniques . . . . .	44
2.4.1	Non-invasive tissue property measurement techniques . . . . .	44
2.4.2	Invasive tissue property measurement techniques . . . . .	47
<b>3</b>	<b>TeMPeST 1-D</b>	<b>53</b>
3.1	Design considerations for minimally invasive linear property measurement . . . . .	54
3.2	Actuator options: linear actuators . . . . .	56
3.2.1	Voice coil actuators and solenoids . . . . .	56
3.2.2	Piezo-electric actuators . . . . .	58
3.3	Position sensor options . . . . .	59
3.3.1	Optical encoders . . . . .	60
3.3.2	Laser interferometry . . . . .	60
3.3.3	Linear variable differential transformers (LVDTs) . . . . .	62
3.4	Force sensor options . . . . .	62
3.5	System layout options . . . . .	64

3.6	TeMPeST 1-D design details . . . . .	66
3.6.1	Voice coil and suspension design . . . . .	69
3.6.2	LVDT . . . . .	74
3.6.3	Force sensor . . . . .	75
3.6.4	TeMPeST 1-D electronics . . . . .	75
3.6.5	Flexible arm and fine positioning cam . . . . .	80
<b>4</b>	<b>System modeling and characterization</b>	<b>83</b>
4.1	TeMPeST 1-D System Modeling . . . . .	83
4.1.1	Voice coil actuator model . . . . .	84
4.1.2	Tissue contact I . . . . .	84
4.1.3	TeMPeST 1-D in free motion . . . . .	88
4.1.4	Tissue contact II . . . . .	89
4.2	TeMPeST 1-D Characterization . . . . .	92
4.2.1	Warm-up characteristics . . . . .	92
4.2.2	LVDT calibration . . . . .	93
4.2.3	Force sensor calibration . . . . .	95
4.2.4	Voice coil calibration . . . . .	95
4.2.5	Position sensor frequency response . . . . .	97
4.2.6	Force sensor frequency response . . . . .	98
4.2.7	Flexure stiffness; actuator effective damping and mass . . . . .	101
<b>5</b>	<b>GUI and controller development</b>	<b>105</b>
5.1	T1Dgui: graphical user interface for the TeMPeST 1-D . . . . .	105
5.1.1	Waveform type selection . . . . .	106
5.1.2	Sampling and waveform parameters . . . . .	108
5.1.3	Function buttons . . . . .	109
5.2	T1D.exe: real-time control and data acquisition for the TeMPeST 1-D	111

<b>6</b>	<b>Validation Tests and Tissue Property Measurements</b>	<b>113</b>
6.1	Testing on Mechanical Springs . . . . .	114
6.1.1	Spring testing apparatus . . . . .	115
6.2	Testing on Inertial Load . . . . .	119
6.2.1	Inertial load testing method . . . . .	119
6.3	Testing on Silicone Gel Samples . . . . .	121
6.3.1	ARES standard testing of gels . . . . .	122
6.3.2	Cartilage press standard testing of gels . . . . .	124
6.3.3	TeMPeST 1-D testing of gels . . . . .	126
6.4	In Vivo Solid Organ Measurements . . . . .	128
6.4.1	Laparoscopic testing . . . . .	129
6.4.2	Open surgical testing . . . . .	131
6.4.3	<i>In vivo</i> solid organ test results . . . . .	131
<b>7</b>	<b>Contributions, Discussion and Further Directions</b>	<b>135</b>
7.1	Summary . . . . .	135
7.2	Instrument and measurement comments . . . . .	137
7.3	Future work . . . . .	142
<b>A</b>	<b>Nomenclature</b>	<b>145</b>
<b>B</b>	<b>Flexure masks and etch sequence</b>	<b>147</b>
<b>C</b>	<b>TeMPeST 3-D</b>	<b>151</b>
<b>D</b>	<b>T1Dgui</b>	<b>155</b>



# List of Figures

1-1	Tissue Material Property Sampling Tool. . . . .	24
1-2	TeMPeST 1-D sensor/actuator package. . . . .	25
1-3	Laparoscope view of TeMPeST 1-D testing liver response. . . . .	26
2-1	(a) Maxwell and (b) Voigt body lumped parameter models . . . . .	30
2-2	Maxwell and Voigt body responses to step loads and displacements. Note continuous change in displacement of Maxwell body to step load, and impulse force response of Voigt body to step displacement. . . . .	31
2-3	Kelvin body. . . . .	33
2-4	Kelvin body responses to step load and displacement. . . . .	33
2-5	Kelvin body Bode plots. . . . .	33
2-6	Prismatic element under simple loading and equivalent spring model. . . . .	36
2-7	Equivalent magnitude-phase and complex modulus representations of visco-elastic responses. $y$ -axes are linear scale. Derived from Kelvin body with $k_1 = 10k_2$ , $b = k_2 \cdot 1s$ , unit dimensions. . . . .	38
2-8	Decreasing indentation magnitude ( $\mathbf{Z} \rightarrow Z \rightarrow z$ ) on a body with char- acteristic dimension, $\mathcal{R}$ , begins to approximate indentation of a semi- infinite body . . . . .	39
2-9	Elastography conceptual diagram: (a) undeformed soft material with hard inclusion, (b) deformed geometry under loading, (c) strain field. . . . .	45
2-10	Dundee single point compliance probe [6] . . . . .	49

2-11	Piezo-tube-based anisotropic stiffness measurement device [27]. (1) is the piezo-electric tube, and (15) includes part of the electronics to drive the tube at resonance. . . . .	50
2-12	Force reflecting endoscopic grasper [15] . . . . .	51
2-13	Bicchi device [3] . . . . .	51
3-1	Force on current carrying conductor in magnetic field: (a) single conductor (b) coil in radial magnetic field . . . . .	57
3-2	Moving-coil voice coil designs: (a) radially magnetized ring magnet, (b) flux focusing design, (c) bonded windings design (coil is load-bearing)	58
3-3	Piezo-electric actuator design examples: stack, tube and bi-morph. . .	60
3-4	Optical encoder operation. Spacing between light sources/detectors is some whole multiple of the grating spacing ( $n \cdot \lambda$ ), plus $\lambda/4$ . . . . .	61
3-5	Laser interferometry component arrangement (simplified) . . . . .	61
3-6	LVDT component arrangement and operation . . . . .	62
3-7	Examples of force sensor designs: (a) micro-machined piezo-resistive diaphragm, (b) piezo-electric sensors [21], (c) custom designed sensor with silicon strain gages . . . . .	64
3-8	System layout options: (a) collocated sensors/actuator, (b) external sensors/actuator, (c) external actuator/internal sensors . . . . .	65
3-9	TeMPeST 1-D sensor/actuator package fully assembled (left) and moving core alone, mounted on flexures (right) . . . . .	67
3-10	Sensor/actuator components. . . . .	67
3-11	TeMPeST 1-D system components . . . . .	68
3-12	Separable components so that sensor/actuator package can be sterilized.	69
3-13	Typical FEMM flux density/field line plot. . . . .	71
3-14	Force constant vs. position from model. . . . .	72
3-15	Flexural suspension . . . . .	73
3-16	Single flexure FEA output: spring constant = 105N/m. For applied force = 0.05N, z=0.48mm, maximum Von Mises stress = 132.4MPa . .	74



3-17	Modified force sensor components . . . . .	76
3-18	TeMPeST 1-D body, housing force sensor balance and instrumentation amplifier circuits, and the current source for the voice coil . . . . .	76
3-19	Direct voltage to current amplifier circuit . . . . .	78
3-20	Force sensor, balance and instrumentation amplifier circuit. . . . .	79
3-21	Modified Mediflex laparoscope/instrument holder and fine positioning cam. The cam provides fine position control over a range of 0.5" . . . . .	80
3-22	Details of fine positioning cam geometry. Pins on TeMPeST 1-D shaft follow cam in disk mounted to Mediflex arm. In this configuration, clockwise rotation about the axis generates linear motion of the shaft towards the right. . . . .	81
4-1	Second order model of voice coil actuator in free motion. . . . .	85
4-2	Position and measured force of voice coil actuator in contact with unknown (Kelvin) tissue. . . . .	85
4-3	Free space tip response for TeMPeST 1-D on Mediflex arm, with base motion ( $X_b/F_{coil}$ ) shown for comparison. . . . .	89
4-4	Full TeMPeST 1-D in contact with Kelvin body (top); magnitude and phase of measured force, position and base motion (middle); magnitude and phase of $X_{lvdt}/F_{meas}$ and ideal Kelvin response (bottom). . . . .	91
4-5	Measurements of compliance of mechanical springs made with TeMPeST 1-D fixed in vice and mounted on Mediflex arm . . . . .	92
4-6	Initial zero-force/zero-displacement warm-up response of position and force sensors. Force sensor 5% settling time is approx. 12 min. . . . .	93
4-7	Calibration jig for LVDT, as well as testing fixed displacement tests of voice coil and force sensor. . . . .	94
4-8	Calibration curves for LVDT and position constant. Voltage offset can be adjusted by the signal conditioner, but only slope is needed for frequency domain analysis. N=200 for each position. . . . .	94

4-9	Force sensor final calibration method: standard masses loaded on tip of inverted TeMPeST 1-D. . . . .	96
4-10	Force sensor calibration data. Voltage offset can be adjusted with the bridge balance circuit, but only slope is needed for frequency domain analysis. N=200 for each force value. . . . .	96
4-11	Force constant vs. axial position for voice coil. This is equivalent to the torque constant for a motor. . . . .	97
4-12	LVDT frequency response. Flat response to 500Hz, gain and phase response consistent with transport lag due to sequential analog measurements . . . . .	99
4-13	Force sensor frequency response (magnitude). . . . .	100
4-14	Static, quasi-static and dynamic force-displacement response for the indenter. Ideal second order response overlaid over data. . . . .	103
5-1	Control panel for graphical user interface. Includes controls for waveform type, sampling rate and duration, waveform amplitude, offset and frequency or frequency range. . . . .	106
5-2	Types of waveforms supported by the T1Dgui . . . . .	107
5-3	FFTs of linear and exponential chirp signals. All signals defined with 1Hz and 100Hz initial and final frequencies . . . . .	108
6-1	Testing of spring array with CBIL cartilage press (left) and TeMPeST 1-D (right) . . . . .	116
6-2	Spring testing array force-displacement response using CBIL cartilage press. Hysteretic 4-spring data caused by lags between force and position sensing. . . . .	116
6-3	Spring array stiffness under 0.1Hz sinusoidal excitation using CBIL cartilage press (CP: +) and TeMPeST 1-D (T1D: o), and chirp excitation with TeMPeST 1-D. . . . .	118
6-4	Test arrangement for inertial load experiments. . . . .	120
6-5	Bode plots of response of inertial loads . . . . .	120

6-6	Parallel plate shear modulus testing geometry . . . . .	122
6-7	RTV silicone solidifying in molds. . . . .	123
6-8	Magnitude and phase of shear modulus (G) (n.b. modulus is inverse of compliance, hence positive phase) . . . . .	124
6-9	CBIL cartilage press being used to test silicone gel sample. . . . .	125
6-10	Elastic modulus of RTV samples. Includes TeMPeST 1-D chirp, parallel plate rheometer (ARES), cartilage press (CP) data and TeMPeST 1-D fixed frequency sinusoidal response (30:70 sample only). . . . .	127
6-11	Exterior view of operating field for laparoscopic sessions . . . . .	130
6-12	Typical view of TeMPeST 1-D approaching contact with liver . . . . .	131
6-13	View of TeMPeST 1-D used during open surgical measurements of spleen	132
6-14	Non-parametric elastic modulus of liver. Spike at 60Hz is due to electrical interference in force signal. . . . .	134
7-1	Pivot-mounted force sensors with torsional actuator, riding on air-bearing supported carriage (left) deployable, surface mounted sensor/actuator package (right). . . . .	140
7-2	Concept for large-scale, 3-D motion force-displacement probe, the TeMPeST 3-D. . . . .	143
B-1	A completed sheet of flexures. The stiffest flexure is at the top left, the softest at the lower right. Flexures forming the fixed-fixed cantilever beams of a 1-axis force sensor occupy the bottom row. . . . .	148
B-2	Front and back sides of typical suspension and force sensor flexures, post-etching (from lower left corner of flexure sheet in figure B-1). Front side shows boss surfaces for clamping to TeMPeST 1-D body and core, back side shows cantilever and break-out tabs. . . . .	148
B-3	Complete set of masks, used to generate a series of flexures with different stiffnesses and cantilever beam elements for 1-D force sensor. . . . .	149
B-4	Photomask and etch sequence for generating flexures . . . . .	149

B-5	CAD model of the etched flexures. Note thinner cantilever and break-out tab regions. . . . .	150
C-1	An early conceptual model for the TeMPeST 3-D. Apart from computer control, this model demonstrated an early concept for the cable drive, with motions in the pitch, yaw and thrust directions. . . . .	151
C-2	A more fully fleshed out version, including motors at the base, a universal joint near the tip, and a 3-axis force sensor behind the blunt probe. Position sensing in this version is done with the encoders on the motors, but redundant sensors closer to the tip would improve accuracy. . . . .	152
C-3	Tip design for the TeMPeST 3-D. A universal joint permits motion in pitch and yaw, but prevents rotation of the tip about the shaft. Linear bearings in the sleeve support the axial motion of the tip. A novel 3-axis force sensor (pitch- and yaw-moment, and axial thrust) measures the reaction forces of the tissue. . . . .	152
C-4	Cable drive system for the TeMPeST 3-D. The top motor controls pitch of the probe, the side motors are redundant in controlling yaw, and all together they move the central carriage along the shaft of the tool. Not shown are linear bearings which would support the shaft at the upper right, and lower left, as well as at the tip of the tube (see figure C-2).	153
C-5	TeMPeST-power: the interface box underneath the docking station houses a power source, PWM current amplifiers and interface circuitry to support the TeMPeST 1-D, the TeMPeST 3-D, and potentially other devices to be developed later. . . . .	153
D-1	The TeMPeST 1-D graphical user interface. . . . .	156
D-2	Instantaneous frequency of chirp vs. time and drive current vs. instantaneous frequency. . . . .	157

D-3	Fast Fourier transform of the drive current signal. For linear chirp, transform has flat magnitude within chirp frequency range. For exponential chirp, $\log(\text{magnitude})$ falls with a slope of -0.5 with respect to $\log(\text{angular frequency})$ . . . . .	157
D-4	Raw voltage output from the TeMPeST 1-D, including pre- and post-measurement offset voltages (upper and lower left). Upper traces in each plot are force sensor voltage, lower traces are LVDT voltage. . .	158
D-5	Processed position and force signals. Position is positive for increasing indentation. . . . .	158
D-6	Fast Fourier transform of position. . . . .	159
D-7	Fast Fourier transform of force. . . . .	159
D-8	Measured material compliance: ratio of fast Fourier transforms of position and force. . . . .	160



# List of Tables

2.1	Simple deformations of elastic, semi-infinite bodies with rigid, right cylindrical indenter of radius $a$ . Shear cases require no-slip condition at interface. . . . .	40
2.2	Examples of reported tissue properties . . . . .	43
6.1	Measured spring stiffness summary. . . . .	117
6.2	Best fit values for standard masses . . . . .	121
6.3	Cartilage Press quasi-static elasticity data . . . . .	125
6.4	Experimental parameters for <i>in vivo</i> tests of solid organs . . . . .	133





# Chapter 1

## Introduction

Surgical training in teaching hospitals today is often performed based on the familiar adage “see one, do one, teach one,” in which new surgeons and medical students first observe experts performing operations, then perform them under supervision, and in turn pass their skills on to newer doctors. This sequence depends on the arrival, in the operating or emergency room, of patients with conditions requiring the operation to be taught. Not only can such an environment be highly stressful to the new surgeon, but clearly the health and well-being of the patient is risked on the incompletely developed skill-set of the surgeon.

Recent years have seen the nascence of the field of surgical simulation, in which a surgeon may learn, practice and be evaluated on mannequin- and computer-based systems. Such systems will be able to provide a solid base of skills to new surgeons so that when they finally do have contact with patients, they will be more familiar with the cognitive and manual skills required to successfully perform their tasks.

Surgical, and more generally medical simulations take a page from a field where simulation has become very important, that of flight simulation. In modern flight simulators, well developed models of the dynamics of flight and the performance of given aircraft are linked to hardware interfaces that are similar to those in real aircraft. With this combination, pilots can be exposed to the basics of flying under normal conditions, as well as being faced with scenarios where problems and complications arise, without risk to themselves or their potential passengers. In fact, private pilots

may apply training time spent in a flight simulator towards up to 20% of total flight training hour requirements [10], or even more depending on the type of aircraft.

One of the key features of developing a flight simulator is developing accurate models of the behavior of the aircraft and its environment, including aerodynamics and the responses of the controls and actuator systems, as well as audio, visual and motion/haptic feedback from the simulated environment. In the same vein, a surgical simulation system will require models of the human body, including its geometry, the mechanical and physiological responses of the organs and tissues, models of the instruments to be used and hardware interfaces so that the surgeons can see, hear and feel what they are training on. The models and feedback systems must be realistic enough so that the trainees can “suspend disbelief”, feeling that they are actually performing on real tissues, and so that they do not learn bad habits from a simulator that deviates too far from reality.

Creating a realistic simulation depends in large part on developing accurate models of the mechanical response of the organs and tissues to deformation with surgical instruments. As will be discussed further, there are numerous ways of modeling the response of visco-elastic (or more complex) responses of tissues, including lumped-parameter and finite element techniques. Some (e.g. finite element modeling or FEM) are inherently more accurate than others (e.g. lumped-parameter) for the complex geometry and properties of tissues, which may be non-linear, inhomogeneous, anisotropic or time-dependent (amongst others). Accuracy is traded-off at the cost of additional computation and slower response of the simulation, which must be fast enough to appear to run in real-time to the user.

Whatever method of modeling is used, however, all depend on knowledge of the material properties of the tissue being simulated. If a simple, lumped-parameter model is to be used, then spring constants and damping coefficients are required, which can be determined from the geometry and inherent material properties of the tissue. For finite element models, for example, the material properties, such as Young’s modulus, the Poisson ratio and damping ratio would be included directly as parameters for the model. Thus, some method of acquiring these data is necessary

to make simulation systems that are based on the physics governing the response of real tissues.

Tissue properties have been determined in the past by extracting samples from the organ of interest, and measuring their responses on devices similar to those used to measure the properties of engineering materials (e.g. steel or concrete). Tissue samples removed from the living state can radically change in their responses, as the blood supply to the cells is cut off, as temperature and humidity change, and as the boundary conditions of the sample in the organ are different from those in the testing device.

Recent work in measuring tissue properties has begun looking at tissues *in vivo* and *in situ*, that is in the living state and in the environment of the body, without removal. Toward these tests, many methods, ranging from surgically invasive, to minimally invasive and entirely non-invasive, are being developed.

This thesis presents the design and development of a minimally invasive surgical instrument (see figure 1-1) which can measure the force-displacement response of solid organ tissues over small deformations and forces, and over a range of frequencies relevant to surgical simulation with both visual and haptic feedback.

The following chapters begin with an introduction to basic aspects of tissue modeling, and some of the simplifications that can be made to conveniently extract tissue properties from knowledge of the force-displacement response of visco-elastic media. The primary simplification employed in this work is the approximation that for small deformations, large organs can be modeled as semi-infinite bodies. This simplification permits the use of closed form expressions relating force, displacement and the material properties of the organ. Chapter 2 also includes a review of existing and planned methods and devices for measuring tissue properties *in vivo*. These are divided into a class of non-invasive techniques, which employ magnetic resonance or other imaging techniques to examine deformation fields within the body, and a class of invasive techniques which record the mechanical response of tissue, at discrete points, to some known load or displacement. This section concludes with a brief comment on one class of measurements that has not been covered by these techniques, namely the

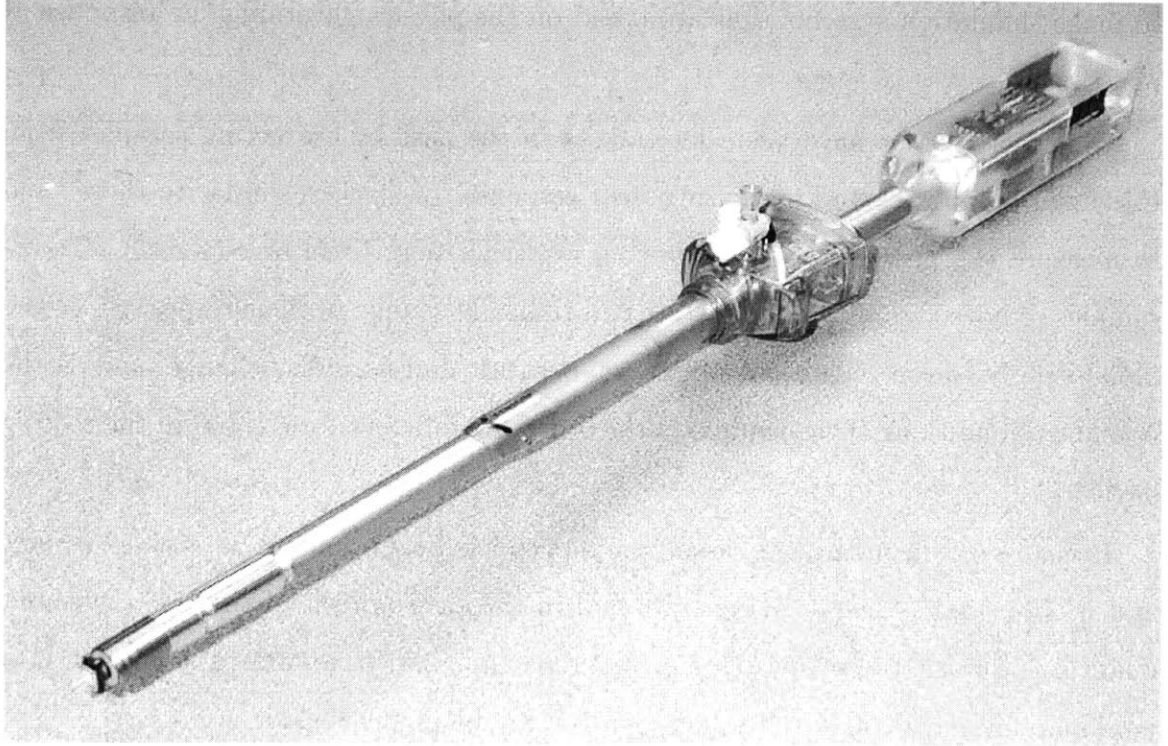


Figure 1-1: Tissue Material Property Sampling Tool.

investigation of the frequency dependence of tissue properties in the range relevant to simulation with haptic feedback.

The Tissue Material Property Sampling Tool, or TeMPeST 1-D, which is the subject of this thesis, is described in detail in chapters 3 through 6. Chapter 3 begins with a discussion on the design criteria and available options for the system components, including force and position sensing and linear actuation. The second half of the chapter goes into a detailed discussion of the TeMPeST 1-D prototype and its systems. The sensor/actuator package that was developed (see figure 1-2) includes a novel voice-coil actuator combined with a specially modified force sensor and a position sensor. The entire package has a 12mm outer diameter, so that the instrument fits through standard laparoscopic ports. The electronics and other system components are also described. The entire system is designed to be easily portable, supporting transport to and use in the operating room for acquisition of tissue properties *in vivo*.

Chapter 4 begins with the development of mathematical models of the instrument and hypothetical models of contact with visco-elastic media. A simple second

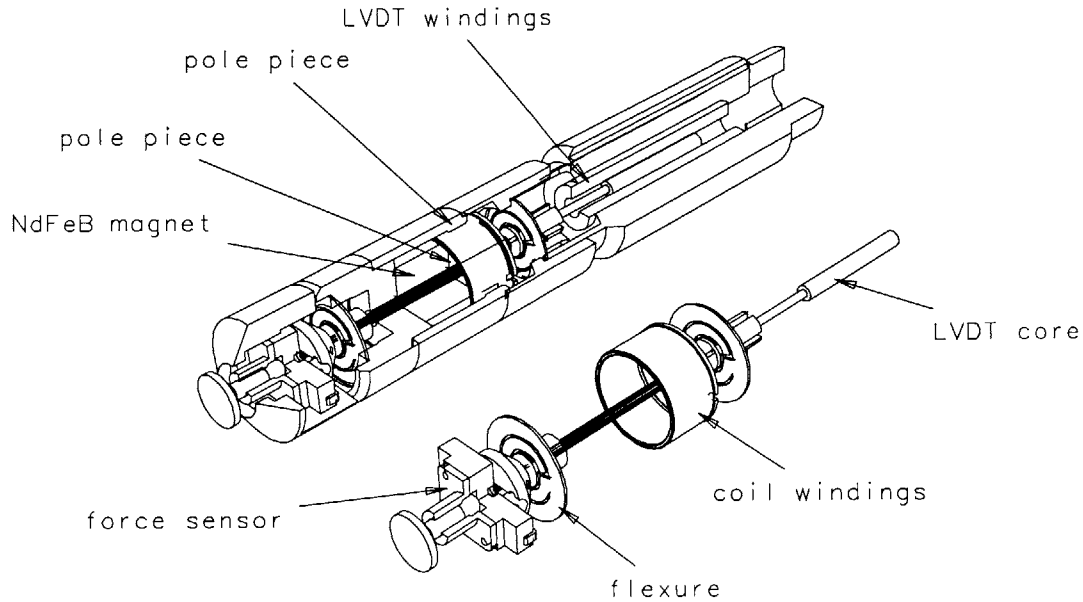


Figure 1-2: TeMPeST 1-D sensor/actuator package.

order model is used to illustrate how the transfer function of the tissue can be determined from measurements of applied force and displacement. A fourth order model includes the contributions of the dominant dynamic elements of the system, including the actuator and the body of the TeMPeST 1-D mounted on a surgical instrument holder. This model is used to examine the kinds of distortions that the real system would introduce in comparison with the ideal (second order) model. The bulk of the chapter is devoted to calibration and characterization tests to populate the models with parameters for the real instrument. These tests include the determination of the force and position vs. voltage constants for the sensors as well as their dynamic responses. These sections also cover the determination of the effective stiffness, mass and damping of the sensor/actuator package and the force constant of the voice coil actuator.

Chapter 5 is a short chapter that describes the graphical user interface (GUI) and real-time control/data acquisition program. The GUI includes pre-processing functions that generate the waveforms used to excite the tissue, and post-processing elements to analyze the force-displacement data acquired during testing. The principle output is a non-parametric representation of the frequency-dependant compliance



Figure 1-3: Laparoscope view of TeMPeST 1-D testing liver response.

of the tissue. Using the geometric information developed in chapter 2, these data can be used to determine models of the visco-elastic properties of tissue. The real-time data acquisition code runs the TeMPeST 1-D in open-loop, sending current to the voice coil and recording the measured force and displacement sensor voltages at speeds up to 2kHz.

Experiments performed on standard materials, including springs, masses and silicone gel, are described in chapter 6. These tests were performed to verify that the TeMPeST 1-D can be used to correctly extract the characteristics of materials whose properties are known *a priori*. As a proof of concept demonstration, the TeMPeST 1-D was used to perform *in vivo* tests on the liver and spleen of pigs at the Dartmouth College medical school. Figure 1-3 is the view through a laparoscope of the instrument measuring the properties of liver in minimally invasive conditions. Chapter 6 concludes with the details and results of these experiments, including the determination that, given the semi-infinite body approximation, porcine liver is primarily elastic from 0.1 to 100Hz, and has an elastic modulus between 10 and 15kPa.

Chapter 7 summarizes the contributions and implications of this work. It revisits the important elements of the preceding chapters, and looks at directions for further research. This includes concepts for new instruments to resolve some of the limitations

of the TeMPeST 1-D, as well as instruments to measure properties of organs and tissues for which TeMPeST 1-D is not suited.

To supplement the material in the text of this thesis, appendices are included which summarize the nomenclature used in the thesis; describe the manufacture of the TeMPeST 1-D flexural bearings; present some details of a design for a proposed device called the TeMPeST 3-D, which will extend the range of force-displacement tests that can be performed into the non-linear and potentially anisotropic regime; and present a sequence of images of the graphical user interface and pre- and post-processing output.





# Chapter 2

## Background

Computer-based surgical simulation begins with the development of models of the mechanical response of organs and tissues. Depending on the desired level of realism, they may range from simple lumped parameter models, such as the two-parameter Voigt and Maxwell, and three-parameter Kelvin models [12], to full-blown finite element models, which are computationally expensive, to intermediate representations like the “water-bed” model [8], which balances between complete accuracy and speed of calculation. In the first part of this chapter, some of the simpler models will be discussed in relation to how they may be used in determining material properties of tissue from measurements of force-displacement responses. Mention will also be made of the types of data required, in light of the perceptions of the user of a simulation system.

The second part of the chapter will review the two classes of measurement techniques that are used to determine tissue properties: non-invasive methods, employing global scanning technologies such as magnetic resonance imaging and ultrasound, to acquire strain field measurements under known external loading conditions; and invasive methods that impose and record local loads or displacements made directly upon organs and tissues.

The chapter will conclude with a discussion of what areas of tissue property measurement have not been covered by the existing body of research, and look towards the development of the TeMPeST 1-D.

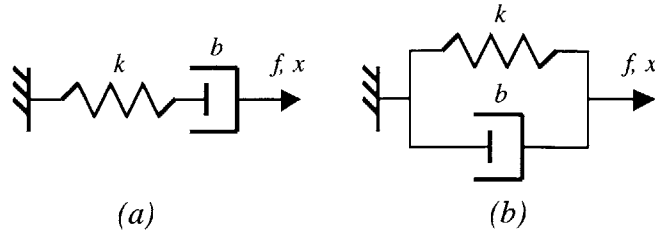


Figure 2-1: (a) Maxwell and (b) Voigt body lumped parameter models

## 2.1 Basics of visco-elastic behavior

In observing the response of many biological tissues to mechanical loading, a number of dominant characteristics are observed. Consider the case of a sample of tissue, attached at both ends to the jaws of a testing device and subjected to different kinds of loading.

If a step in applied force is made on the sample, the tissue can behave elastically over short time scales, in that a step change in the length of the sample is observed. Thus, a very simple model of tissue might be to represent it as a spring element with a known spring constant. If however, the load is maintained for some time period after the initial step, one might observe the length of the tissue to increase further than the initial response, a phenomenon called creep. Since this property occurs over time, some additional element should be included in the model of this “visco-elastic” material, typically a lumped damping element, such as an idealized dashpot.

Alternatively, if a step change in length is made (impossible in reality, but illustrative for the purposes in modeling), the applied force at very short time scales would be proportional to the strain imposed on the tissue, but as time passes, the force would fall, a phenomenon called stress relaxation. Again, an elastic and a dissipative element need to be included in a model to describe the tissue.

Two models with these two elements are possible: the Maxwell body which treats the tissue as a series spring-dashpot system, or a Voigt body, which models the tissue as a spring and dashpot in parallel [12]. Figures 2-1 and 2-2 show the models of the tissue and the step responses to both applied load and displacement. Equations 2.1–2.4 present the governing equations for these systems, and their transfer functions.

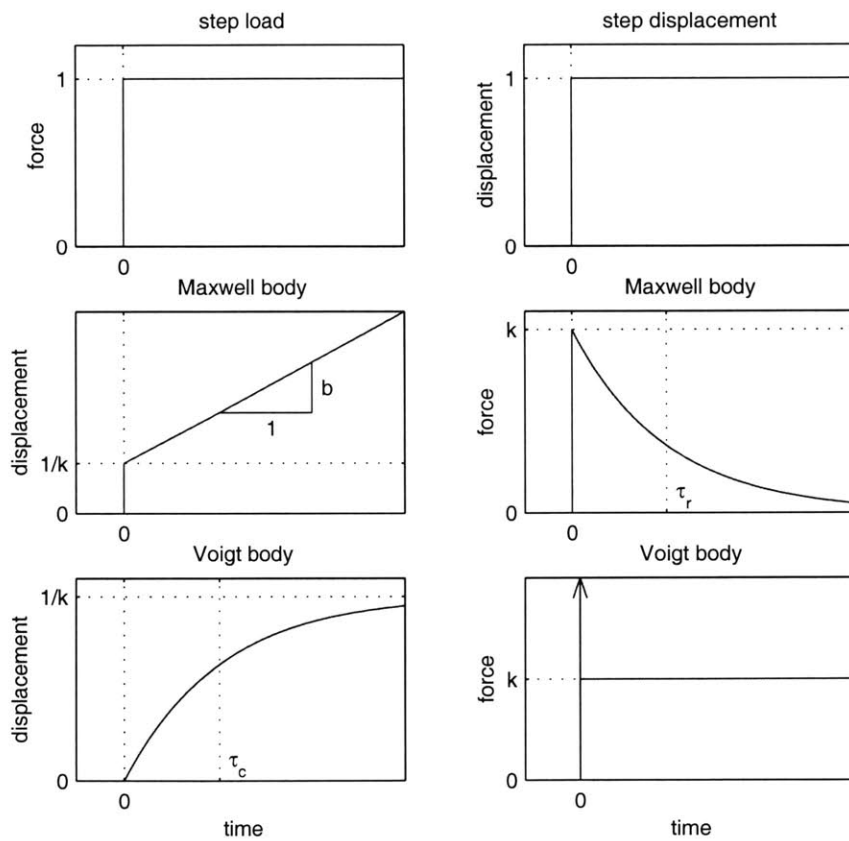


Figure 2-2: Maxwell and Voigt body responses to step loads and displacements. Note continuous change in displacement of Maxwell body to step load, and impulse force response of Voigt body to step displacement.

$$\text{Maxwell body: } x = \left( \frac{1}{k} + \frac{1}{b} \int dt \right) f \quad (2.1)$$

$$\frac{X(s)}{F(s)} = H_m(s) = \left( \frac{1}{bs} + \frac{1}{k} \right) \quad (2.2)$$

$$\text{Voigt body: } f = \left( k + b \frac{d}{dt} \right) x \quad (2.3)$$

$$\frac{X(s)}{F(s)} = H_v(s) = \frac{1}{bs + k} \quad (2.4)$$

Each of these models captures part of the observed behavior of tissue, but the Maxwell body exhibits continuous creep under a step force, with no limits on ultimate displacement (not observed in most biological tissues over the time scales relevant to surgery), while the Voigt model would predict an impulse response to a step change in displacement, which is also not observed.

Increasing the complexity of the model to the three parameter Kelvin body [12], as shown in figure 2-3, solves this problem. The response to step loads shows the initial elastic response as well as creep to a final length, while the response to a step displacement shows a finite value for the initial force, relaxing to some limiting value (figure 2-4). The time response, equation 2.5 can be characterized by three parameters: the relaxation time constant,  $\tau_r$ , the creep time constant,  $\tau_c$ , and the relaxed stiffness,  $k_r$ , where the time constants are the time required for the visco-elastic portion of the response to reach  $(1 - e^{-1}) \times 100\%$  of the final response, and  $k_r$  is the ratio of the force and displacement of the step deformation response as time approaches infinity. Equations 2.7 - 2.9 provide the relationships between  $k_r$ ,  $\tau_r$  and  $\tau_c$  and the values for the springs and dampers in the Kelvin model. The Bode plots for the Kelvin body are shown in figure 2-5.

$$\left( \frac{b}{k_1} \frac{d}{dt} + 1 \right) f = k_2 \left( b \frac{k_1 + k_2}{k_1 k_2} \frac{d}{dt} + 1 \right) x \quad (2.5)$$

$$\frac{X(s)}{F(s)} = H_k(s) = \frac{1}{k_r} \frac{\tau_r s + 1}{\tau_c s + 1} \quad (2.6)$$

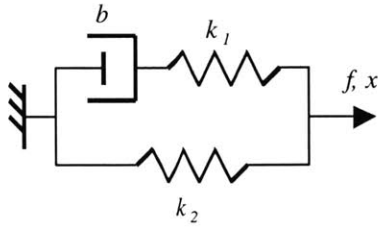


Figure 2-3: Kelvin body.

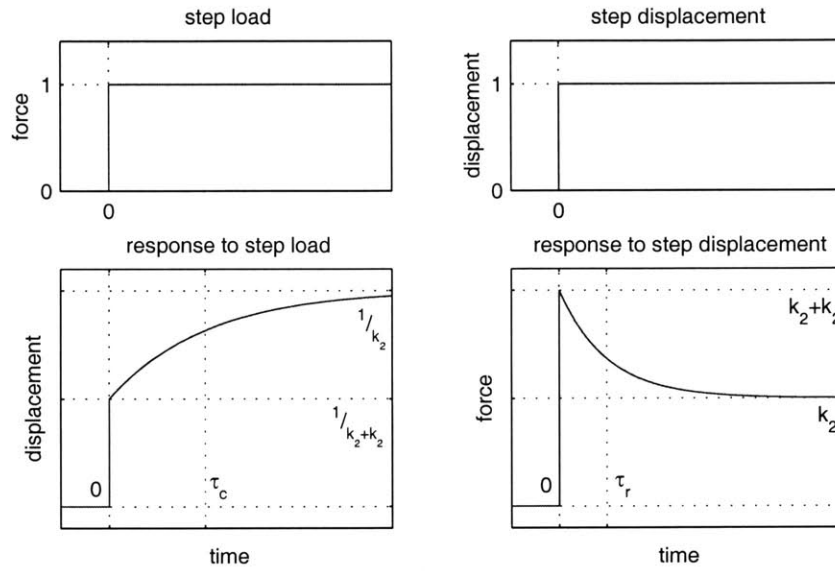


Figure 2-4: Kelvin body responses to step load and displacement.

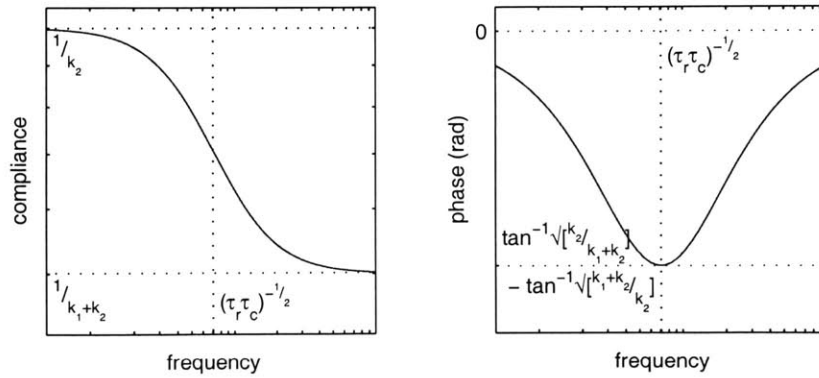


Figure 2-5: Kelvin body Bode plots.

$$k_r = k_2 \quad (2.7)$$

$$\tau_c = \frac{(k_1 + k_2)b}{k_1 k_2} \quad (2.8)$$

$$\tau_r = \frac{b}{k_1} \quad (2.9)$$

More complex behaviors can be generated by creating series and parallel networks of Kelvin or other models, with the limiting case of an infinite number of elements to create an arbitrary response [12].

The sinusoidal response of a Kelvin material is characteristic of a lag filter; at low frequencies, the damping effects are negligible, so the stiffness corresponds with only one of the spring elements. At high frequencies, the damping element acts as a rigid element, so the stiffness is the sum of the two springs. The break frequencies for the rise and plateau correspond with the creep and relaxation time constants.

The transition between low and high frequencies depends on the tissue and the damping mechanism involved. Cartilage, for example, exhibits a poro-visco-elastic response, in which one damping mode is the motion of fluid through the matrix of the tissue. Based on the results of some experiments [26], the division between high and low,  $((\tau_r \tau_c)^{-1/2})$ , can be as low as 0.01Hz. Above this frequency, fluids do not have enough time to migrate out of the tissue, so the tissue stiffness is effectively higher than that below  $(\tau_r \tau_c)^{-1/2}$ .

Figure 2-5 presents the sinusoidal response of the Kelvin body as the compliance, or apparent softness, versus frequency. As will be revisited later when material properties, rather than lumped parameters, are examined, is it common to present the stiffness (inverse of compliance) of the tissue. As far as the preceding discussion, this simply involves inverting the transfer function, as well as the magnitude and phase plots, so that apparent stiffness increases with frequency, and the phase is positive (see figure 2-7, for example).

With respect to surgical simulation, the sensing and control capabilities of the human user set guidelines for the frequency domain of interest. Clearly static forces can be applied and perceived by a user. Human control of hand motions is limited

to a range on the order of a 1–10Hz, or a few repetitive motions per second—we simply cannot move our fingers faster than this. At the same time, we have mechano-receptive nerve endings in our skin, some of which have peak sensitivity to vibrations in the 100’s of Hz range [4]. With these issues in mind, testing should be done, and tissue properties be determined such that behavior over the whole range of the human “sensorium” is covered.

## 2.2 Geometric Effects

The preceding discussion is essentially specific to the geometry of a given material sample, looking only at its force-displacement response to different loading conditions. For such data to be useful beyond the test bench, the parameters characterizing the response need to be transformed into material properties which are independent of geometry. In the thought experiments described above, the material being tested would typically have simple, known geometry, such as a rectangular or circular prism. Such geometries permit simplifying assumptions such as uni-axial and uniform stress distributions in the sample, and simple (e.g. uniform) strain distributions. With these assumptions made, simple relationships between geometry-dependent lumped parameters describing the force-displacement behavior and geometry-independent material properties can be determined.

Consider a sample that might behave like a spring (figure 2-6). In the case of a prismatic test element with cross sectional area,  $A$ , the force ( $f$ ) is imposed uniformly across the ends of the sample, causing the length to change from  $l_0$  to  $l$ . The sequence leading to equation 2.10 demonstrates that the material’s elastic modulus can be determined from the lumped spring constant and the known geometry.

$$\begin{aligned}k &= \frac{f}{x} \\E &= \frac{\sigma}{\epsilon} \\x &= l - l_0\end{aligned}$$

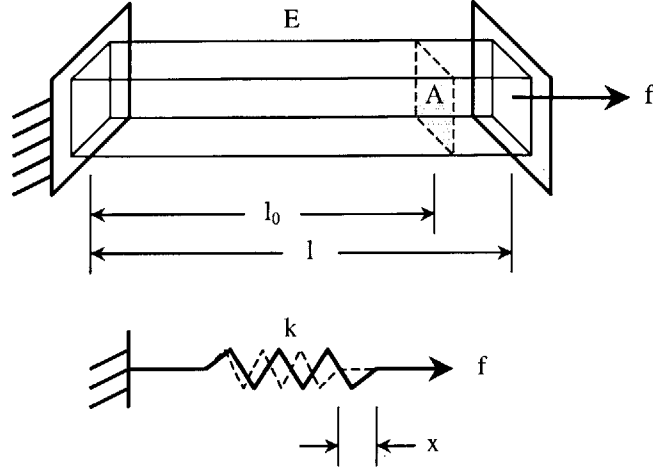


Figure 2-6: Prismatic element under simple loading and equivalent spring model.

$$\begin{aligned}
 \sigma &= \frac{f}{A} \\
 \epsilon &= \frac{x}{l} \\
 \Rightarrow E &= \frac{f \cdot l}{x \cdot A} \\
 &= k \frac{l}{A}
 \end{aligned} \tag{2.10}$$

This expression is valid for static deformations where elasticity is the only material parameter needed. It can, however, be extended to the frequency domain, which is necessary to describe visco-elastic materials, through the “correspondence principle” [12], in which the static value for the elastic modulus,  $E$ , is replaced with a frequency dependent expression, called the complex modulus,  $E(i\omega)$ .

$E(i\omega)$  is the geometry independent, elastic form of  $H(i\omega)$ , which was the transfer function for the lumped parameter model compliance. It is derived simply by substituting the transfer function for stiffness (the inverse of equation 2.6 in the case of a material acting like a Kelvin body) into equation 2.10. Equation 2.11 shows the result for the Kelvin material example.

$$E(i\omega) = k_r \frac{l}{A} \frac{\tau_c i\omega + 1}{\tau_r i\omega + 1} = E_r \frac{\tau_c i\omega + 1}{\tau_r i\omega + 1} \tag{2.11}$$

It is typically presented graphically in one of two equivalent forms: plots of the



magnitude,  $|E(i\omega)|$ , and phase,  $\delta$ , of the sinusoidal response versus frequency (equation 2.12)<sup>1</sup>; or as the elastic ( $E_e$ , in-phase) and dissipative ( $E_d$ , out-of-phase) components of the complex modulus versus frequency, which are also the real and imaginary components of  $E(i\omega)$  (equation 2.13). Figure 2-7 shows the response of a Kelvin body in both forms.

$$E(i\omega) = |E(i\omega)| e^{i\delta} \quad (2.12)$$

$$= E_e(\omega) + iE_d(\omega) \quad (2.13)$$

$$\begin{aligned} E_e(\omega) &= \Re(E(i\omega)) \\ &= |E(i\omega)| \cos(\delta) \end{aligned}$$

$$\begin{aligned} E_d(\omega) &= \Im(E(i\omega)) \\ &= |E(i\omega)| \sin(\delta) \end{aligned}$$

Data presented for the experiments described in chapter 6 will be shown in the magnitude-phase form since it is more convenient to determine the transfer function parameters from this representation. If the low and high frequency magnitude asymptotes are  $E_l$  and  $E_h$ , and the frequency at maximum phase is  $\omega_m$ , then the parameters of equation 2.11 are given by equations 2.14 to 2.16.

$$E_r = E_l \quad (2.14)$$

$$\tau_c = \sqrt{\frac{E_h}{E_l \omega_m}} \quad (2.15)$$

$$\tau_r = \sqrt{\frac{E_l}{E_h \omega_m}} \quad (2.16)$$

---

<sup>1</sup>An alternative to presenting phase is to present  $\tan \delta$ , the “internal friction”

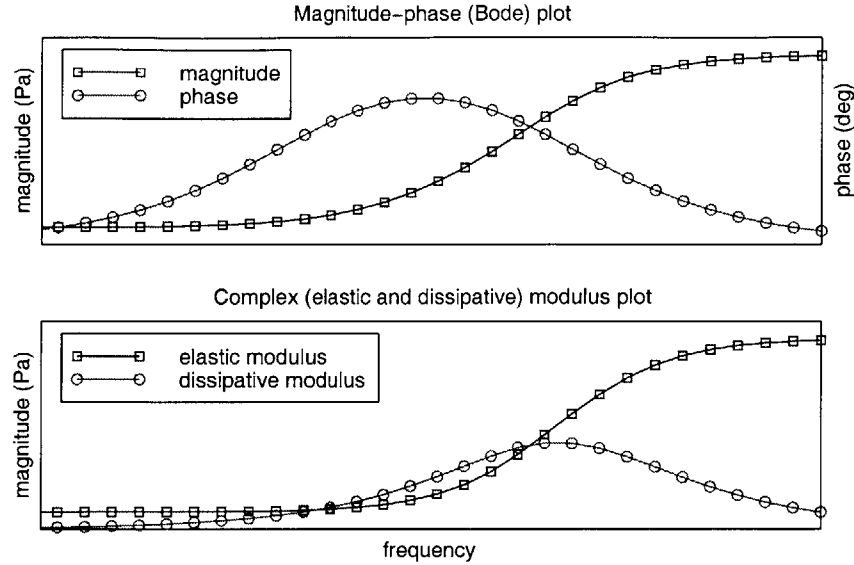


Figure 2-7: Equivalent magnitude-phase and complex modulus representations of visco-elastic responses.  $y$ -axes are linear scale. Derived from Kelvin body with  $k_1 = 10k_2$ ,  $b = k_2 \cdot 1s$ , unit dimensions.

### 2.2.1 Semi-infinite body approximation

As was mentioned in the introduction, real tissues do not typically take such convenient forms as those presented above. Liver, kidney, spleen, and other solid tissues have both complex surface and internal geometries. However, when one considers small regions of the organ relative to the bulk, and small deformations within that region, some simplifying assumptions can still be made.

Consider the example of figure 2-8. In this case, the deformation imposed by an indenter is also fairly large compared with the characteristic dimension of the body. If one magnifies the region of contact and reduces the depth of indentation (and to a lesser extent, the size of the indenter), in the limit it begins to take on the appearance of a semi-infinite body, with a surface extending in all directions away from the point of contact, and the material extending indefinitely below the surface. For this geometry, in the case of a right circular indenter applying a load to the surface, a number of closed form solutions have been derived describing the relationship between force, displacement, and the material properties of the body. Different loads may be applied to the surface, for which a few of the governing relationships are summarized

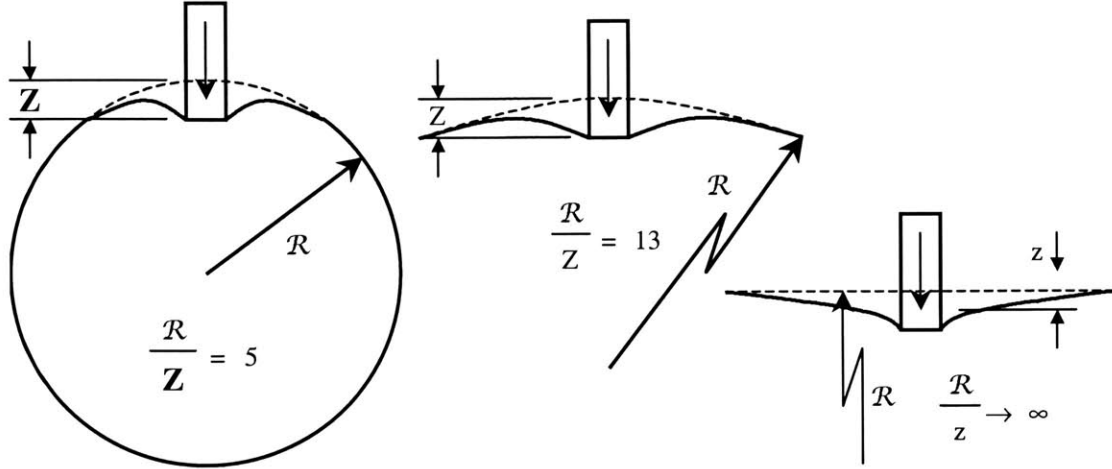


Figure 2-8: Decreasing indentation magnitude ( $Z \rightarrow Z \rightarrow z$ ) on a body with characteristic dimension,  $\mathcal{R}$ , begins to approximate indentation of a semi-infinite body

in table 2.1 (derived from [19]).

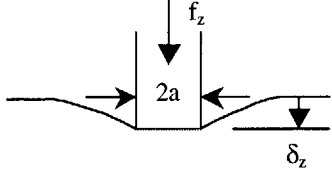
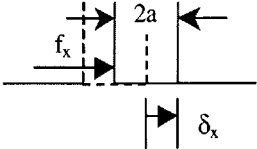
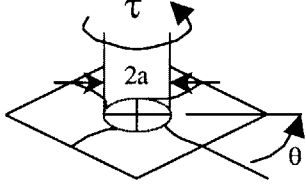
For normal indentation, uniform displacement in the  $z$ -direction, and friction-free contact are assumed, so that sliding of tissue across the surface of the indenter is permitted (equation 2.17). If the punch adheres perfectly to the surface, equation 2.18 applies. However, because of the  $(1 - 2\nu)$  term, this expression is highly sensitive to the value of the Poisson ratio ( $\nu$ ) when it is close to 0.5. Since this condition applies for many tissues (see below), it would be preferred to arrange experiments such that the friction-free expression applies.<sup>2</sup>

For tangential shear, uniform displacement in  $x$  is assumed, but slight deformation above and below the plane of the surface is permitted. The rotational shear case assumes no  $z$ -axis motion and uniform rotation of the tissue under the indenter.

Each of these expressions includes the two unknowns  $E$  (Young's modulus) and  $\nu$ , so both cannot be determined from measurements made using only one type of deformation. For example, a normal indentation and a rotational shear (or some other combination) would have to be performed to fully determine both parameters. However, much of the literature on biological tissue reports that it is often nearly incompressible (not surprising considering the large water content, which is also nearly

<sup>2</sup>During laparoscopic surgery, the atmosphere inside the abdomen is very humid, and all of the tissue surfaces are slick, so for a non-porous indenter, the friction-free, or at least a low-friction, condition applies.

Table 2.1: Simple deformations of elastic, semi-infinite bodies with rigid, right cylindrical indenter of radius  $a$ . Shear cases require no-slip condition at interface.

Normal Indentation	Tangential Shear	Rotational Shear
		
$E_{stip} = \frac{(1 - \nu^2)f_z}{2a\delta_z} \quad (2.17)$ $E_{stick} = \frac{(1 + \nu)f_z}{2a\delta_z \ln \frac{3-4\nu}{1-2\nu}} \quad (2.18)$	$E = \frac{(2 + \nu + \nu^2)f_x}{2\pi a\delta_x} \quad (2.19)$	$E = \frac{3(1 + \nu)\tau}{8a^3\theta} \quad (2.20)$

incompressible), so the Poisson ration,  $\nu$ , has a value very close to 0.5 [36, 32, 20]. If the expression relating force, deformation,  $E$  and  $\nu$  is insensitive to small errors in the estimate for  $\nu$  only one type of experiment is needed to determine the properties of the material. By performing tests over a range of frequencies of interest, the frequency dependent expression for  $E$  can be determined.

Note that such deformation tests need to closely approximate the assumed conditions: deformations must be small relative to the geometry of the tissue, and local tissue/organ curvature should similarly be small. At the same time, it should be recognized that since these small deformation/large body conditions are the same ones that would lead to assumptions of linear behavior in the material, this implies that these expressions could be superposed, so that deformations in the normal and tangential shear directions, for example, could be described by a vector sum of the

two components.

The semi-infinite assumption eventually breaks down as organ sizes may be too small or deformations too large to justify it. At this point, numerical solutions to the governing elastic equations, including finite element or other techniques, must be turned to. One set of solutions is an extension to the normal indentation case described above, for soft materials with known thickness bonded to a rigid substrate [16]. In this case, a correction factor, which depends on the ratio between indenter radius and sample thickness,  $a/h$ , and the Poisson ratio, is applied to equation 2.17 yielding equation 2.21. An extension to this solution, which takes into account not only finite thickness, but also the mean depth of indentation has been derived (equation 2.21), which essentially increases the value of  $K$  as indentation depth increases [34].

$$\begin{aligned}
 E &= \frac{(1 - \nu^2)f_z}{2a\delta_z K \left\{ \frac{a}{h}, \frac{x}{h}, \nu \right\}} & (2.21) \\
 K &> 1 \\
 \lim_{h \rightarrow \infty} K &= 1
 \end{aligned}$$

If  $a/h = 0.2$  and  $\nu = 0.5$ , then a fit for  $K$  is [34]:

$$K = 1.23 + 1.26 \frac{\delta_z}{h} \tag{2.22}$$

This extension takes into account some of the effects of preloading the body being tested. For a true semi-infinite body, the depth of indentation should not affect the linear relationship between force and displacement. For non-ideal bodies, the apparent stiffness will increase, so some information about either the mean pre-load or mean depth of indentation is important to include in property extraction. These issues were taken into account in performing measurements on silicone gel samples, described in chapter 6.

In still more complex geometries, finite element techniques can be used in which the material properties are iterated, and simulations performed, until the simulation

yields the same response as the measured tissue.

To this point, certain tacit assumptions have been made. These include material homogeneity and isotropy. In real organs, tissue properties may vary from location to location both on the surface of the organ, and within an organ. Such inhomogeneity can be seen in the difference in stiffness between skin on the back of the hand, and calloused skin under the heel of the foot. Since these differences are location dependent, a series of measurements can be made over different locations so that a complete map of the variation in properties can be generated. Tissues are also often anisotropic. Good examples include tendon and muscle, which have different stiffnesses and strengths along and across the length of their fibers [9]. Normal indentation and rotational shear would not typically provide information about the directional variation in properties, but tangential shear might, by examining the responses to shear deformation in different directions along the surface of an organ.

## 2.3 Tissue property review

Measurements have been made of the material properties of different kinds of tissues for many years. Some sources for data from human and animal tissues include [9] and [35]. These data are primarily taken from measurements made *in vitro*, under a variety of conditions differing from the normal living state. The first of these is the lack of blood perfusion, and therefore oxygenation, blood pressure, and supply of energy to the cells, so the tissue is either beginning to die, or is long dead. In the case of Yamada's summary [35] for example, samples were permitted to age for some period to reach a "steady-state" value before being measured.<sup>3</sup> Humidity may not necessarily be controlled in all experiments and temperature may vary from the physiological state. Some tissue has even been packed in ice and thawed prior to testing [7]. Further, the boundary conditions of a sample, and therefore its internal stress state will change when the sample is cut away from the rest of the organ. Ideally, one would prefer to measure tissues *in situ*, so that the loads imposed by

---

<sup>3</sup>Some data indicate the factor by which "steady-state" and tissue *in vivo* differ.

adjacent tissue and organs are as close to normal as possible [12].

Beyond the circumstances of testing, insufficient data is available regarding a complete description of the tissue in question. Most often, a single stiffness or strength parameter is reported for the case of static or quasi-static testing. Ultimate strength measurements are often reported, but are not useful for simulations that do not cause damage (tearing or cutting) to tissue, which constitute much of what must be modeled. Tissues are generally non-linear, so some more comprehensive set of parameters, or family of describing curves would be desirable. Inhomogeneity is often a characteristic of organs, so multiple stiffnesses would be needed for a detailed description. In addition, many tissues exhibit anisotropy in their properties, so some description of the variation in stiffness, damping or non-linearity with orientation would also be desirable from the standpoint of developing a library of tissue properties.

A brief review of some of the data available, including information regarding the testing methods and source, is included in table 2.2. Sources such as Yamada [35] and Duck [9] cover many more types of tissues than are included here, but are subject to some of the problems described above.

Table 2.2: Examples of reported tissue properties

tissue/property	value	measurement method
Liver		
$K_b$ , human [9]	2.53-2.70GPa	ultrasonic velocity
$E$ , rabbit [35]	5.6kPa	indentation <sup>4</sup>
	19.4kPa	tensile <sup>5</sup>
$E$ , bovine [7]	0.43-1.68kPa	compression ( $\epsilon < 5\%$ )
Kidney		
$K_b$ , human [9]	2.54GPa	ultrasonic velocity
$E$ , rabbit [35]	8.8kPa	tensile <sup>5</sup>

As can be seen from this short table, the available data comes from numerous testing techniques, with widely varying results. More recent data presented in other sources, such as [25] and [5] are in forms that are not conveniently converted to stiffness moduli because the necessary geometric parameters were unreported.<sup>6</sup> Further,

converting from the adiabatic bulk modulus data ( $K_a$ ) to Young's modulus is not possible without a good estimate for the Poisson ratio. As can be seen from equation 2.23, when  $\nu$  is close to 0.5, small errors can dramatically change the calculated value for  $E$  based on  $K_a$ .

$$E = 3K_a(1 - 2\nu) \tag{2.23}$$

## 2.4 Tissue property measurement techniques

Since tissue properties measured *in vitro* may be significantly different from those measured *in vivo*, a number of research groups are developing methods and devices for taking data from living tissues, often *in situ*. There are two general classes of measurement techniques: non-invasive methods, which apply an external load to the body and measure the internal strain or vibration fields with scanning techniques such as magnetic resonance imaging (MRI) or ultrasound; and invasive methods, which typically apply local loads to tissue and examine the force-displacement response. Several examples of each technique will be discussed in the following sections.

### 2.4.1 Non-invasive tissue property measurement techniques

A number of non-invasive methods have been developed over the last few decades to determine the internal structure of the body, including ultrasound, magnetic resonance imaging, and computed tomography imaging, using X-rays.

Ultrasound has been used to directly measure the stiffness of tissues, by examining the relationship between the speed of sound through tissue, and the tissue elasticity [22]. In solid mechanics, for typical engineering materials, there is a direct relationship (equation 2.24,  $K_b$  = bulk modulus,  $\rho$  = density) between sonic velocity

---

<sup>4</sup>2.63mm indentation, using 10g load on 5mm round flat indenter

<sup>5</sup>estimate of slope in linear ( $\epsilon < 10\%$ ) range of stress strain curves, Figures 175 and 181 of [35]

<sup>6</sup>E.g. [25] report stress and the thickness ratio achieved with their device, but not data on the thickness of the tissue relative to the size of the compression surfaces, and [5] does not define the way that strain was calculated, or describe the indentation tip (see section 2.4.2).



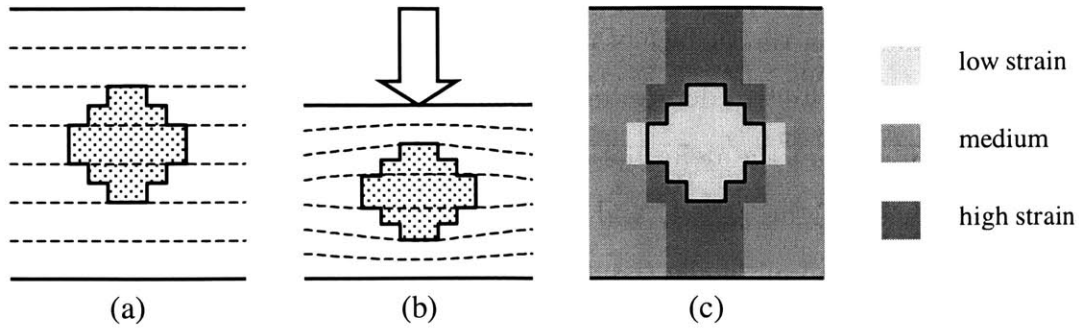


Figure 2-9: Elastography conceptual diagram: (a) undeformed soft material with hard inclusion, (b) deformed geometry under loading, (c) strain field.

and elasticity which is generally applicable. However, because ultrasound transducers typically operate in the kilohertz to megahertz range, rather than in the DC to tens or hundreds of Hertz range, elasticity derived in this manner may not be applicable for surgical simulation [32]. As was mentioned in section 2.1, transitions between different stiffness regimes may occur at frequencies much lower than those employed in ultrasound. Some measurements which directly compared static stiffness with sonic velocity, by simultaneously measuring with a load cell and an ultrasound transducer, found no significant relationship [22].

$$\begin{aligned}
 v &= \sqrt{\frac{K_b}{\rho}} \\
 &= \sqrt{\frac{E}{3(1-2\nu)\rho}}
 \end{aligned}
 \tag{2.24}$$

Ultrasound, MRI and CT methods can be used, however, in other ways. One method, which looks at the static properties of tissue, involves taking two successive scans of the tissue in question, before and after applying a simple load to the outside of the body. Originally devised for ultrasound (and called “elastography” [23]), this method is equally applicable for use with other methods.

Essentially, elastography depends on the inverse relationship between the stiffness of a deformable body, and the strain that it undergoes when loaded. The first scan provides a baseline for comparison (see figure 2-9a). Then some load (as simple as

possible) is imposed on the surface of the body. A second scan is made (2-9b), which is compared with the first to determine the magnitude and direction of deformations within the body. From the deformation data, a map of the strain field within the tissue is generated (figure 2-9c), and this strain field processed, to determine the relative local moduli of all of the tissue within the scan field.

This description significantly simplifies the calculations involved in determining the strain field, and thus the elasticities. A number of difficulties are inherent in this technique, which have limited its use to date. First, stress and strain are tensor quantities; individual ultrasound, MRI and CT scans, however, are two-dimensional cross sections of the tissue, and therefore cannot directly capture out-of-plane deformations. Since the separation between scans can be 10 times larger than in-plane resolution [33], calculation of strain in the third dimension is problematic.<sup>7</sup> Assumptions such as incompressibility [32] or uniform stress distribution at the surface [20] can provide sufficient constraints to determine strain fields.

Second, some calculation techniques do not handle high-contrast elasticity changes well. For example, when a hard inclusion is present in a soft material, the strain field calculations will predict “shadow artifacts” [20], which are erroneous regions of hardness within what should be soft tissue. For simple geometries, such artifacts can be neglected as being obviously in error. However, for unknown, complex geometries, such as those found in the internal organs, the shadows could be confused with actual changes in elasticity.

One last item is that elastograms are unable to directly measure the absolute value of the elasticity of tissues, but only the relative stiffnesses between tissues. This is because the applied stress field is often not known, nor does any material within the strain field have a known elasticity. One solution is to deliberately include a known material within the field, and compare all of the tissues to it. For example, in work done to detect breast tumors, a layer of rubber of known modulus was placed between

---

<sup>7</sup>Some researchers [18] are developing instruments with 2-D arrays of ultrasound transducers to permit scanning of pyramidal volumes of tissue, but such systems have not been used for tissue property measurement.

the tissue and the ultrasound scanner (which also applied the load), so that its strain was also calculated to serve as a reference for all of the other tissues [31].

A second approach using scanning techniques uses a dynamic load to excite vibrations within tissue. Vibration amplitude, and therefore local velocities, are related to the tissue stiffness, and can be determined using Doppler velocimetry.

Called “sonoelastography” when used with ultrasound [24], and MRI elastography for the corresponding magnetic resonance technique [30], this method involves applying a small amplitude vibration, typically tangentially, to the surface of the body, while simultaneously measuring the velocity field within the body. Different groups have used vibrations from as low as 20Hz to the low kHz range [24]. By sweeping the frequency over a range of interest, or testing at different constant frequencies within the range, damping coefficients or time constants for the tissues could, in principle, be determined. No examples, however, of this sort of measurement were found.

## 2.4.2 Invasive tissue property measurement techniques

Because the non-invasive techniques cause no trauma, they might be ideal for studying human tissue properties. They have, however, not yet been used to generate a library of tissue property data, in part because of the complexity of the calculations involved (a primary area of research). In addition, the cost of MRI or CT machines (or access to them) can be prohibitively high for many researchers, and in the case of CT, requires subjects to be exposed to X-rays.

As an alternative, a number of devices have been developed to perform measurements directly on tissues, so that their force-displacement responses can be determined. Generally speaking, a load is applied with an instrument of some geometry, and the force or displacement of the region of contact is measured. By making certain approximations regarding the geometry and characteristics of the tissue (such as those described earlier in this chapter), material properties of the tissue can be determined from the force-displacement response.

## **Dundee Single Point Compliance Probe**

This device (figure 2-10) has been developed to perform indentation tests on solid organs (e.g. liver, spleen, kidney). It consists of a rigid rod attached to a 1-axis force sensor, and a surrounding sleeve which slides relative to the rod and whose relative position is measured with a linear position sensor. The hand-held device is used during open surgery; it is brought into contact with the tissue, and pushed gently until the rigid rod has indented the tissue by 5mm relative to the sleeve. Force and displacement are recorded as the indentation occurs. In a preceding step, the thickness of the organ is measured with an ultrasound probe to provide a characteristic length from which to define strain.

The DSPCP has been used to perform tests on human liver *in vivo* during the course of elective surgery, and on a variety of other tissues, the results for which are expected to be published in the near future. They show significantly non-linear responses, and variation in stiffness both between organs, and between healthy and diseased tissue [5].

This device is suitable for taking quasi-static measurements on tissue, and is one of very few that have been used to take measurements *in vivo* on human organ tissue. Since it is hand-held, it would be difficult to use to acquire data over a range of frequencies above that at which the user could move the device. However, having the quasi-static data would provide a reference for further property measurement.

## **Anisotropic tissue property measurement device**

Tissues such as skin often exhibit anisotropy in their stiffnesses, which can be interrogated in a number of ways, such as through the use of a device found in the US patent literature. The device shown in figure 2-11 makes use of a piezo-electric tube, fixed at one end, and contacting the tissue at the other [27]. The piezo-tube can be driven to resonate in an arbitrary orientation, the frequency of which will depend on the stiffness of the tissue it contacts. By sweeping the orientation and recording the resonant frequency at different locations on the tissue surface, a map of the tissue



Figure 2-10: Dundee single point compliance probe [6]

stiffness anisotropy can be generated.

While designed for external use, it could be used during open surgery, or with some modifications, in minimally invasive surgery. From the available literature, it is not clear if it has been used to measure tissue properties yet, and if so, would not have been used to measure the properties of internal organs.

### **Force reflecting endoscopic grasper (FREG)**

In addition to surgical simulation, some researchers are investigating methods for performing remote, or tele-surgery. An essential component of such a system is the “slave” manipulator, which performs the grasping or cutting of the tissue (under the control of the “master” which the surgeon manipulates). The slave manipulator can also be used as a robotic device, grasping tissue under computer control, and recording the applied forces. The FREG (figure 2-12) has been used to perform tests on tissue in this fashion. Using a Babcock grasper, which has rectangular, roughly parallel jaws, tissue can be grasped and force and displacement of the jaws recorded. Tests have been done on living tissue, including liver and spleen, by applying short

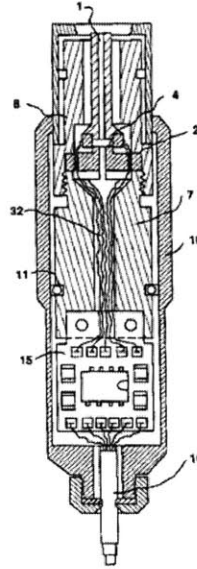


Figure 2-11: Piezo-tube-based anisotropic stiffness measurement device [27]. (1) is the piezo-electric tube, and (15) includes part of the electronics to drive the tube at resonance.

1Hz oscillations and yielding some quasi-static stiffness information, including force-displacement hysteresis information [25].

### Enhanced force feedback device

Another modified minimally invasive tool is that shown in figure 2-13. In this case, the goal was to provide enhanced force-feedback to the surgeon performing minimally invasive surgery, by instrumenting a surgical grasper, and providing a separate force-feedback device. The second device would generate a response to touch that mimicked the response of the real tissue [28]. The intent here was not the measurement of tissue properties specifically, but determination of a force-displacement response model for the tissue. Some properties could be extracted from the data if the tissue contact geometry was known. This is the prime difficulty of using this tool for these purposes—with a regular surgical grasper, the contact region is significantly more complex than that of the FREG, so without additional sensors, it would be difficult to determine geometry independent material parameters for any tissue measured.

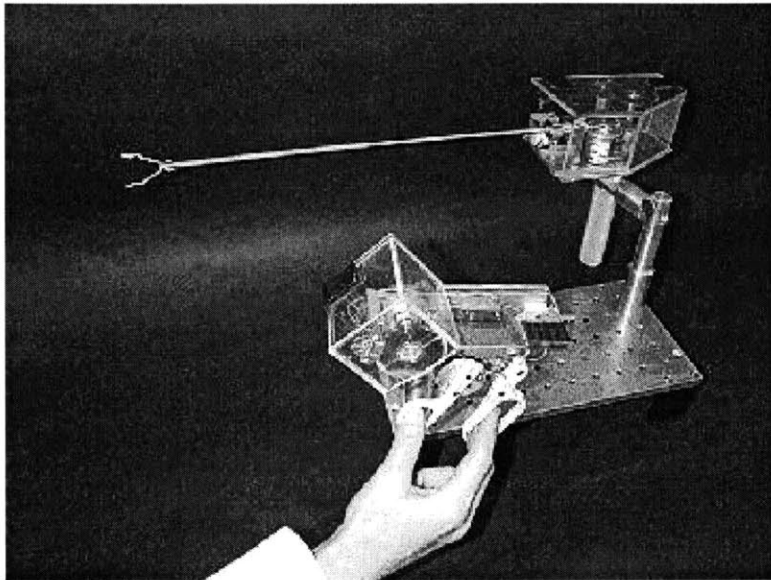


Figure 2-12: Force reflecting endoscopic grasper [15]



Figure 2-13: Bicchi device [3]

## Other devices

The devices described above by no means represent a complete survey of all of the existing devices that have the capacity to acquire *in vivo* tissue data. Two other methods include a pipette aspiration technique, where deflection vs. vacuum pressure in a tube touching the tissue is used [1]; and a stylus-mounted ultrasound transducer/force sensor, designed for use in measuring the stiffness of amputee stump tissue. The latter measures depth of compression via ultrasound echoes, and applied force with the force sensor [36].

## TeMPeST 1-D

An open question in surgical simulation is how much accuracy is required in the models of organs to achieve the desired educational goals. For cognitive training, where perhaps only the sequence of tasks is to be learned, then very simple (or no) models are needed. Training sensor-motor skills, however, will typically require some fidelity in the simulation's force feedback. Going further, tissue simulation could be used to develop new procedures, or evaluate designs for new surgical instruments with reduced need for animal testing. These applications require increasing levels of accuracy, but what is not known is exactly what level of realism is necessary. To be able to answer this question, very detailed models should be available, which can be degraded to observe the effects on the application.

One part of generating such an accurate model is knowledge of how tissue properties change over the range of frequencies relevant to simulation with haptic feedback. The frequency dependent properties of solid organs is one of the domains of tissue property measurement that has not been significantly investigated. To begin this investigation, a device was designed to examine the linear response of tissue over these frequencies. This device and its use will be the subject of the following chapters.



# Chapter 3

## TeMPeST 1-D

As was shown in the previous chapter, a number of instruments and methods for tissue measurement exist, which look at specific aspects of tissue behavior. At the outset of the research described here, two different domains of tissue measurement were considered for study: large scale deformation in three dimensions, and small scale, one-axis deformations, but with the capability to examine a wide range of frequencies. Preliminary designs were developed for both, and the latter was developed into the complete instrument described herein. As this work is the beginning of a longer term body of research, the three-axis device remains to be developed further, although the preliminary design is discussed in chapter 7.

The one-axis Tissue Material Property Sampling Tool (TeMPeST 1-D) was developed to provide force-displacement data suitable for the determination of linear material properties over a range of frequencies relevant to surgical simulation with haptic feedback. It was designed for use in minimally invasive or open surgical settings, keeping in mind issues such as electrical, mechanical and biological safety. The following sections consider the requirements for such a device, options for sensor and actuator systems, and go into detail regarding the design of the prototype.

### 3.1 Design considerations for minimally invasive linear property measurement

To perform the force-displacement measurements required to characterize the tissue, a number of different components must be part of any instrument. These include methods for measuring the displacement of the tissue and the force response, and some means of applying a deformation to the tissue.

Since linear properties are desired, this implies that only small deformations need to be (or alternatively, can be) applied, giving some guidance towards actuator and position sensor selection. The definition of “small deformations” depends on the material and geometry of the structure being examined. As was shown in the summary of existing liver property data, for example, strains of a few percent, implying deformations of no more than a few millimeters, remain in the linear stiffness regime [5]. Again taking liver as an example, since it is a large organ with significant regions where the local curvature of the tissue is low, millimeter-scale deformations are on the scale of a few percent, using the local thickness of the liver as a characteristic dimension<sup>1</sup>.

As shown in section 2.2 a number of simple motions can be imposed on tissues under which extraction of material properties is fairly simple. Linear indentation, rotational shear and tangential shear are all possible deformation modes. A basic requirement for the shear modes, and the “stick” mode of indentation is that non-sliding contact is maintained between the tissue and the device, generated by an adhesive or roughened surface, for example. Adhesives might be difficult to remove from the tissue without damaging it or leaving some part of the indenter tip behind, and roughened surfaces may need to be so rough that the non-ideal geometry may introduce unmodeled tissue-probe interactions, distorting the measurements. For example, [27] suggests the use of a short needle piercing the surface of the tissue

---

<sup>1</sup>The liver’s longest dimension is approximately 20–22.5cm, transverse to the body, and its thickness (upper to lower surface) between 15 and 17.5cm [14]. It is, however, wedge shaped, narrowing towards the left, so depending on the location, the characteristic dimension or thickness will be smaller than this, as the front or left edge are approached.

to maintain the position of their vibrating piezo-tube tip. On the other hand, the frictionless indentation solution is easier to achieve, since the wet surfaces of the living tissue already provide some lubrication, and additional lubricant could be applied to guarantee low friction contact. For these reasons, the “slip” mode of normal indentation was chosen for the TeMPeST 1-D.

Considering linear indentation, the existing stiffness data and the use of the semi-infinite body expressions provide guidelines for the force that an actuator should be able to provide to create deformations on the scale described. For liver, using the maximum value for Young’s modulus from table 2.2, a 5mm diameter punch, and a nominal indentation depth of 1mm, a rearranged form of equation 2.17 yields a minimum force of:

$$\begin{aligned}
 f &= \frac{2aE\delta_z}{1-\nu^2} & (3.1) \\
 &= \frac{2(2.5\text{mm})(19.4\text{kPa})(1\text{mm})}{1-(0.5)^2} \\
 &= 0.13\text{N}
 \end{aligned}$$

Further, since property variation over a range of frequencies relevant to simulation with haptic feedback (i.e. DC to >100Hz) is of interest, the actuators, sensors and the system as a whole need to have steady DC response, and bandwidth preferably larger than the maximum frequency to be considered.

These values represent minimum design goals. Because the tool is intended for use in a minimally invasive environment, two further constraints must be taken into account.

First, a device will typically take the form of a long shaft with an outside diameter corresponding with a standard size for surgical trocars and cannulas.<sup>2</sup> Many commercial instruments (e.g. shears, grippers, laparoscopes, surgical staplers) come in 5

---

<sup>2</sup>Trocar: sharp-pointed instrument used to pierce abdominal wall to permit placement of cannula. Cannula: tube with “trap-door” seal, inserted through abdominal wall to permit passage of surgical instruments, while maintaining elevated pressure inside abdominal cavity.

or 10mm sizes, but 12mm devices are also fairly common, and 12mm cannulas were available in the animal testing facilities that will be described in section 6.4.

Second, if a device will eventually be used to measure human tissue properties, any element that enters the body must be sterilizable, implying that either the whole tool, or some detachable part of it must be tolerant of one or more sterilization techniques. Some of these include autoclaving (high temperature saturated steam “bath”) and placement in an anoxic environment with special gases (such as ethylene oxide [13]) to destroy pathogenic organisms.

## 3.2 Actuator options: linear actuators

Based on the requirements just discussed, a number of candidate classes of actuators that support small deformations and forces are immediately apparent. Voice coil motors and solenoids, shape memory alloy (SMA), and piezoelectric and magnetostrictive actuators, among others, were examined to determine whether they could be used to generate motions on the order of those considered here. SMA wire actuators are limited by the thermal time constant of the wire, and provide only tensile loading, however strains of up to approximately 5% can be achieved. Piezoelectric and magnetostrictive materials respond up to very high frequencies, but can only generate strains on the order of parts per million; they would be difficult to use to create an actuator with millimeter-scale displacements. Voice coils and solenoids can be designed to have large displacements, reasonable bandwidth, and apply both tensile and compressive loading. They will be examined in additional detail as they were the prime candidates for use in the TeMPeST 1-D. Piezoelectrics will also be illustrated as a representative of the class of solid state actuators.

### 3.2.1 Voice coil actuators and solenoids

Voice coil actuators convert electric current to applied force through the relation  $\vec{d}\vec{f} = I \cdot \vec{d}\vec{l} \times \vec{B}$ , appropriately cast for the particular geometry of the actuator.  $\vec{d}\vec{f}$  is the force applied to conductor element  $\vec{d}\vec{l}$ ,  $I$  is the current passing through

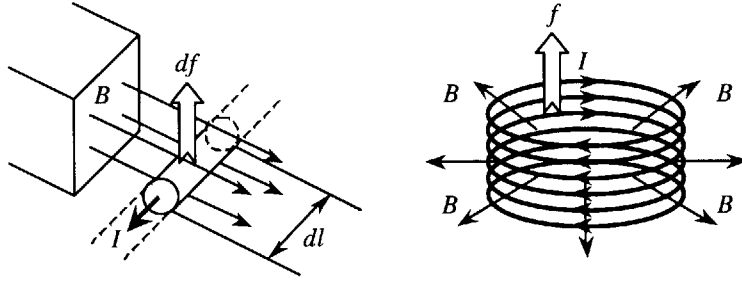


Figure 3-1: Force on current carrying conductor in magnetic field: (a) single conductor (b) coil in radial magnetic field

the element, and  $\vec{B}$  is the flux density in the region of the conductor element (see figure 3-1).

Voice coil actuators typically employ permanent magnets to generate the  $B$  field, and a coil placed such that the  $B$  field is perpendicular to its conductors. Running a current through the coil creates a force on the coil. If the coil (or the magnet) is mounted to bearings, it will move under the influence of the applied force, and this motion could be used in this case, to deform the tissue. Alternating current passed through the coil would therefore generate an oscillating force and displacement. A common example of a voice coil actuator is a loudspeaker. When mounted on flexural bearings (as is the case for a loud speaker), the actuator can generate motion in either direction from the rest position and may have nanometer resolution with proper control. Other applications include disk drive head positioning and wafer stepper fine positioning. Range of motion is typically in the millimeter to centimeter range, depending on the design of the actuator [29]. Constant force can be generated, and the bandwidth is limited by the coil/actuator mass and the spring constant of any suspension. One drawback is the heat generated in the coils when large forces must be generated. Some examples of coil and magnet arrangements are shown in figure 3-2.

Solenoids use a current carrying coil, but typically have the coil fixed in place, and have a moving ferrous core piece, which is drawn into the coil when current is applied. Force is inversely proportional to the square of the air gap width between pole pieces. A spring is used to return the core piece to its rest position when the current is turned off. Solenoids are often used in switching applications, so that only the end points of

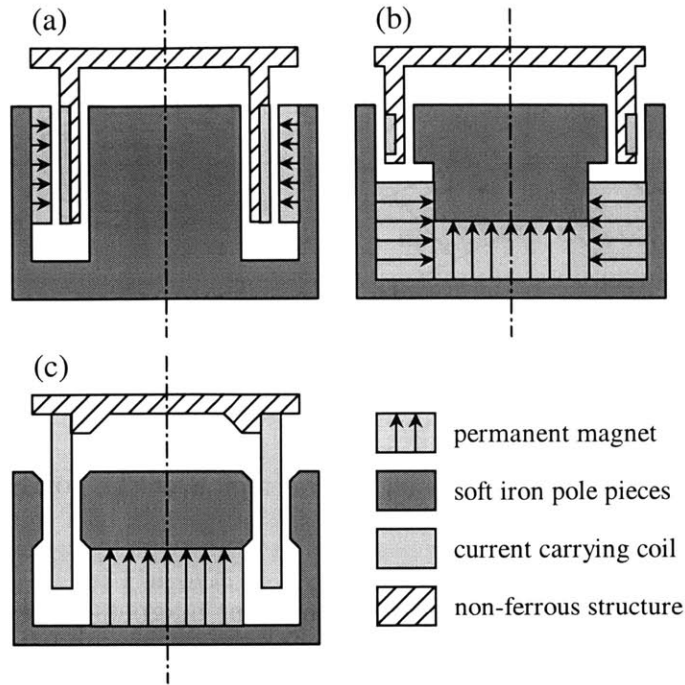


Figure 3-2: Moving-coil voice coil designs: (a) radially magnetized ring magnet, (b) flux focusing design, (c) bonded windings design (coil is load-bearing)

motion are important [29]. However, by varying the applied current, position control can be achieved. Since the rest position corresponds with one end of the range of motion, to achieve oscillatory motion, a non-zero offset current can be applied, and an oscillation imposed on top of that. As with the voice coil actuators, Joule heating occurs in the windings, potentially raising the temperature of the device.

Range of motion depends on the length of the coil and core piece, and can be 10cm or greater. As with voice coils, static forces can be applied, and bandwidth is determined by the mass of the core piece and the stiffness of the return spring.

Rotary solenoids and voice coil-type motors can also be generated, as well as galvanometer-like actuators, but these would require some rotary to linear transmission to generate the desired linear indentation motion.

### 3.2.2 Piezo-electric actuators

Piezoelectric materials undergo mechanical strains when electric fields are applied across them. Common geometries include stacks of elements, whose total displace-

ment is the sum of the elements in series, and cantilevered elements which flex, providing comparatively large amplitude motions at the cantilever end (figure 3-3).

Range of motion is typically very small, as strains are typically less than 0.1%.<sup>3</sup> As a result, stacks of electrically parallel and series mechanical piezoelectric elements are assembled, so that net deformation is increased, but even so deflections are typically on the order of tens of microns. Further, large voltages ( $\sim 100 - 1000\text{V}$ ) typically need to be applied to generate the maximum strain values [29].

Steady displacements can be generated, and bandwidth can be extremely high. This is partially due to the high stiffness of the material. With respect to tissue property measurement, however, high stiffness and low range of motion are disadvantages. As was shown earlier, to achieve a reaction force in the 100mN range, displacements of approximately 1mm are necessary (and greater for softer tissues). To generate such a displacement with a piezo-stack, the stack would have to be over one meter long! The smaller forces that would be generated with smaller displacements would be increasingly difficult to measure accurately.

Flexing, bimorph elements can achieve larger displacements, but typically only do so when they are driven at resonance, so that the tip motion is amplified. Since examination of properties over a range of frequencies is of interest, bimorphs would not be appropriate either (and could be difficult to fit into a 12mm shaft and still generate motion in a useful direction).

### 3.3 Position sensor options

To measure the deformation of the tissue, it may be sufficient to measure the displacement of the tip of the tool. To avoid introducing friction (such as would be present in a potentiometer), non-contact position sensors were considered for the TeMPeST 1-D.

---

<sup>3</sup>e.g. a low voltage piezo stack, part TS18H5-104, from Piezo Systems, Inc. of Cambridge, MA is 18mm long and can deflect by  $13.5\mu\text{m}$ , or 0.07%.

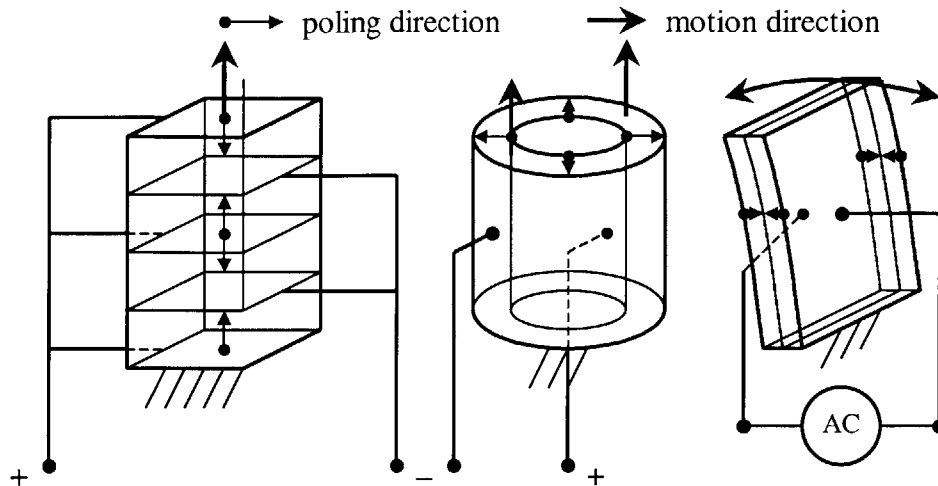


Figure 3-3: Piezo-electric actuator design examples: stack, tube and bi-morph.

### 3.3.1 Optical encoders

Optical encoders measure position by detecting changes in light transmitted through a moveable grating (figure 3-4). Often two light sources/detectors are placed such that the light/shadow patterns that are generated when the grating moves are in “quadrature”. This allows the determination of the direction of grating motion relative to the sources/detectors. When properly aligned, the source/detectors and the grating do not contact each other, allowing friction-free position measurement.

Encoders are limited in resolution to the line spacing on the grating, and ultimately for very high resolution devices, by diffraction effects. Output is digital.

Since it is often desirable for sensors and actuators to be co-located, this would require that the encoder be placed near the tip of the shaft of the tool. There are, however, few commercially available encoders that could fit within the confines of a 12mm (or smaller) minimally invasive tool shaft.

### 3.3.2 Laser interferometry

Constructive and destructive interference between two light beams can also be used to measure position. As shown in figure 3-5, a beam of laser light is split, and the beams follow different paths, reflecting off of either a fixed mirror, or one whose motion is to be measured. The beams are recombined and will constructively or destructively



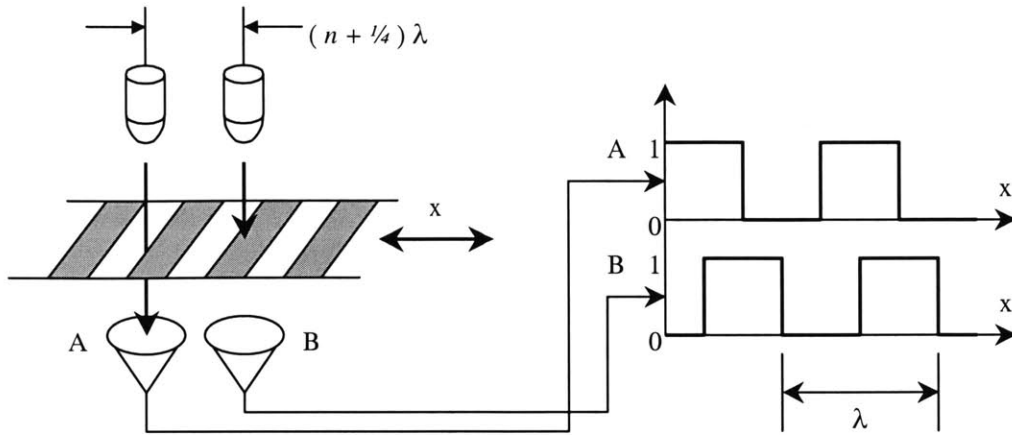


Figure 3-4: Optical encoder operation. Spacing between light sources/detectors is some whole multiple of the grating spacing ( $n \cdot \lambda$ ), plus  $\lambda/4$

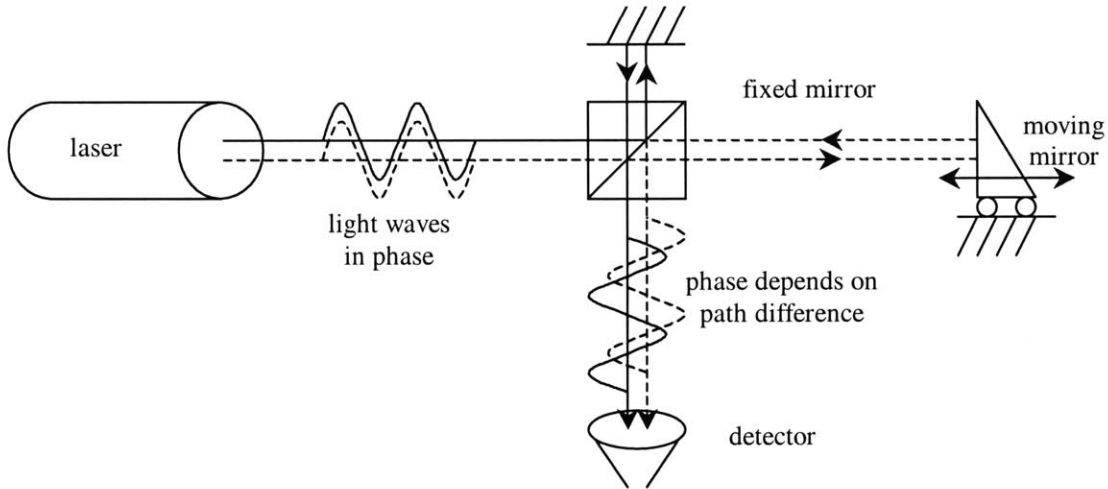


Figure 3-5: Laser interferometry component arrangement (simplified)

interfere with each other depending on the difference in the two path lengths. By placing an optical sensor in the path of the recombined beam, and measuring the rise and fall in intensity, path length differences of fractions of a wavelength can be measured. By counting rises and falls, large motions can be tracked. Very precise placement and alignment of the components must be ensured to reliably measure position. For a minimally invasive surgical (MIS) instrument, the measurement beam could pass down the shaft of the tool, reflect off a small mirror attached to the moving tip, and provide position measurements. The optics and associated electronics can be expensive.

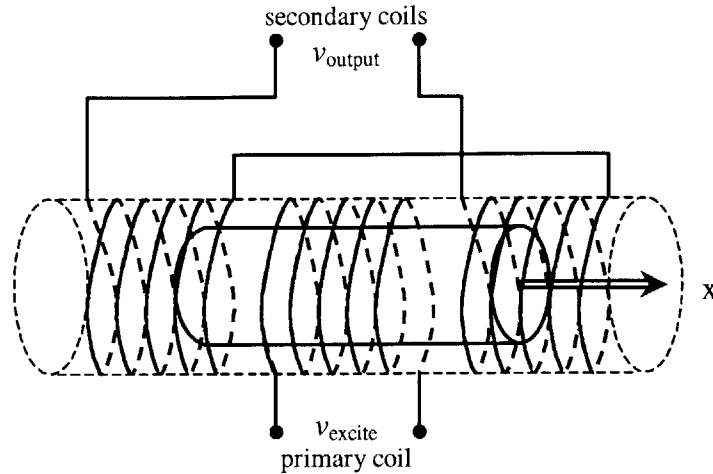


Figure 3-6: LVDT component arrangement and operation

### 3.3.3 Linear variable differential transformers (LVDTs)

A transformer functions because current passing through one set of windings induces a magnetic field, which in turn induces a current in a second set of typically interleaved windings. The induced current is a function of the mutual inductance between the windings, which can be varied by changing the position of ferrous core elements within the windings (see figure 3-6).

An LVDT uses this principle to measure position. A ferrous core, attached to the moving element, is placed within the windings of the LVDT. An alternating current is passed through the primary windings. The direction and magnitude of the current induced in the secondary windings depends on the position of the core piece. Within a small range near the mid-point of device, the relationship between core position and induced voltage (measured across the secondary winding terminals) is linear.

## 3.4 Force sensor options

A means for measuring applied force is also required for a force-displacement measurement tool. Many commercial force sensors make use of a flexible member of some geometry, and a strain gauge sensor to determine its deformation under loading. Another class of sensors uses a piezo-electric element, effectively the inverse

of the actuators described above. When loaded in the proper direction, the charge developed across the sensor can be measured.

One example of a strain gage-based sensor, the Cooper Instruments & Systems LPM 562 500G, is shown schematically in figure 3-7a. This sensor uses a micro-machined silicon diaphragm, with piezo-resistors mounted near its edge. The piezo-resistors are connected in the form of a full-bridge Wheatstone bridge to maximize the response to loading. A ball bearing ensures that loading is normal to the diaphragm, minimizing off-axis effects. It can only be used to measure compressive forces because tensile loading would cause the ball-bearing to leave the surface of the diaphragm. For the normal indentation tests described in chapter 2, this is not a concern.

Many piezo-electric sensors are available, but few commercial devices were located that would fit within the envelope defined by the 12mm minimally invasive entry port, and fewer designed to measure forces in the Newton to sub-Newton range. A typical sensor is shown in figure 3-7b. This sensor, a model 9211 from Kistler Instrument Corp., at 6mm in diameter would easily fit inside even a 10mm instrument, but its lead wires extend from the side (a common feature) preventing its use near the tip of the instrument. The model 9207 has leads extending from the back end, but is much larger, so placing it near the tip of the actuated indenter is difficult. As will be described further in the next section, other placement options exist, but these are non-optimal, especially when compared with the solution that was chosen. Some piezo-electric plastic sensors are also available<sup>4</sup>, but no suitable stock commercial versions were found.

Before the Cooper Instruments device was located, another concept for a force sensor was developed for the TeMPeST 1-D, shown in figure 3-7c. This sensor would use two fixed-fixed cantilever beams with silicon strain gages mounted at points of maximum strain, again wired in the form of a full Wheatstone bridge. Lead wires would extend along the axis of the sensor, rather than out the side. Development was discontinued before completion because the Cooper sensor satisfied the requirements, and cost significantly less in parts and time required for completion. This device may

---

<sup>4</sup>e.g. Measurement Specialties, Inc., Valley Forge, PA

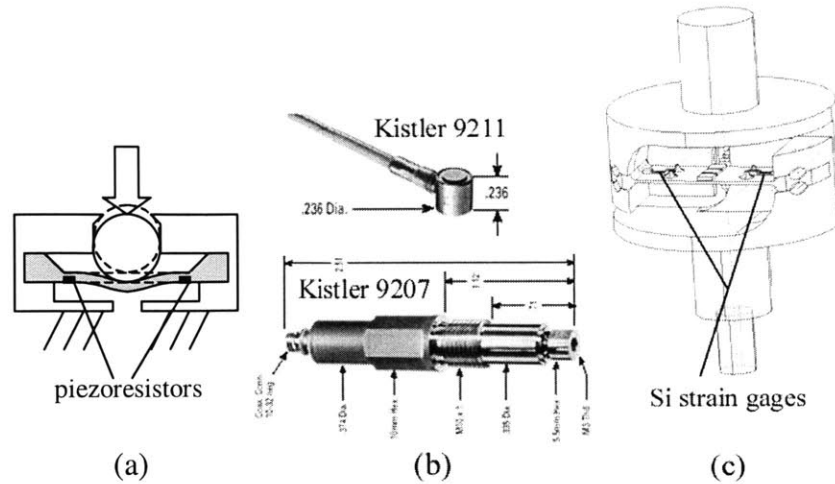


Figure 3-7: Examples of force sensor designs: (a) micro-machined piezo-resistive diaphragm, (b) piezo-electric sensors [21], (c) custom designed sensor with silicon strain gages

be developed further, as it could be used to measure both compressive and tensile loads, which would be interesting to apply to examine the properties of tissue without any pre-loading.<sup>5</sup>

### 3.5 System layout options

With a choice of sensors and actuators comes the question of arrangement and placement of the components. Some of the options that were considered are shown in figure 3-8.

The collocated design permits the closest placement of sensors to the tip where loads and displacements are applied to the tissue. Minimizing the mass of elements between the force sensor and the tip reduces inertial loads being measured by the force sensor. Since force sensors are typically very stiff compared with the expected values for the organs, there would be little error between the position of the actuator and that of the tip on the other side of the force sensor, so position sensor placement is not critical.

<sup>5</sup>This would, of course, require the development of some method for attaching the indentation tip to the tissue, which, as described earlier, is problematic, and perhaps another topic for further development.

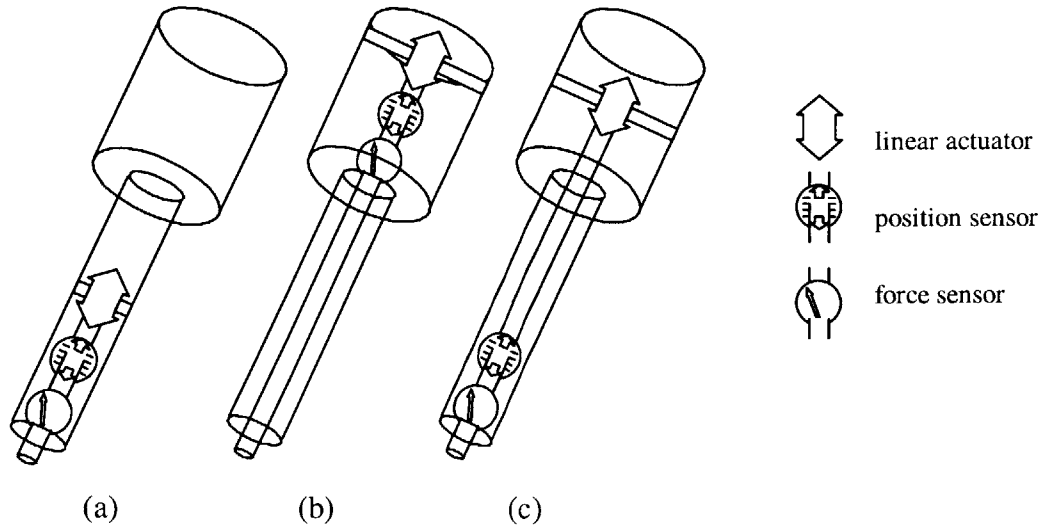


Figure 3-8: System layout options: (a) collocated sensors/actuator, (b) external sensors/actuator, (c) external actuator/internal sensors

The second design places all of the major components outside of the shaft of the tool. This permits the use of more powerful actuators, potentially with large ranges of motion. Flexibility in the shaft driving the tip would be an issue, as buckling would drive the shaft against the wall of the tube, and would reduce the accuracy of positions measured at the actuator. In addition, the mass of the indenter shaft would cause additional dynamics to be measured by the force sensor (i.e. the inertial load of the shaft), which would have to be modeled and removed during data analysis.

Placing the actuator at the external end of a long shaft, while the sensors remain within the main tube would solve one of the problems of design (b), in that the reaction force of the tissue is measured directly, rather than including the inertial load of the moving shaft. Unlike design 1, a much stronger actuator would be needed to drive the long shaft and all of the sensors at high frequencies. More importantly, if the shaft of the tool were to be sterilized, separately from the handle, both mechanical and electrical connections would be required, complicating the mechanism.

The first design argues for a voice coil actuator, as it can be compact, yet yield a range of motion comparable to its size. A piezoelectric stack, on the other hand, would need to be exceedingly long to accomplish millimeter-scale motions. Safety issues also argue for the voice coil; low voltages drive the coil, which are not typically

dangerous to living organisms (though large currents can be generated), while piezoelectric elements require large voltages, which could generate large currents passing through the tissues should something critical fail.

The final design for the TeMPeST 1-D makes use of the co-located design concept, a voice-coil motor, and commercial force sensors and LVDTs.

### 3.6 TeMPeST 1-D design details

Figure 3-9 shows the complete TeMPeST 1-D sensor/actuator package, in both assembled form, and with the moving core elements and flexures shown separately. Figure 3-10 shows an “exploded” view of all of the parts, prior to assembly. The instrument makes use of a custom-made voice-coil linear actuator to drive the indenter. The position of the tip is measured with an LVDT sensor (Schaevitz<sup>6</sup>, 099 XS-B) mounted in the tool. While the voice coil output is a force, because the force acts on the indenter mass and pushes against the stiffness of the flexural support bearings, the actual force exerted on the tissue will differ from the commanded value. For this reason, a force sensor (modified Cooper Instruments & Systems<sup>7</sup> LPM 562 500G) placed at the indenter tip is used to determine the actual load imposed on the tissue. In the current version of the device, a small preload must be applied to the tissue to ensure that contact between the tip and the tissue is maintained. In future revisions, a suction or adhesive system may be implemented so that measurements with zero mean force can be made. In addition, with the Cooper force sensor, only compressive loading can be measured, as will be described.

Typical signals that the TeMPeST 1-D can impose on the tissue include sinusoids and chirps within the TeMPeST 1-D bandwidth, steps and saturating ramps, and other force profiles, depending on the type of analysis required (e.g. measuring frequency response or time domain analysis). A Gateway<sup>8</sup> Solo 366MHz Pentium II laptop with a docking station (figure 3-11) provides the control and data acquisition

---

<sup>6</sup>Hampton, VA

<sup>7</sup>Warrenton, VA

<sup>8</sup>North Sioux City, SD

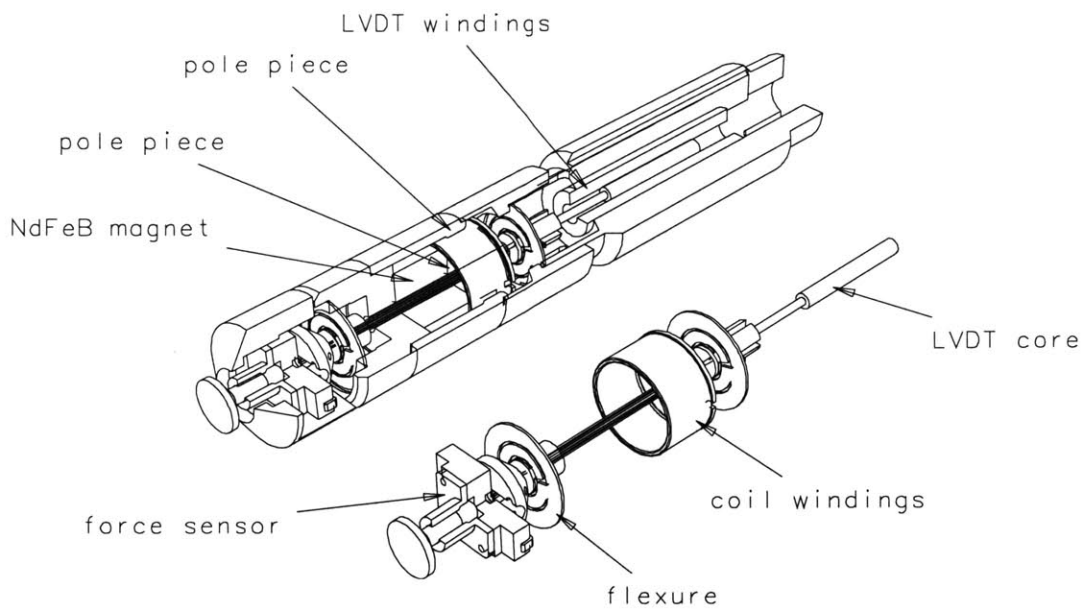


Figure 3-9: TeMPeST 1-D sensor/actuator package fully assembled (left) and moving core alone, mounted on flexures (right)

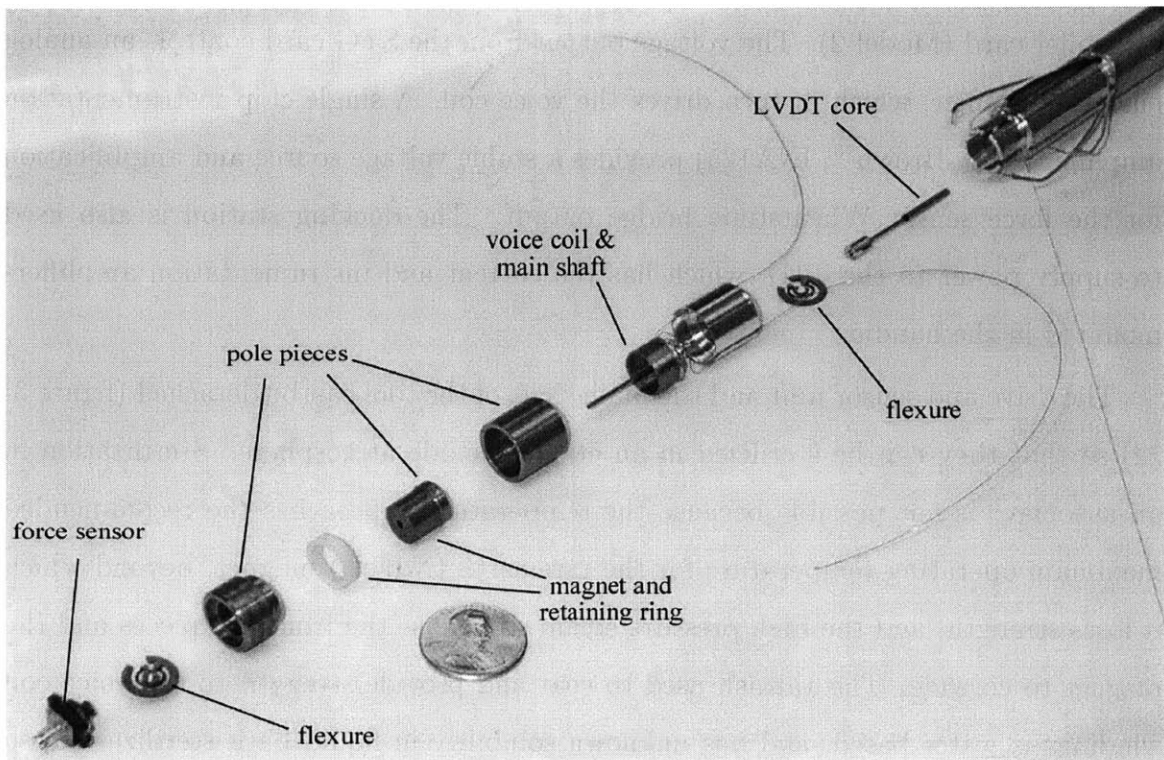


Figure 3-10: Sensor/actuator components.

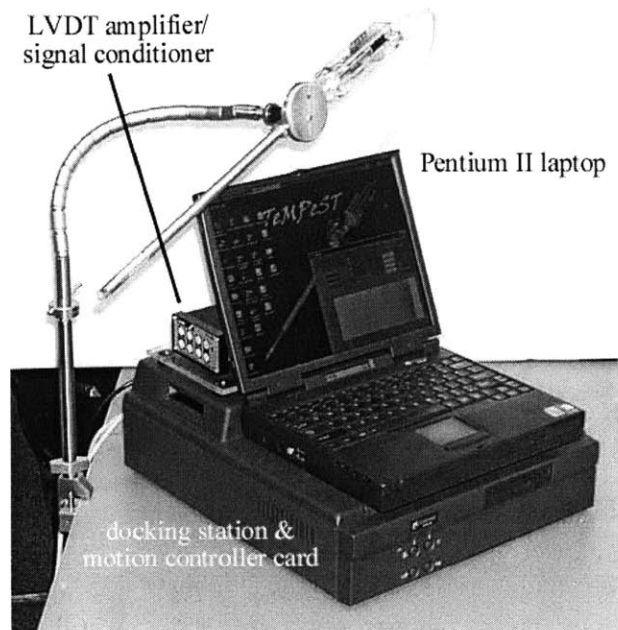


Figure 3-11: TeMPeST 1-D system components

interface to the device through a Servo To Go, Inc.<sup>9</sup> (STG) eight channel motion controller card (Model 2). The voltage output from the STG card controls an analog current amplifier, which in turn drives the voice coil. A single chip instrumentation amplifier (Burr-Brown<sup>10</sup>, INA125) provides a stable voltage source and amplification for the force sensor Wheatstone bridge output. The docking station is also used to supply power to the T1D, which has the current and instrumentation amplifiers mounted in the handle.

The drive and sensor unit and the main shaft of the tool can be detached (figure 3-12) so that they can be sterilized in an ethylene oxide atmosphere. Sterilization in an autoclave is not possible because the temperature approaches the recommended maximum operating temperature for the rare earth (NdFeB) magnet, beyond which it loses strength, and the high pressure steam will cause the iron pole pieces and the magnet to corrode. The varnish used to coat and provide strength to the voice coil windings is water based, and has unknown solubility in liquid bath sterilization, so

---

<sup>9</sup>Redmond, WA

<sup>10</sup>Tucson, AZ



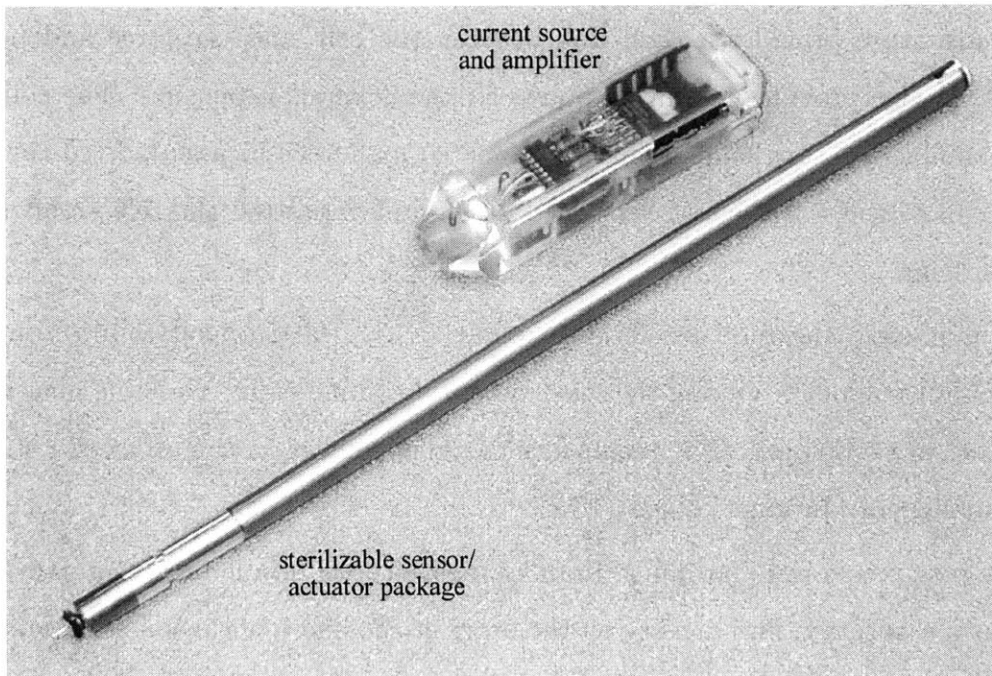


Figure 3-12: Separable components so that sensor/actuator package can be sterilized.

this method is not recommended.

A flexible arm which can be attached to an operating table was used to hold the TeMPeST 1-D. Since fine positioning of the TeMPeST 1-D with the arm was difficult, a manual cam actuator with a range of motion of 0.5" was constructed to provide this capability.

### 3.6.1 Voice coil and suspension design

No commercially available voice coil or solenoid actuators were found that would support the size limitations, desired range of motion and mounting of both position and force sensors. For this reason, an actuator was designed specifically for the TeMPeST 1-D.

Constraints on and specifications for the actuator include a maximum diameter of 12mm, a desired range of motion of  $\pm 0.5\text{mm}$ , the ability to apply approximately 0.1N force, heating and temperature considerations, and the limits of available materials.

As was shown in figure 3-11a, the voice coil actuator is made up of a cylindrical magnet, an internal and external pole pieces, and the armature. The central shaft

of the armature provides a rigid link between the coil, and the force and position sensors. It also provides mounting points for the flexural suspension. The coils used were manufactured by hand, using a wax coated mandrel which supported the shape of the coil as the water-based varnished dried, and permitted the release of the coil upon heating.

To maximize the flux density in the gap, a rare-earth, neodymium-iron-boron (NdFeB-50) magnet<sup>11</sup>, among the most powerful commercially available materials at this time, was employed. The remanence of the magnet is on the order of 1.4T, with a nominal energy product of 50MGOe.

The pole pieces were fashioned from low carbon steel (grade indeterminate). Pure iron has a saturation flux density on the order of 2T, and low carbon steel somewhat lower than this. Since the flux density of the magnet was already close to that of the pole piece saturation, the focusing arrangement (figure 3-2) was not necessary. Also, due to space constraints, the radially oriented ring magnet type was also not used. In addition, such a magnet would have a very short effective length, and would provide a lower flux density in the gap than a longer magnet, oriented as was done in the TeMPeST 1-D. To prevent any “bottle-necks” in the magnetic circuit due to saturation of the pole pieces, all of the components were designed so that the cross sectional area perpendicular to the magnetic field lines was greater than or equal to the cross sectional area of the magnet.

Modeling of the magnetic field and the force on a coil with a given current density was performed using a “free-ware” magnetic field simulator called FEMM<sup>12</sup>, a finite element modeling tool which can be used to analyze 2-D planar and axi-symmetric geometries. This tool permitted iteration of the design of the actuator to maximize the gap flux density while staying within the maximum diameter limits. Figure 3-13 shows a typical result from the simulation showing flux density and the magnetic field lines throughout the circuit. Figure 3-14 shows the force/current constant ( $K_{cf}$ )

---

<sup>11</sup>Magnet Sales and Manufacturing, Culver City, CA

<sup>12</sup>Finite Element Method Magnetic, version 2.1, ©1999, Dr. David C. Meeker. <http://members.aol.com/dcm3c>, 2 Jan 2001, last update 21 Nov. 2000

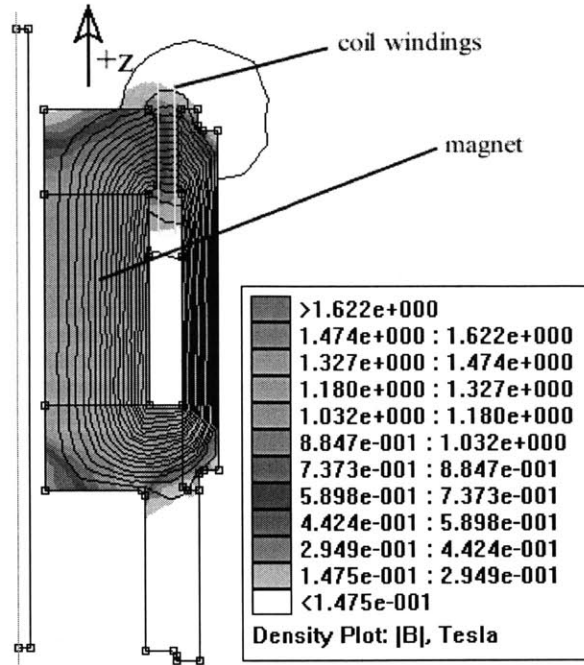


Figure 3-13: Typical FEMM flux density/field line plot.

for a coil wound with 34 gage insulated magnet wire. As can be seen,  $K_{cf}$  is nearly constant across a range of motion of greater than  $\pm 0.5\text{mm}$ , satisfying the range of motion requirement.

To provide friction-free actuation, a flexural bearing system was developed for the TeMPeST 1-D. Sliding bearings introduce friction between the moving surfaces, and ball or roller bearings are not generally suited for very small, repetitive motions. Hydrostatic bearings (oil, water or air) were considered, but have additional difficulties such as sealing the system to prevent contamination of the organs and dealing with the pressurized environment in laparoscopic surgery (in addition to the precision manufacture of more parts). Mounting the moving elements on flexures eliminates these problems. A number of designs were considered for the flexures, and an example of the final version is shown in figure 3-15.

While flexures provide friction-free motion, this comes at the cost of exerting a restoring force on the actuator. The applied force for a given displacement is less than that generated by the voice coil alone, and is zero when the displacement is equal to the voice coil output force divided by the flexure spring constant. Further,

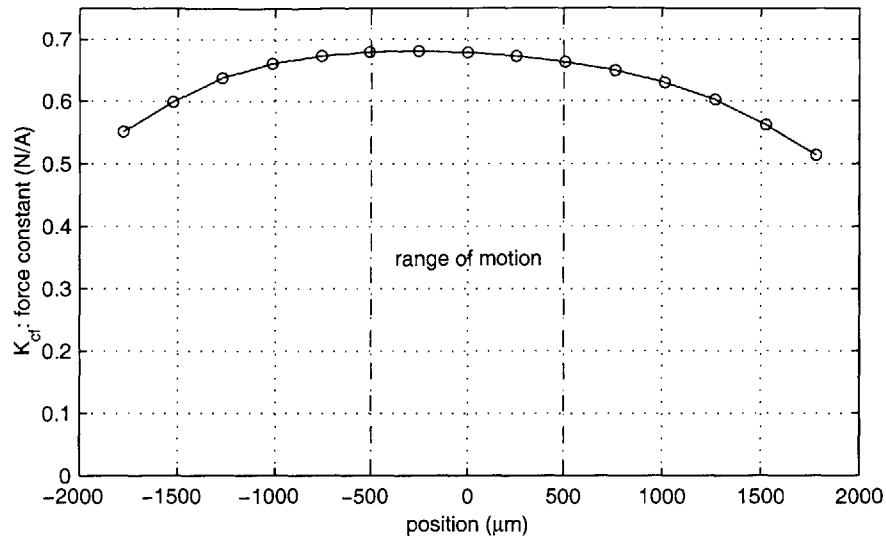


Figure 3-14: Force constant vs. position from model.

combining the mass of the moving elements with the elastic suspension creates a second order system, which will have undesired large amplitude oscillations when driven at or near its resonant frequency. A trade-off exists between minimizing the current needed to exert a desired force, which argues for low flexure stiffness, and achieving a resonant frequency above the frequency range of interest, which requires a higher spring constant (and low mass). From early mass estimates for the actuator and a desired minimum resonant frequency around 100Hz, the flexures were designed to have a minimum stiffness of approximately 100N/m.

The design chosen for the TeMPeST 1-D is a fixed-fixed cantilever design, clamped to the moving armature and fixed housing at the inner and outer bosses respectively, with the cantilever wrapped around the central axis of the armature. To provide flexibility in design, a series of flexures was manufactured, each version with a different cantilever length, and thus a different stiffness.

On its own, a single flexure would tend to bend out-of-plane when an axial load is applied, and would thus exert a bending moment on the armature away from the axis of the actuator. As shown in figure 3-9, two flexures are used to support the armature, so the lateral stiffness of each flexure prevents the other from bending off-axis, thereby achieving the desired motion.

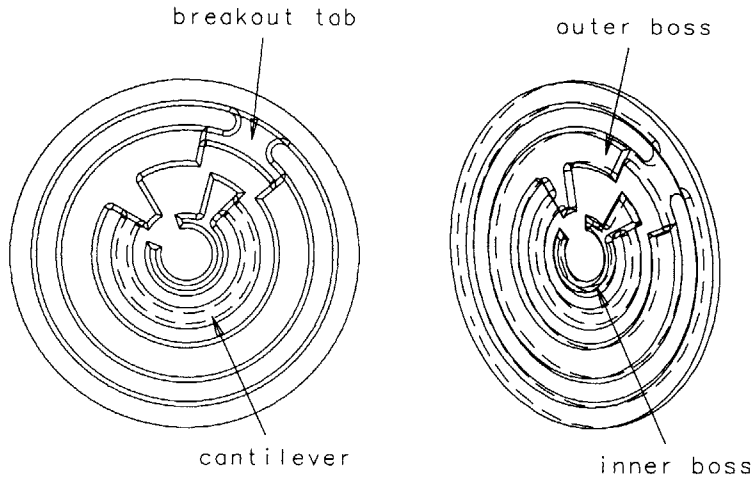


Figure 3-15: Flexural suspension

The flexures were manufactured by photo-etching 0.015" thick T2024-T3 aluminum.<sup>13</sup> Other materials were considered, including copper and copper alloys, as well as steel. Aluminum was chosen as it had the lowest elastic modulus of the available materials; a lower modulus permits the design of slightly larger elements, which are less sensitive to the tolerance limits of the mask alignment process. Since photo-etching permits the simultaneous manufacture of a number of parts, a series of flexures with a range of stiffnesses was created, providing flexibility in tuning the behavior of the actuator.

The masks used to create the flexures are included in appendix B. Isotropic etching of the aluminum produced components which have full thickness at the inner and outer mounting bosses, but only 0.005" thick cantilevers. The masks include allowance for breakout tabs to prevent the flexures from separating from the rest of the sheet during etching.

Finite element analysis was performed using SDRC I-DEAS Master Series 7 to estimate the minimum stiffness of the longest cantilever design, and verify that the normal range of motion would not exceed the fatigue strength of the alloy.<sup>14</sup> A typical result is shown in figure 3-16, as are expected force-displacement data, showing that the flexures behave like linear springs within the normal range of motion.

<sup>13</sup>MicroPhoto, Inc., Roseville, MI

<sup>14</sup>140Mpa for 500,000,000 cycles [2]

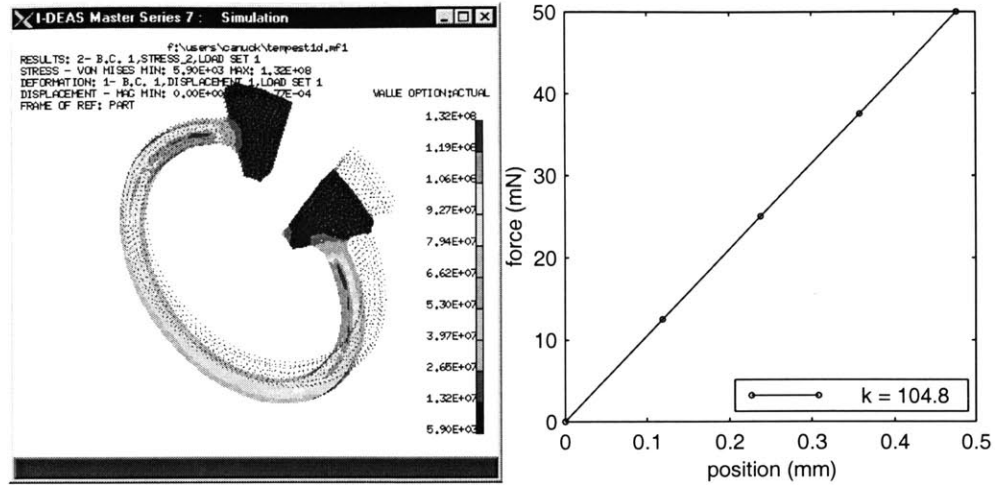


Figure 3-16: Single flexure FEA output: spring constant = 105N/m. For applied force = 0.05N,  $z=0.48$ mm, maximum Von Mises stress = 132.4MPa

Total combined stiffness for the two flexures plus the six lead wires connecting the force sensor and voice coil to the amplifier and drive circuitry is approximately 275N/m (see section 4.2.7), indicating that the model agrees closely with the fabricated components used in the TeMPeST 1-D, and that the components match the desired stiffness.

### 3.6.2 LVDT

The Schaevitz, 099 XS-B LVDT was used unmodified, with the LVDT coils mounted in the aluminum housing (figure 3-11a), and the core element attached to the moving armature of the voice coil actuator. This LVDT has a nominal linear range of motion of  $\pm 2.4$ mm, with a rated linearity of 1.0% of full scale maximum. Careful placement of the photo-etched flexures automatically aligns the armature so that the LVDT core does not rub against the inner surface of the coils.

The LVDT drive oscillation and signal conditioning of the response are performed by a Schaevitz ATA 2001 signal conditioner. Front panel controls permit gain, phase and offset adjustments, which are stored in non-volatile memory. It provides an analog bipolar voltage output with a range of  $\pm 10$ V.

### 3.6.3 Force sensor

A Cooper Instruments LPM 562 500G force sensor measures the force exerted on the tissue. The device makes use of a micromachined silicon diaphragm with piezoresistors embedded near the edges. The resistors and embedded circuitry create a full bridge Wheatstone circuit (figure 3-17).

Silicon diaphragms can be used as pressure sensors, where a pressure difference across the diaphragm causes it to deform elastically. The deformation causes a change in the resistance of the piezoresistors, proportional to the local strain. To be used as a force sensor, a ball bearing held in a collar pushes against the mid-point of the diaphragm, generating a near-point force. Whether a distributed pressure or a point load is applied, the bridge circuit will respond, and the load can be detected.

Because the ball bearing does not rise very far above the sensor package, the modified version shown in figure 3-17 was constructed. The base of the package, the silicon structure and the ball bearing were retained, and an additional collar and indenter with a right circular tip were added. The indenter is fixed to the ball bearing with epoxy; the diameter of the additional collar is smaller than the ball bearing, so no components can fall out during use. In turn, the diameter of the indenter tip shaft is slightly smaller than the collar diameter, so that a free sliding fit is achieved, thereby avoiding significant friction that would corrupt the force measurement.

Since no method was available to permit adhesion or other non-damaging attachment to tissue, tensile loading is not used. For this reason, the modified force sensor, which detects only compressive forces, is acceptable for the measurements.

### 3.6.4 TeMPeST 1-D electronics

The TeMPeST 1-D body houses two circuits: one to drive the current in the voice coil actuator, and one to balance and amplify the force sensor output. The system implemented is shown in figure 3-18. The circuits were assembled on a perforated protoboard using wire-wrap sockets to permit easy placement (or replacement) of the components.

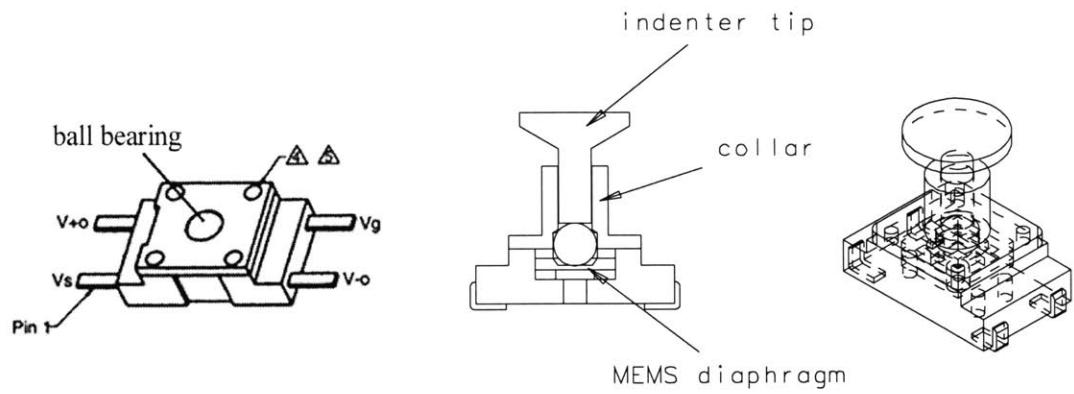


Figure 3-17: Modified force sensor components

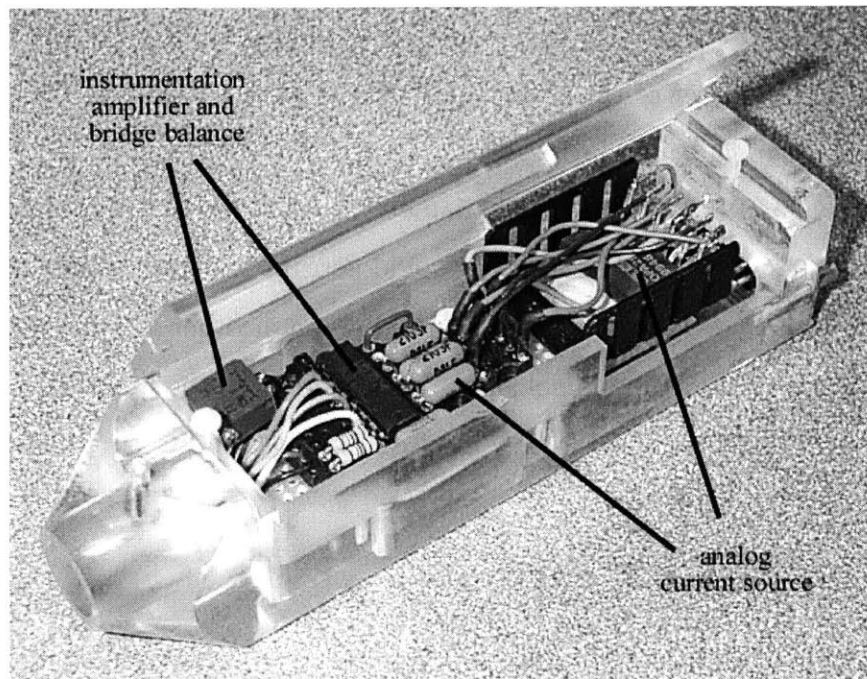


Figure 3-18: TeMPeST 1-D body, housing force sensor balance and instrumentation amplifier circuits, and the current source for the voice coil



In addition to the electronics in the instrument, a laptop and a docking station with a motion controller card provide for control, data acquisition and analysis.

### Analog current source

The voice coil actuator converts current passing through conductors in a magnetic field into force. The digital to analog converter (DAC) on the motion controller card can only supply a few mA of current, so an additional power source and voltage to current converter is necessary. Power can be supplied from the docking station power supply, providing  $\pm 12\text{V}$  and ground connections. Voltage controlled current sources are commercially available, but [17] describes a simple one-chip analog current source which suits the needs for the prototype TeMPeST 1-D. Figure 3-19 shows a modified version of the circuit. The original version holds  $R_1/R_2 = 1$ , but by altering the ratio, the gain of the system can be changed, independently of the value of the sense resistor,  $R_S$ . Since power dissipation in the sense resistor varies as  $I^2R$ , a smaller resistor reduces heating, and wasted power;  $0.5\Omega$  power resistors were available on hand and one was used in the final design. However, since in the original design, output current is proportional to  $V_{in}/R$ , smaller resistors increase the voltage to current gain. Since the DAC range is  $\pm 10\text{V}$ , and the output current will be typically smaller than  $500\text{mA}$ , the modified gain section of the circuit is necessary to scale down the large voltage to a proportionally small current.

The most important component of this circuit is the high-power operational amplifier, which must be able to supply the full current. The Barton-Barr OPA2544 is a dual power op-amp chip, one half of which was used as the power op-amp, while the other serves the role of buffer amplifier, and carries only minimal current.

For this circuit, the relationship between input voltage and output current is shown in equation 3.2. With an input voltage range of  $\pm 10\text{V}$  from the STG card, the maximum current that the source will generate is  $500\text{mA}$ . Power dissipation in the power-op amp is given by equation 3.3. Maximum dissipation is  $5.9\text{W}$ , and coincides with the  $10\text{V}$  maximum input voltage. This is a non-trivial amount of heat, so the power op-amp chip was mounted to a heat sink to prevent overheating, and windows

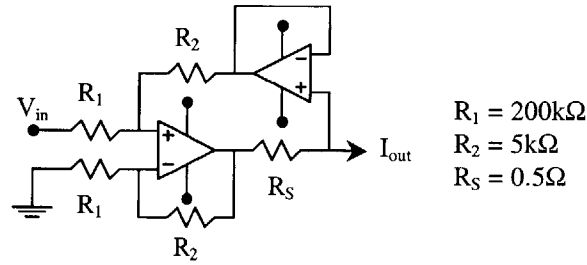


Figure 3-19: Direct voltage to current amplifier circuit

were designed into the housing to permit natural convection to carry heat away. As will be apparent in chapter 6, in all experimental cases current was only supplied for periods on the order of 30 seconds or less, and maximum current was never used; heating was not a significant concern.<sup>15</sup>

$$\begin{aligned}
 I_{out} &= \frac{R_2}{R_S R_1} V_{in} \\
 &= \frac{1}{20} V_{in} \tag{3.2}
 \end{aligned}$$

$$\begin{aligned}
 P &= \left(12 - \frac{R_2}{R_1} V_{in}\right) \frac{R_2}{R_S R_1} V_{in} \\
 &= \frac{3}{5} V_{in} - \frac{1}{800} V_{in}^2 \tag{3.3}
 \end{aligned}$$

### Force sensor bridge and instrumentation amplifier

The force sensor described in section 3.6.3 is a Wheatstone bridge design which uses a fixed voltage across the source and ground terminals. Its output is the difference between the voltages at the  $V_+$  and  $V_-$  terminals. Since the differential signal is typically on the order of millivolts, it must be amplified so that quantization noise in the ADCs and additional noise picked up by the wires between the sensor and the ADCs are not significant. In addition, the force sensor bridge circuit is not completely balanced, so a balance circuit with a potentiometer was added so that the offset voltage could be zeroed and to compensate for any effects of room temperature

<sup>15</sup>Even after minutes of driving the voice coil with a constant current of up to 200mA during calibration and other tests, the heat sink never became too hot to touch, remaining below about 45°C.

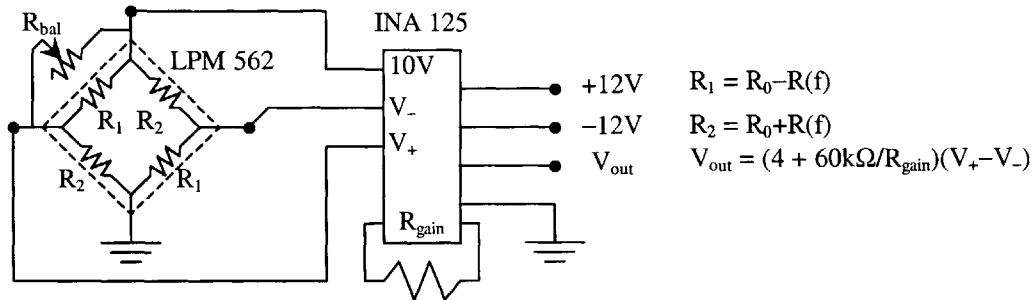


Figure 3-20: Force sensor, balance and instrumentation amplifier circuit.

variation.<sup>16</sup> The circuit diagram is shown in figure 3-20.

As with the current source, a single chip design was possible using the Burr-Brown INA125, which includes a stable voltage source to provide the supply voltage to the bridge, and an instrumentation amplifier with a gain that can be set by using one additional resistor. The output is linear with force over the range of interest, as described in section 4.2.3.

## Computer and motion controller

To generate the open loop trajectories, control the system, and acquire and analyze data, a laptop, docking station and motion controller card were purchased. Important applications installed on the laptop include Microsoft Visual C++ and Mathworks MATLAB. MSVC++ was used to create the real-time control and data acquisition application, while the graphical user interface, trajectory generator and analysis segments were developed in MATLAB. Use of a laptop permitted convenient off-line (and off-site) data analysis.

The Gateway 2000 laptop was selected in part because it is compatible with a full docking station which has two dual ISA/PCI interface card slots. The power source supplying the docking station and the laptop (when docked) was modified to supply power to the TeMPeST 1-D as well.

The interface card is an eight channel ServoToGo model 2 ISA motion controller.

<sup>16</sup>Piezoresistive strain gages are more sensitive to temperature than normal metal foil or wire gages, though since the resistors will vary roughly in line with each other, temperature variation is a second order effect.

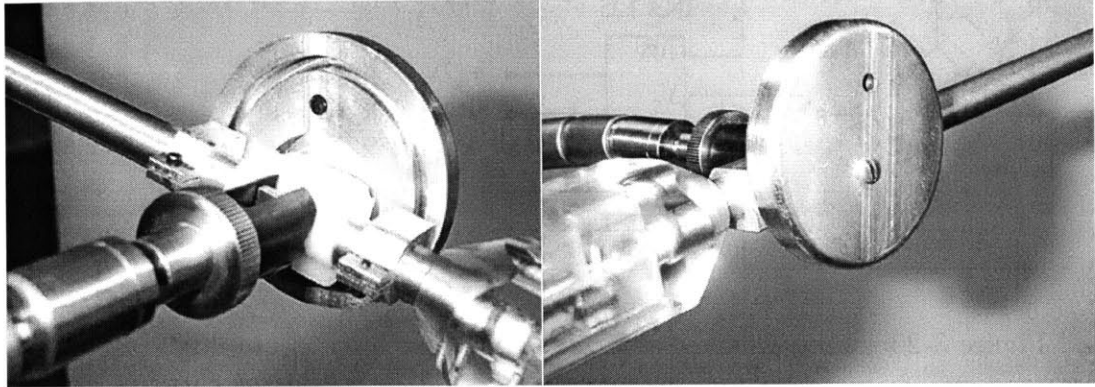


Figure 3-21: Modified Mediflex laparoscope/instrument holder and fine positioning cam. The cam provides fine position control over a range of 0.5”

It supports up to eight 13-bit ADC channels, eight 13-bit DAC channels, four optical encoders and 32 bits of digital I/O. While not all of this functionality is necessary for the TeMPeST 1-D, it is anticipated that this same system will be used to support additional instruments, such as the TeMPeST 3-D, described in appendix C. The input and output range are  $\pm 10V$ , so the resolution of the ADC and DAC channels is 2.44mV.

### 3.6.5 Flexible arm and fine positioning cam

To rigidly attach the TeMPeST 1-D to an operating table, a Mediflex<sup>17</sup> Bookler laparoscope/instrument holder, model no. 69045-D (see figure 3-11b), which is designed to support a laparoscope or other instruments, was employed. While it can be arbitrarily positioned, locking the arm in place requires tightening of a nut to create enough friction between the links to prevent motion. Using the arm to position the tip of the TeMPeST 1-D to the sub-millimeter accuracy required to contact soft tissue was not found to be possible, so a manual cam system was developed to permit precision positioning. Figure 3-21 shows the flexible arm, and a close up of the fine positioner.

The fine positioner consists of a sliding joint between the arm and the cam made of Delrin to provide a guide for axial motion. Attached to the shaft of the TeMPeST

---

<sup>17</sup>Islandia, NY

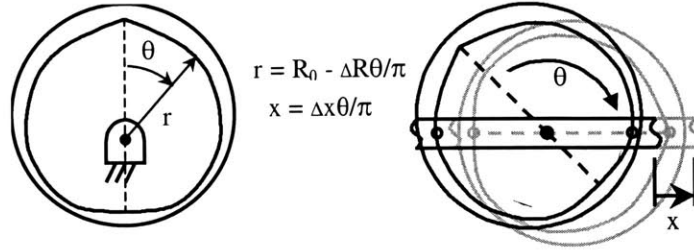


Figure 3-22: Details of fine positioning cam geometry. Pins on TeMPeST 1-D shaft follow cam in disk mounted to Mediflex arm. In this configuration, clockwise rotation about the axis generates linear motion of the shaft towards the right.

1-D above and below the sliding joint are two pins which act as cam followers, and drive the motion of the TeMPeST 1-D shaft. The cam followers ride in a pair of helical grooves cut into an aluminum disk which turns on a screw attaching the disk to the Mediflex arm.

The shape of the cam is designed so that the length of a straight line passing through the pivot point, from one half of the cam path to the other has a constant length. This length is the same as the distance between the two cam follower pins. By rotating the disk, the proportions of the line segments between the cam followers shifts from lying above the pivot to below. A rotation of  $180^\circ$  results in a fine motion of 0.5". Assuming that the smallest rotation that a user can generate is on the order of  $2^\circ$ , then the TeMPeST 1-D can be positioned to better than 0.2mm. Figure 3-22 illustrates the geometry and motion of the fine positioner.



# Chapter 4

## System modeling and characterization

This chapter will begin with the development of lumped parameter models which can be used to examine the behavior of the TeMPeST 1-D, both in free motion, and in contact with some unknown material. This modeling will permit the extraction of force-displacement models of the tissue from the measured force and displacement from the system, and from there, the determination of material properties.

The system model requires the determination of a number of parameters to describe each of the major elements, including the force and position sensors, the voice coil and its suspension. Experiments to calibrate and characterize each of these subsystems will be described and their results presented.

### 4.1 TeMPeST 1-D System Modeling

The lumped parameter models for the TeMPeST 1-D will be developed from the simplest, second order description for the voice coil actuator alone, to more complex models including the dynamics of the TeMPeST 1-D mounted on the articulated arm and simple models of the tissue.

### 4.1.1 Voice coil actuator model

The dominant elements of the voice coil are the stiffness of the flexures and the mass of the armature, which includes the coil, the force sensor, and the core of the LVDT. For this model, the mass is estimated based on the volume and density of the materials used in the armature and the stiffness on that calculated from the finite element model of the flexures. Calculating the damping from first principles based on viscous forces due to air in the actuator or material damping properties would be extremely difficult. However, for the purposes of modeling, knowing that damping from air would be small, a damping ratio of 5% is assumed. Figure 4-1 shows the lumped parameter model for this system, and its frequency response. Equations 4.1 are the state space model of the system.

$$\begin{aligned} \begin{pmatrix} \dot{x} \\ \ddot{x} \end{pmatrix} &= \begin{pmatrix} 0 & 1 \\ -\frac{k}{m} & -\frac{b}{m} \end{pmatrix} \begin{pmatrix} x \\ \dot{x} \end{pmatrix} + \begin{pmatrix} 0 \\ \frac{1}{m} \end{pmatrix} f_{coil} \\ x_{meas} &= \begin{pmatrix} 1 & 0 \end{pmatrix} \begin{pmatrix} x \\ \dot{x} \end{pmatrix} \end{aligned} \quad (4.1)$$

### 4.1.2 Tissue contact I

Assuming now that the TeMPeST 1-D is rigidly mounted while in contact with tissue with transfer function  $H(s)$ , a more complex model describes the response. The tip position and force measured at the tip can be determined analytically. As shown in the sequence of equations 4.2 which follow, the ratio of the transforms of position to force is equal to the transfer function of the tissue, permitting reconstruction of  $H(s)$  from position and force data. For the purposes of generating equations 4.2 and the Bode plots, a Kelvin tissue model is included in the system.



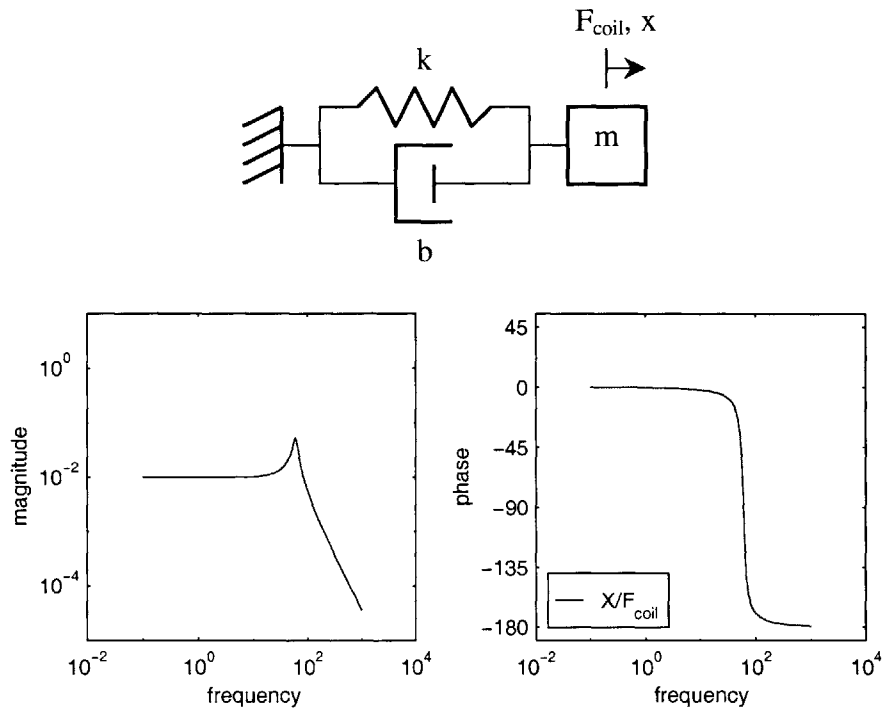


Figure 4-1: Second order model of voice coil actuator in free motion.

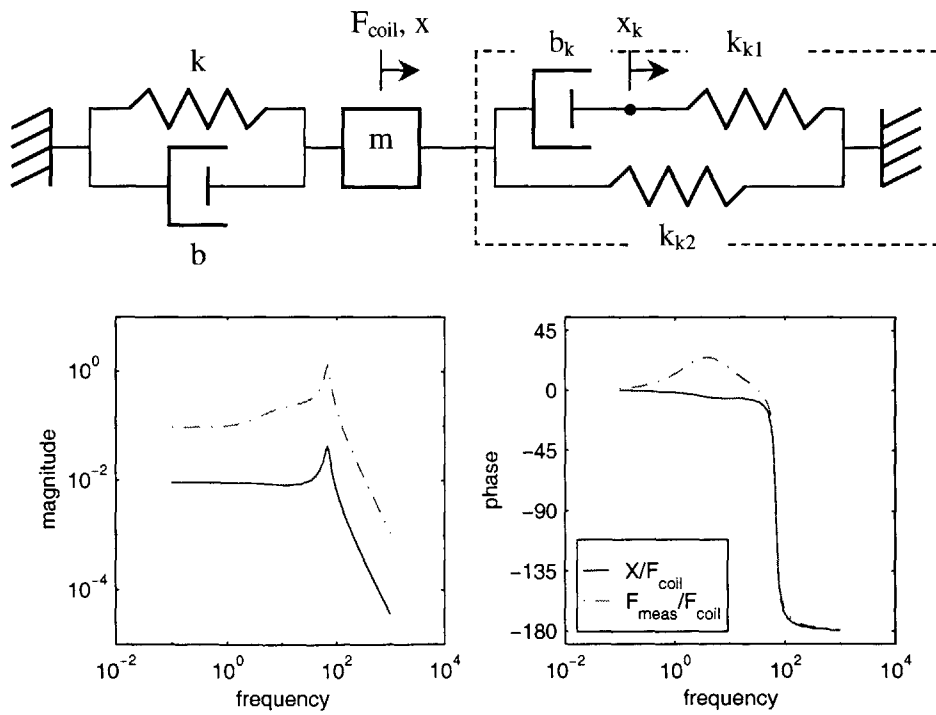


Figure 4-2: Position and measured force of voice coil actuator in contact with unknown (Kelvin) tissue.

$$\begin{pmatrix} \dot{x} \\ \ddot{x} \\ \dot{x}_k \end{pmatrix} = \begin{pmatrix} 0 & 1 & 0 \\ -\frac{k+k_2}{m} & -\frac{b}{m} & -\frac{k_{k1}}{m} \\ 0 & 1 & -\frac{k_{k1}}{b_k} \end{pmatrix} \begin{pmatrix} x \\ \dot{x} \\ x_k \end{pmatrix} + \begin{pmatrix} 0 \\ \frac{1}{m} \\ 0 \end{pmatrix} f_{coil}$$

$$\begin{pmatrix} x_{meas} \\ f_{meas} \end{pmatrix} = \begin{pmatrix} 1 & 0 & 0 \\ k_{k2} & 0 & k_{k1} \end{pmatrix} \begin{pmatrix} x \\ \dot{x} \\ x_k \end{pmatrix} \quad (4.2)$$

Transforming the equation for  $x_k$  and the output equations to the Laplace domain and continuing:

$$X_{meas}(s) = X(s) \quad (4.3)$$

$$F_{meas}(s) = k_{k2}X(s) + k_{k1}X_k(s) \quad (4.4)$$

$$sX_k(s) = sX(s) - \frac{k_{k1}}{b_k}X_k(s) \quad (4.5)$$

Solving equation 4.5 for  $X_k(s)$  in terms of  $X(s)$  and substituting the result into equation 4.4 (and dropping 's' for convenience) yields:

$$F_{meas} = \left( (k_{k1} + k_{k2})s + \frac{k_{k1}k_{k2}}{b_k} \right) X \quad (4.6)$$

And finally dividing  $X_{meas} = \mathcal{L}\{x_{meas}\}$  by  $F_{meas} = \mathcal{L}\{f_{meas}\}$  generates the desired result:

$$\frac{X_{meas}}{F_{meas}} = \frac{s + \frac{k_{k1}}{b_k}}{(k_{k1} + k_{k2})s + \frac{k_{k1}k_{k2}}{b_k}} \quad (4.7)$$

$$= \frac{1}{k_{k2}} \frac{\frac{b_k}{k_{k1}}s + 1}{\frac{k_{k1} + k_{k2}}{k_{k1}k_{k2}}b_k s + 1} \quad (4.8)$$

$$= H(s) \quad (4.9)$$

which is the same expression as was derived for the Kelvin body in section 2.1.

This is a very simple example of a system identification problem, in which the system is the tissue being studied, and the parameters describing it are desired. Using the ratio of the transforms of position and force leads first to a non-parametric graphical representation for the transfer function of the tissue. Once the non-parametric form has been determined, one can decide what sort of system best fits the observed behavior, and then determine the parameters to achieve a best fit between the model and the tissue response.

For example, for an unknown material exhibiting a Kelvin body characteristic response, the unknown parameters could be calculated from measurements of the high and low frequency asymptotes in compliance ( $c_1, c_2$ ), and by the frequency where the phase is maximum ( $\omega_m$ , in rad/sec). The relationships between these values and the parameters introduced in figure 2-3 and equation 2.5 are developed in equations 4.10 - 4.13.

$$k_1 = c_1^{-1} \quad (4.10)$$

$$k_2 = c_2^{-1} - c_1^{-1} \quad (4.11)$$

$$\begin{aligned} \omega_m &= (\tau_c \tau_r)^{-1/2} \\ &= \frac{b}{k_1} \left( \frac{k_1 + k_2}{k_2} \right)^{-1/2} \end{aligned} \quad (4.12)$$

$$b = \frac{1}{c_1 \omega_m} \left( \frac{c_1 - c_2}{c_1} \right)^{1/2} \quad (4.13)$$

The preceding equations were developed assuming that the force and position signals were continuous in time, permitting the use of the Laplace transform. For sampled data, the Discrete Fourier Transform, or the Fast Fourier Transform can be used to generate non-parametric representations of the materials in question. One method for doing this is to generate an input signal with frequency content spread over a range of interest, such as a chirp. Then the ratio of the DFTs of force and position is found, and is used as an approximation to the frequency response of the tissue.

This method, described in more detail in [11] is used in some of the characterization exercises used to determine the TeMPeST 1-D parameters later in this chapter, as well as the measurements of properties of real materials (chapter 6).

### 4.1.3 TeMPeST 1-D in free motion

The next level of complexity arises from the inclusion of the mass of the entire instrument and the flexibility of the Mediflex arm into the system. The additional kinetic and potential energy storage elements introduce two additional states into the system, beyond those in the free-motion second-order system, as shown in figure 4-3. In modeling, stiffness is taken to be that of a round cantilevered rod with length, diameter and density equal to that of the Mediflex arm. Mass is equal to that of the TeMPeST 1-D body (without armature) plus the equivalent mass of the cantilever arm. With this model, the open loop response of the motion of the indenter tip is shown in figure 4-3. In this case, the unmeasured resonant motion of the TeMPeST 1-D body introduces a small distortion to the ideal response discussed above. However, since this distortion is local for a lightly damped system (which is true for the TeMPeST 1-D and arm in free space) and because the stiffness of the Mediflex arm is large compared with the flexures, the dominant characteristics of the system are still those of the voice coil actuator. This continues to permit use of the second-order model of the actuator (equation 4.1) as a useful approximation.

$$\begin{aligned}
 \begin{pmatrix} \dot{x}_b \\ \ddot{x}_b \\ \dot{x} \\ \ddot{x} \end{pmatrix} &= \begin{pmatrix} 0 & 1 & 0 & 0 \\ -\frac{k+k_b}{M} & -\frac{b+b_b}{M} & \frac{k}{M} & \frac{b}{M} \\ 0 & 0 & 0 & 1 \\ \frac{k}{m} & \frac{b}{m} & -\frac{k}{m} & -\frac{b}{m} \end{pmatrix} \begin{pmatrix} x_b \\ \dot{x}_b \\ x \\ \dot{x} \end{pmatrix} + \begin{pmatrix} 0 \\ -\frac{1}{M} \\ 0 \\ \frac{1}{m} \end{pmatrix} f_{coil} \\
 \begin{pmatrix} x \\ x_b \\ x_{lvd} \end{pmatrix} &= \begin{pmatrix} 0 & 0 & 1 & 0 \\ 1 & 0 & 0 & 0 \\ -1 & 0 & 1 & 0 \end{pmatrix} \begin{pmatrix} x_b \\ \dot{x}_b \\ x \\ \dot{x} \end{pmatrix} \tag{4.14}
 \end{aligned}$$

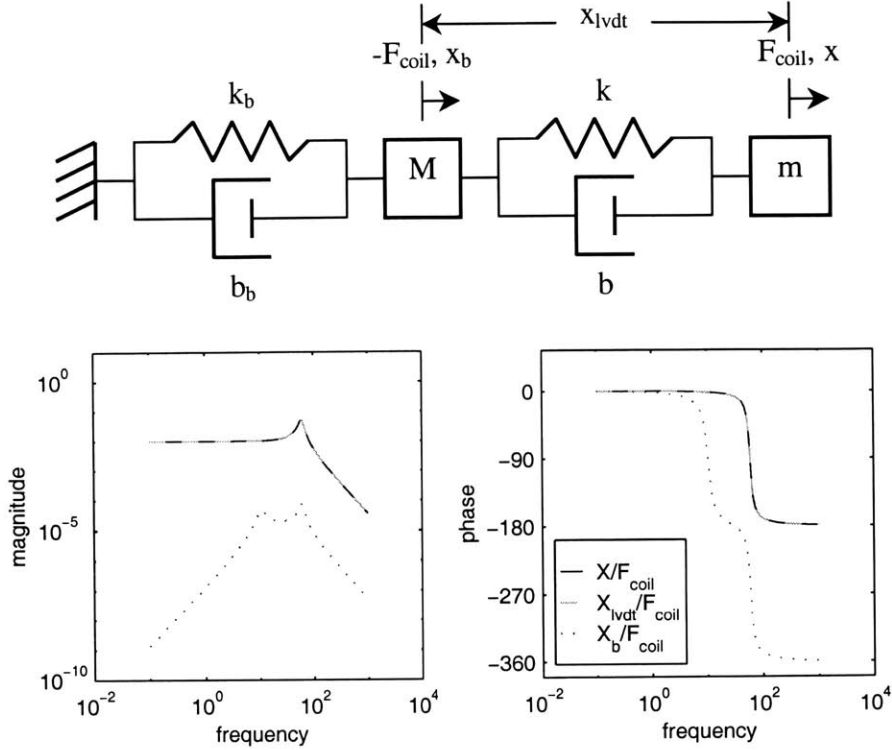


Figure 4-3: Free space tip response for TeMPeST 1-D on Mediflex arm, with base motion ( $X_b/F_{coil}$ ) shown for comparison.

#### 4.1.4 Tissue contact II

Again adding contact with Kelvin tissue to the model, the system (figure 4-4) is now 5<sup>th</sup> order, as shown in equations 4.15. As was done earlier, the ratio of the applied force and measured displacement is found, and in this case, the effect of arm resonance is clear in both the magnitude of the compliance and the phase value. The unmeasured base motion is now larger at the resonant frequency, because the applied force (and reaction from the tissue) is much larger than inertial forces due to the motion of the actuator in free motion.

Despite this larger error in the calculation for the frequency response of the tissue, since the error is still local, as discussed earlier, the gross characteristics of the tissue can be calculated based on, for example, equations 4.10 – 4.13.

$$\begin{pmatrix} \dot{x}_b \\ \ddot{x}_b \\ \dot{x} \\ \ddot{x} \\ \dot{x}_k \end{pmatrix} = \begin{pmatrix} 0 & 1 & 0 & 0 & 0 \\ \frac{k+k_b}{M} & -\frac{b+b_b}{M} & \frac{k}{M} & \frac{b}{M} & 0 \\ 0 & 0 & 0 & 1 & 0 \\ \frac{k}{m} & \frac{b}{m} & -\frac{k+k_{k1}+k_{k2}}{m} & -\frac{b}{m} & \frac{k_{k2}}{m} \\ 0 & 0 & \frac{k_{k2}}{b_k} & 0 & -\frac{k_{k2}}{b_k} \end{pmatrix} \begin{pmatrix} x_b \\ \dot{x}_b \\ x \\ \dot{x} \\ x_k \end{pmatrix} + \begin{pmatrix} 0 \\ -\frac{1}{M} \\ 0 \\ \frac{1}{m} \\ 0 \end{pmatrix} f_{coil}$$

$$\begin{pmatrix} x \\ x_b \\ x_{lvd} \\ f_{meas} \end{pmatrix} = \begin{pmatrix} 0 & 0 & 1 & 0 & 0 \\ 1 & 0 & 0 & 0 & 0 \\ -1 & 0 & 1 & 0 & 0 \\ 0 & 0 & k_{k1} + k_{k2} & 0 & -k_{k2} \end{pmatrix} \begin{pmatrix} x_b \\ \dot{x}_b \\ x \\ \dot{x} \\ x_k \end{pmatrix} \quad (4.15)$$

In addition, as is shown in the  $X_{meas}/F_{meas}$  plots of figure 4-4, at low frequency, the calculated compliance is slightly higher than the model compliance. While not as large as at arm resonance, there is still a small unmeasured motion of the base, which makes the apparent stiffness of the material slightly smaller than would normally be calculated. However, if the stiffness of the base is much larger than that of the tissue being measured, this difference is very small. As solid organs will be tested, rather than bone or cartilage, this approximation is reasonable.

While the experiments performed with the TeMPeST 1-D will be discussed in chapter 6, figure 4-5 presents an example of the contrast between tissue measurements made with the TeMPeST 1-D clamped in place (equivalent to figure 4-2), and the same measurement made with the TeMPeST 1-D attached to the arm, which is free to resonate. As was shown above, the gross characteristics of the tissue (a mechanical spring array, discussed in section 6.1) are preserved in the resonating arm case, with only a local error introduced around the arm's resonant frequency.

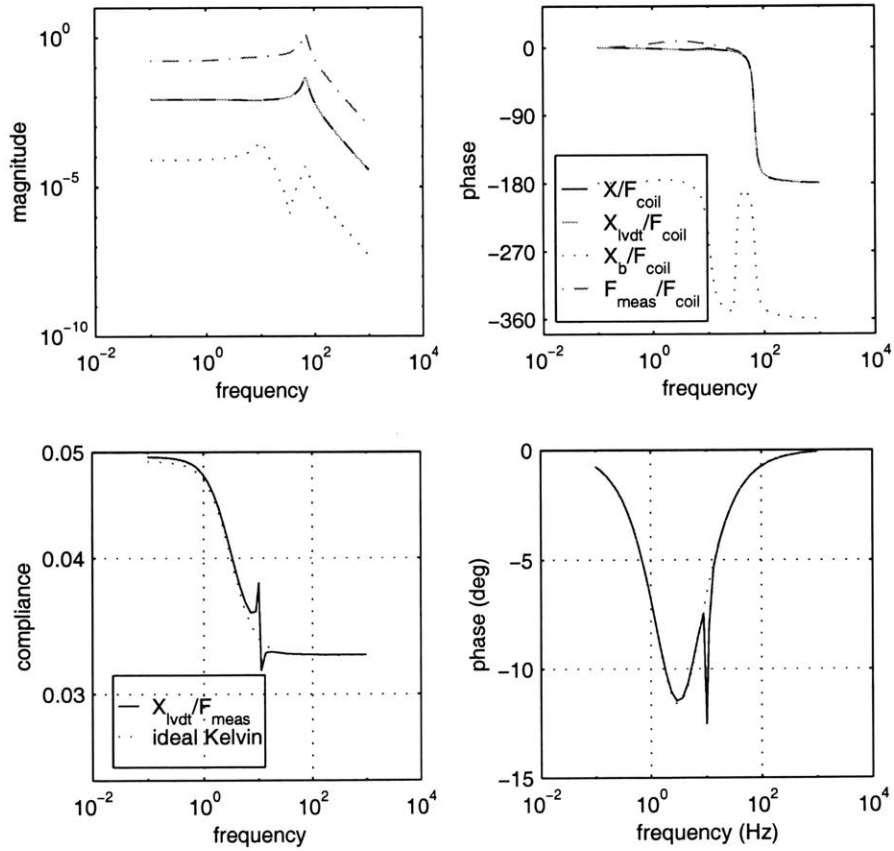
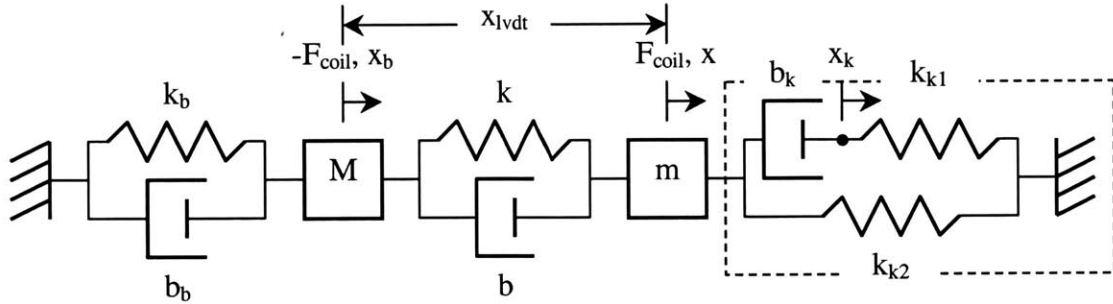


Figure 4-4: Full TeMPeST 1-D in contact with Kelvin body (top); magnitude and phase of measured force, position and base motion (middle); magnitude and phase of  $X_{lvd}/F_{meas}$  and ideal Kelvin response (bottom).

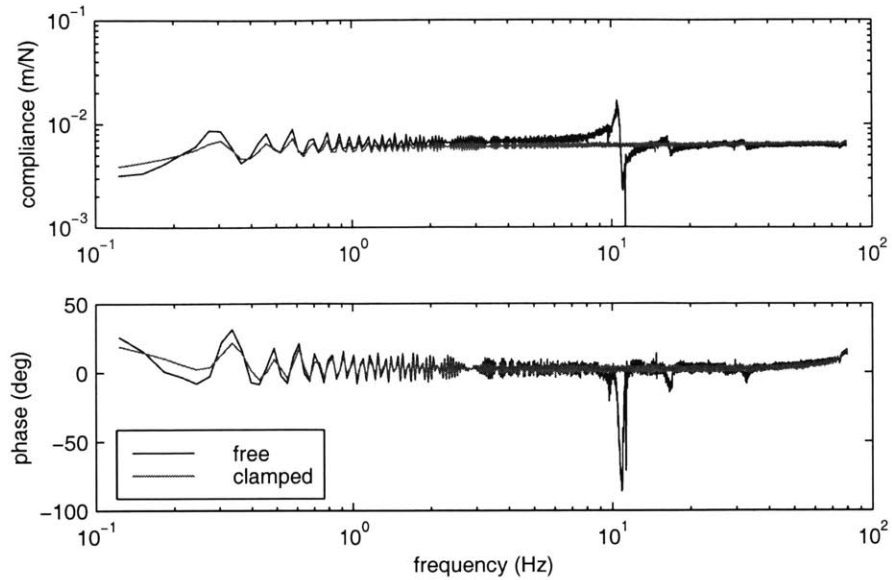


Figure 4-5: Measurements of compliance of mechanical springs made with TeMPeST 1-D fixed in vice and mounted on Mediflex arm

## 4.2 TeMPeST 1-D Characterization

In the preceding sections, models for the system, a method to determine non-parametric, graphical representations of the tissue response and equations to find the parameters for assumed Kelvin behavior have been presented. It remains to fill in the true values for the prototype device, as well as to determine the calibration constants for the sensors and actuator. These measurements will be presented in the following sections.

### 4.2.1 Warm-up characteristics

Before making any measurements with the TeMPeST 1-D, it is important that all of the electronic components have warmed-up to their normal operating temperatures. This true especially for the LVDT and the force sensor, since determination of tissue properties depends on accurate measurement of position and force, but is fairly independent of the precise trajectory followed by the actuator.

Figure 4-6 shows plots of force and position sensor voltage output (or more precisely, output of the instrumentation amplifier and the LVDT signal conditioning hardware) versus time after applying power. From this plot, the force sensor appears



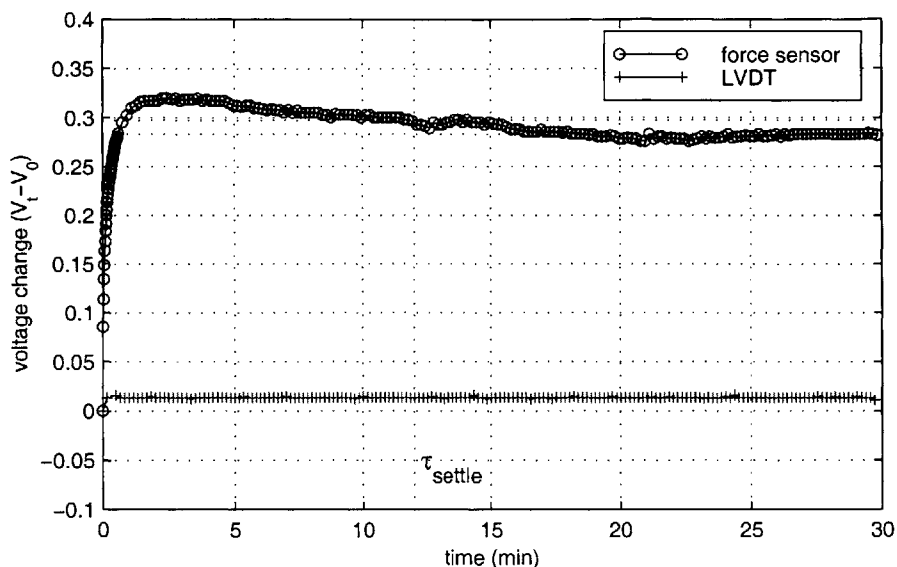


Figure 4-6: Initial zero-force/zero-displacement warm-up response of position and force sensors. Force sensor 5% settling time is approx. 12 min.

to have a heavily damped second order response with a 5% settling time of approximately 12 minutes, while the position sensor settles almost immediately. The LVDT users manual recommends a 15-minute warm-up period, which is on the same order as the settling time of the force sensor, so this period is recommended to ensure that the TeMPeST 1-D has reached a condition that can be considered steady state.

#### 4.2.2 LVDT calibration

The Schaevitz 099 XS-B LVDT is manufactured to have a linearity of  $\pm 1.0\%$  of the full range maximum. The initial calibration sequence described in the user's manual for the Schaevitz ATA 2001 signal conditioner uses the neutral rest- and full scale positions to set the gain and offset. To verify the calibration constant and linearity, a micrometer-based calibration jig was developed, as shown in figure 4-7. With the system warmed up, measurements of output voltage were taken at 0.002" increments, the results of which are presented in figure 4-8. The calibration constant for position sensing is approximately 10.2V/mm.

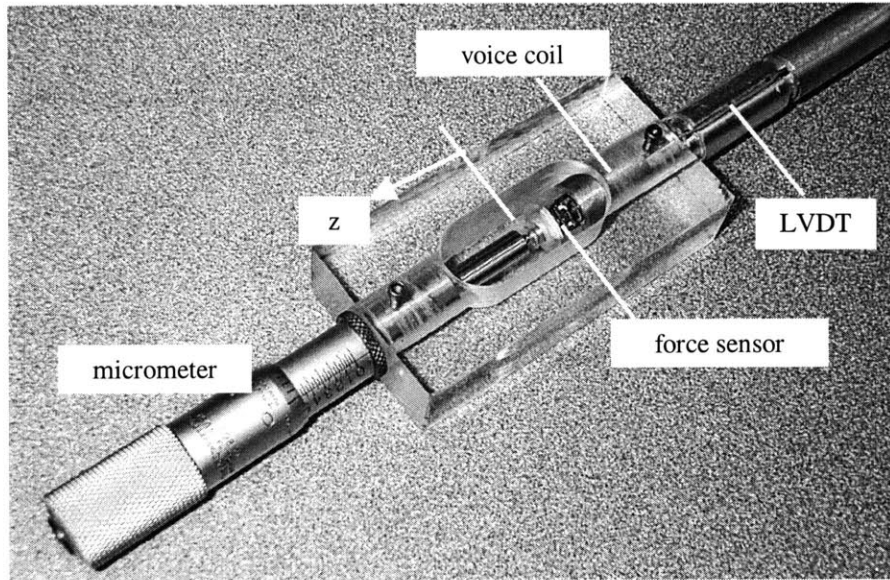


Figure 4-7: Calibration jig for LVDT, as well as testing fixed displacement tests of voice coil and force sensor.

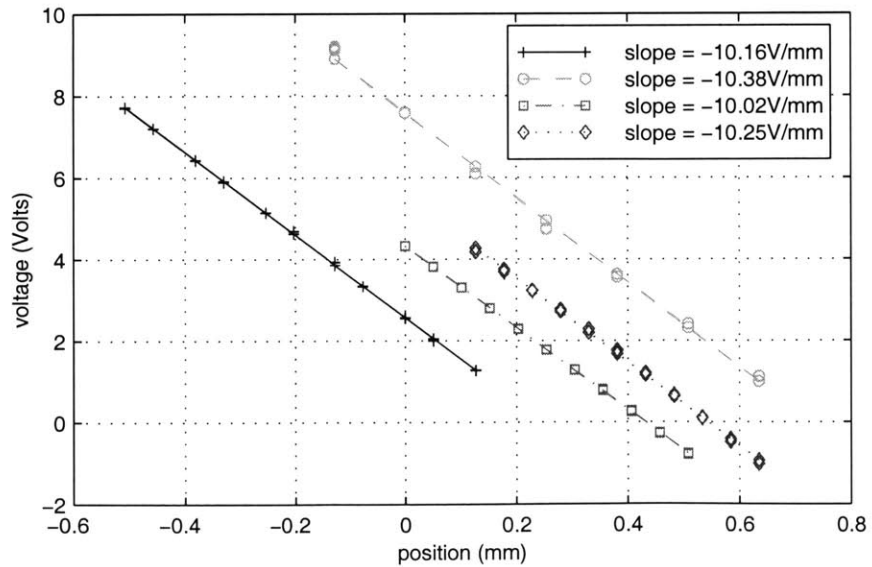


Figure 4-8: Calibration curves for LVDT and position constant. Voltage offset can be adjusted by the signal conditioner, but only slope is needed for frequency domain analysis.  $N=200$  for each position.

### 4.2.3 Force sensor calibration

The nominal response of the force sensor is rated to be  $0.024 \pm 0.004 \text{mV/V/gram}$  (i.e. mV output per volt excitation per gram load), or for the 10V drive used from the instrumentation amplifier chip,  $24.5 \mu\text{V/mN}$ . Since the resolution of the ADC is approximately  $2.5 \text{mV/bit}$ , the sensor output needs to be amplified.

A preliminary version of the circuit was constructed on a protoboard, including the sensor, mounted to the board itself. Standard laboratory masses ranging from 2g to over 50g were loaded onto the indenter tip, and the data acquisition card was used to record the voltage output of the amplifier. Various gains were tried until the amplifier output for the maximum expected load (approximately 0.5N) corresponded with the range of the acquisition card (10V) with some safety margin to permit over load conditions to be detected. A  $40\Omega$  gain resistor yields a gain of approximately 1500.

The fully assembled T1D was calibrated again, with the T1D clamped in a vertical position, and the tip loaded with the masses (figure 4-9). Typical calibration data are shown in figure 4-10. The slope is approximately  $34.5 \text{V/N}$ , and this value was used in the data acquisition and analysis software that will be described in chapter 5. Linearity is approximately  $\pm 1\%$  of the full scale voltage.

### 4.2.4 Voice coil calibration

With the force and position sensors calibrated, they can be used to aid in the calibration of the other components of the TeMPeST 1-D. The first of these is the force output of the voice coil actuator. Since the models presented so far assume that force is the input to the system, rather than current to the voice coil, the force-current constant (and its linearity) need to be found.

Coil calibration was accomplished using the same jig as was used in LVDT calibration (figure 4-7). With the TeMPeST 1-D clamped in the jig, the micrometer was adjusted to set the position of the actuator, and then current was increased and decreased in a linear ramp. Commanded current and force measured by the force

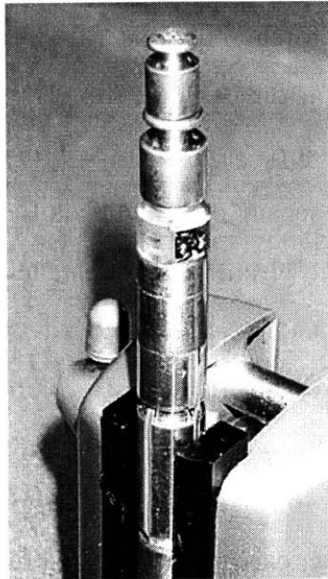


Figure 4-9: Force sensor final calibration method: standard masses loaded on tip of inverted TeMPeST 1-D.

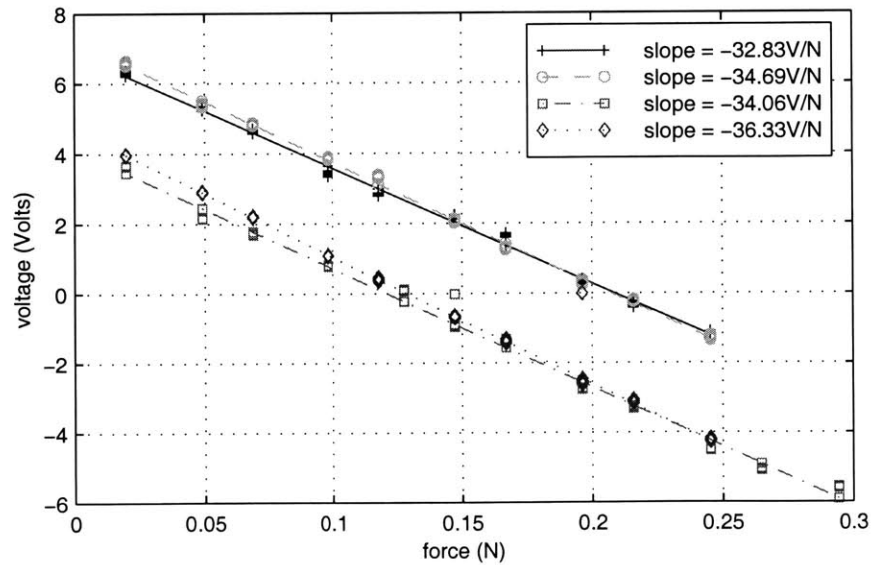


Figure 4-10: Force sensor calibration data. Voltage offset can be adjusted with the bridge balance circuit, but only slope is needed for frequency domain analysis.  $N=200$  for each force value.

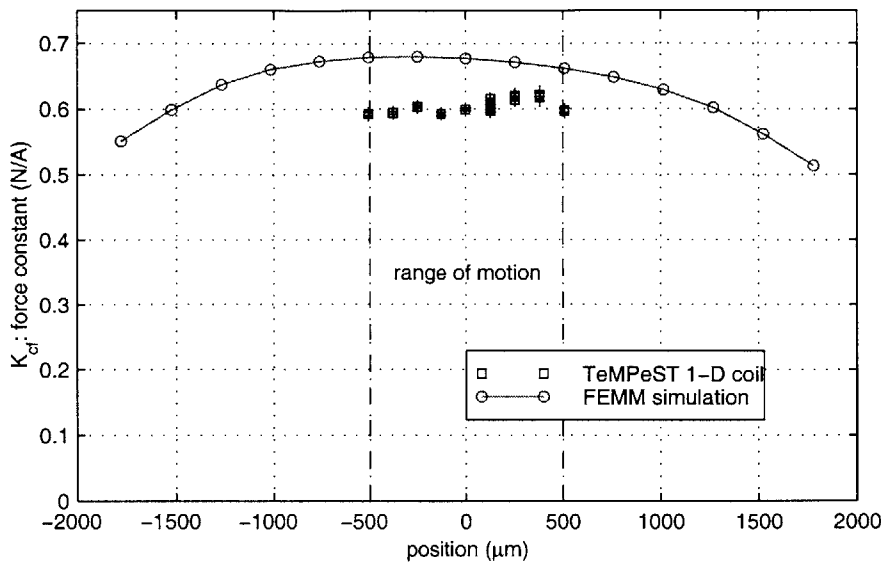


Figure 4-11: Force constant vs. axial position for voice coil. This is equivalent to the torque constant for a motor.

sensor were recorded. This was repeated at a number of positions within the range of motion of the actuator. For positions where the micrometer does not compress the actuator (i.e.  $z > 0$  in figure 4-7), a DC current was applied before the ramps to offset the position of the tip.

Figure 4-11 shows the current-force constant at each position within the range of motion of the TeMPeST 1-D, and shows a mean value of the force constant of 0.61N/A. It also demonstrates that the prediction of constancy of the current-force relationship from the magnetic finite element model is valid, and that the predicted value is close to that of the real device.

#### 4.2.5 Position sensor frequency response

The ATA 2001 signal conditioner for the LVDT uses a 10kHz excitation frequency, and the users manual reports that the output drops by 3dB at 1kHz. Since the TeMPeST 1-D is intended for use at frequencies no higher than a few hundred Hertz, the dynamics of the position sensor are not expected to have any influence on the measured position. However, since the STG motion controller samples the force and

position signals sequentially, the lag between force and position measurement can introduce additional phase lag between the two signals. To verify the magnitude response of the position sensor, and investigate the phase effects, the TeMPeST 1-D was tested with a vibratory stimulator in the MIT Laboratory for Human and Machine Haptics (or Touch Lab).

The Touch Lab stimulator (TLS) uses a galvanometer actuator to drive a small indenter, which is used to investigate the mechanical response of the human fingerpad. With the gain on the position controller (and thus the stiffness of the actuator) turned down, and the TeMPeST 1-D indenter driving the motion of the Touch Lab stimulator indenter, the position response to chirp waveforms was measured by both instruments. The TLS analog output was measured with the channel normally allocated to the force sensor, to make any lag between the force and position measurement apparent in the phase between the two position measuring instruments.

The Bode plots of the transfer function between the two position signals is shown in figure 4-12. Assuming that a pure transport lag between the two signals describes the transfer function, the best fit model, described by equation 4.16 is overlaid on the data.

$$\frac{X_{t1d}(s)}{X_{t1s}(s)} = e^{3.27E-4s} \quad (4.16)$$

From these results, it can be seen that the position response is constant over the range of frequencies covered by the TeMPeST 1-D, and that the lag between the two analog readings is approximately 0.33ms. Knowledge of the transfer function of the position sensor can be used to correct measurements made on unknown materials later on.

#### 4.2.6 Force sensor frequency response

The INA125 instrumentation amplifier documentation indicates that as gain is increased, the break frequency falls from the 100kHz range (G=4), to the 100Hz range (G>1000). Since these are nominal values, a test was performed to determine the

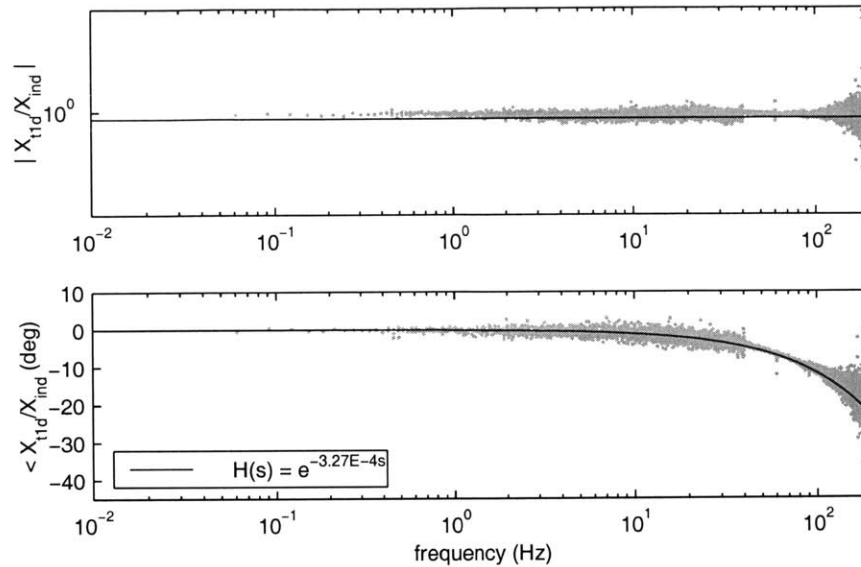


Figure 4-12: LVDT frequency response. Flat response to 500Hz, gain and phase response consistent with transport lag due to sequential analog measurements

true performance of the force sensor and amplifier. The test involved applying force over a range of frequencies with the voice coil with the tip of the indenter held fixed. In this way, the measured force should be the same as the force applied by the voice coil.

In conducting such a test, the voice coil force amplitude would need to remain constant over the frequency range of consideration. This depends on the performance of the analog current source (the OPA2544 power op-amp in particular) at high frequencies. For closed loop operation, the break frequency depends on the gain, according to the limits imposed by the gain-bandwidth product. For the OPA2544, the product is 1.4MHz, and the gain in the feedback loop is 1/40, so the op-amp closed loop bandwidth should be 56MHz. While the series sense resistor and voice coil form an LR filter, since current is being controlled directly, the LR load should not affect the bandwidth of the source-load system. For this reason, it can be expected that this test determines the bandwidth of the force sensor/amplifier without distortion from the actuator.

Figure 4-13 shows the magnitude plot for the transfer function between com-

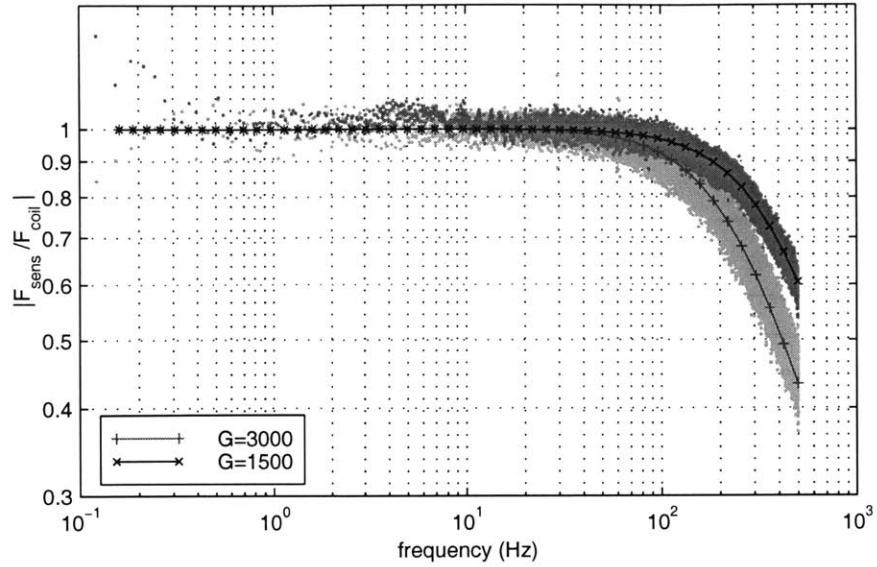


Figure 4-13: Force sensor frequency response (magnitude).

manded and output force. Shown are the data for the INA125 with a gain of 1500 and 3000, with the drop in bandwidth clearly visible. Also shown are the magnitudes of first order continuous systems with unity DC gain and a break frequencies of 380Hz and 240Hz, which closely approximate the behavior of the force sensor/amplifier system with the two gains, respectively. As a compromise between sensor bandwidth and amplifier gain (which improves the signal to quantization noise ratio), a gain of 1500 was used.

By combining the transport lag data from the LVDT dynamic calibration with the first order response of the force sensor, an expression for the filtering effects of the TeMPeST 1-D can be determined (equation 4.17). The inverse of this filter can be applied to the force-displacement response of materials tested with the TeMPeST 1-D, to determine more accurate descriptions of their true responses.

$$H(s) = \frac{e^{-3.27E-4s}}{2\pi 380s + 1} \quad (4.17)$$



### 4.2.7 Flexure stiffness; actuator effective damping and mass

As was described in the second order model earlier, the actuator can be modeled as a three parameter system, with stiffness, a damping element and a mass. These parameters can be extracted from the free motion frequency response as follows.

The combined stiffness of the two flexures (and the force sensor/voice coil wires) can be determined in two ways. The first uses the LVDT calibration jig micrometer to push against the tip of the indenter, while recording the force sensor output. The alternate approach is to pass current through the voice coil, using the known current-force constant to calculate force, and record the position response with the LVDT. If a series of sinusoids of different frequencies, or a chirp signal covering a range of frequencies is used to drive the voice coil, the resonant frequency, and therefore the effective mass, of the actuator can also be determined.

Figure 4-14 shows data points for the static and quasi-static compliance of the flexure. The quasi-static data are taken in two forms: the slope of the least-squares fit of the force-displacement data; and also as the ratio of the FFT magnitudes of the force and position at 0.05Hz<sup>1</sup>. As shown in the figure, they overlay each other precisely. Taking the ratio of the FFTs also yields a phase value for the quasi-static case, showing that there is no lag between force and displacement. The low frequency asymptote of the chirp response also corresponds with the static and quasi-static data. From these results, the equivalent stiffness of the flexures is found to be 276N/m.

The damping ratio (and damping coefficient,  $b$ ) due to air motion within the actuator, material damping, and friction between the moving and stationary parts can be determined from the ratio between the resonant and static compliance ( $M_p$ ) by using equation 4.18 (and 4.20). It can also be determined by performing a best fit on the phase lag to that of an ideal second order system with damping as an unknown parameter. The resonant and static compliances and damped natural frequency are shown in figure 4-14.

---

<sup>1</sup>well below the dominant system resonances.

$$\begin{aligned}
M_p &= \left(2\zeta\sqrt{1-\zeta^2}\right)^{-1} \\
\Rightarrow \zeta &= \left(\frac{1}{2} - \sqrt{1 - \frac{1}{M_p^2}}\right)^{\frac{1}{2}} \\
&= 0.14
\end{aligned} \tag{4.18}$$

With a value for  $\zeta$ , the effective mass can be found using the damped natural frequency,  $\omega_d$  (see equation 4.19). Using a chirp signal on the (rigidly clamped) TeMPeST 1-D, the damped natural frequency was found to be 65.8Hz, yielding an equivalent mass of 1.6 grams. This value is on the same order as an estimate based on the designs for the individual components of approximately 1.2g. This estimate, however, did not include the effective mass of the moving part of the flexures, small amounts of epoxy used to bond parts together, and short lengths of copper wire connecting the moving force sensor and voice coil to the fixed housing.

$$\begin{aligned}
\omega_n &= \sqrt{\frac{k}{m}} = \frac{\omega_d}{\sqrt{1-2\zeta^2}} \\
\Rightarrow m &= \frac{k(1-2\zeta^2)}{\omega_d^2} \\
&= 1.6\text{g}
\end{aligned} \tag{4.19}$$

Comparing the denominators of the transfer functions of a normalized form of equation 4.1 and a unity gain second order system permits calculation of the damping coefficient (equation 4.20):

$$\begin{aligned}
s^2 + \frac{b}{m}s + \frac{k}{m} &= s^2 + 2\zeta\omega_n s + \omega_n^2 \\
\Rightarrow b &= 2m\zeta\omega_n \\
&= 0.20Ns/m
\end{aligned} \tag{4.20}$$

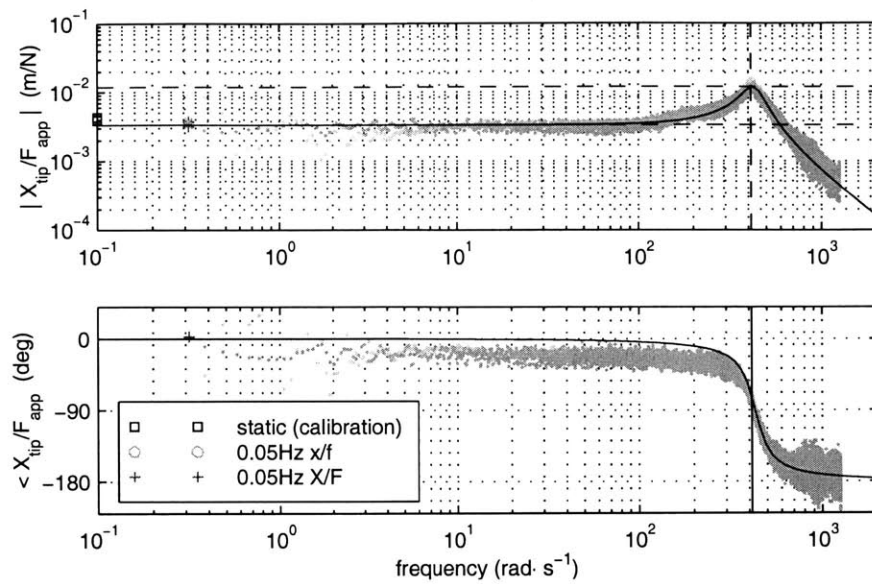


Figure 4-14: Static, quasi-static and dynamic force-displacement response for the indenter. Ideal second order response overlaid over data.

Figure 4-14 shows the frequency response of an ideal second order system with these parameters overlaid on the non-parametric transfer function determined from the ratio of the position and force FFTs.



# Chapter 5

## GUI and controller development

A graphical user interface (figure 5-1), developed using MATLAB, v5.0 and the GUI Design Environment (GUIDE), provides a convenient interface to generate open-loop current trajectories for the TeMPeST 1-D and perform post-processing. Real-time control of the TeMPeST 1-D, including commanding voice coil current and performing data acquisition from the force sensor and LVDT, is performed by a console application written in C++ with Microsoft Visual C++ v5.0. Detailed descriptions of the function of these elements follow.

### 5.1 T1Dgui: graphical user interface for the TeMPeST 1-D

Since the physical input for the TeMPeST 1-D is the current driven in the voice coil actuator, a means for generating the current trajectory is required. Similarly, after position and force data are acquired, some basic post-processing is desired to ensure that no errors or failures occurred during acquisition, and to provide guidance as to which additional experiments should be performed (e.g. different range of frequencies, different amplitudes). The MATLAB-based graphical user interface shown in figure 5-1 provides all of this functionality.

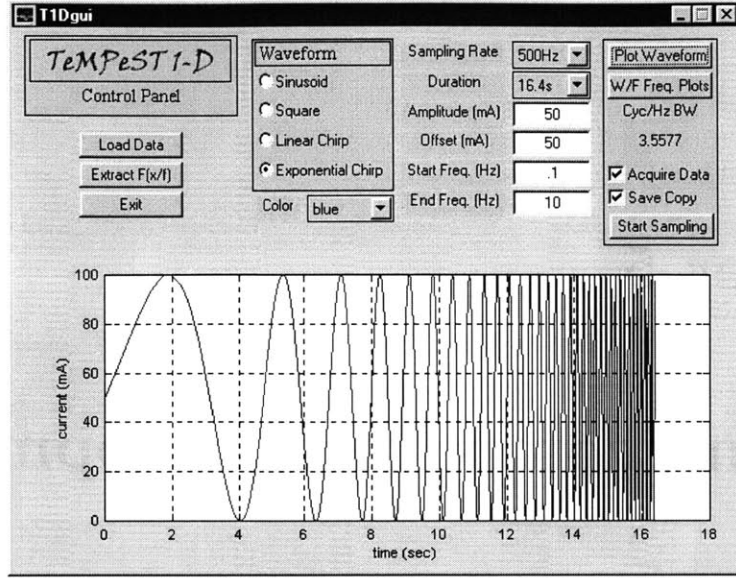


Figure 5-1: Control panel for graphical user interface. Includes controls for waveform type, sampling rate and duration, waveform amplitude, offset and frequency or frequency range.

### 5.1.1 Waveform type selection

T1Dgui allows the generation of four different waveforms (and can be easily extended if necessary): sine, square, and two chirp waveforms (figure 5-2).

The sine wave permits the testing of tissue response at specific frequencies, or over a range of frequencies by examining them one at a time. The square wave allows time domain analysis by providing input for step response examination. The chirp signals allow examination of response over a range of frequencies in a short time interval, necessary for performing the *in vivo* tests that will be described in chapter 6.

$$\text{sine } I(t) = I_0 + I_1 \sin(2\pi f_0 t) \quad (5.1)$$

$$\text{square } I(t) = I_0 + I_1 \text{sgn}(\sin(2\pi f_0 t)) \quad (5.2)$$

$$\text{linear chirp } I(t) = I_0 + I_1 \sin\left(\frac{\pi(f_0 + \Delta f)t}{\Delta t}\right) \quad (5.3)$$

$$\Delta t = t_1 - t_0$$

$$\Delta f = f_1 - f_0$$

$$\text{exponential chirp } I(t) = I_0 + I_1 \sin(C_1(e^{C_2 t} - 1)) \quad (5.4)$$

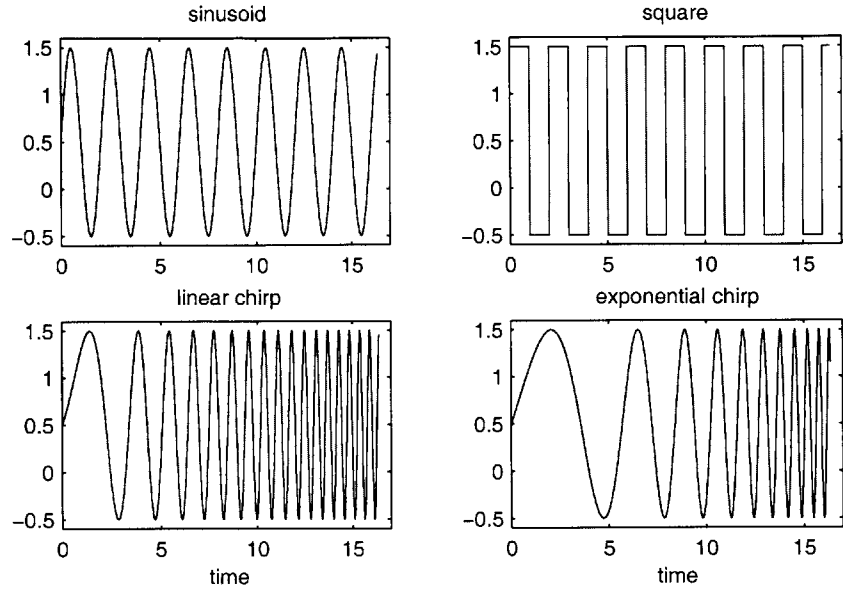


Figure 5-2: Types of waveforms supported by the T1Dgui

$$C_1 = \frac{2\pi f_0 \Delta t}{\ln(f_1/f_0)}$$

$$C_2 = \frac{\ln(f_1/f_0)}{\Delta t}$$

The equations for sine and square waveforms (equations 5.1 and 5.2) are familiar. Chirp signals are essentially sinusoidal signals, but have instantaneous frequencies which vary with time. A commonly used chirp is one where the frequency varies linearly with time (equation 5.3), either increasing or decreasing at a constant rate. Changes in the relative contribution of low or high frequency components can be achieved by altering the way that instantaneous frequency changes. An example of this is a chirp with frequency which changes exponentially with time (equation 5.4). This difference is shown in (figure 5-3), which compares the magnitudes of the fast Fourier transforms of chirp signals with the same starting and end frequency (1.0 to 100Hz), and unity amplitude. Two signals were  $2^{15}$  samples long, with a 2kHz sampling rate, while the other two were  $2^{13}$  samples long.

From the FFTs of the chirp signals, it is immediately seen that the low frequency content of the exponential chirps is greater than that for the linear chirps. The time domain corollary of this is that while the linear chirp has few complete oscillations

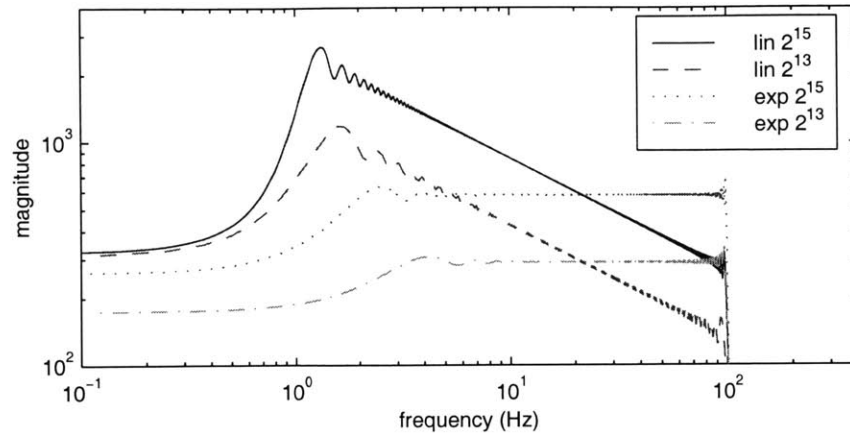


Figure 5-3: FFTs of linear and exponential chirp signals. All signals defined with 1Hz and 100Hz initial and final frequencies

per unit bandwidth at low frequencies, and many oscillations per unit bandwidth at high frequencies, the number of oscillations per unit bandwidth for the exponential chirp is constant; there are as many oscillations as the signal shifts from 1 to 5Hz (for example) as there are between 101 and 105Hz. This permits acquisition of data with a higher signal to noise ratio at low frequencies than the linear chirp.

Chirps are by no means the only kind of signal which has broad-band frequency content. White or pink (i.e. band-limited) random signals could be used to excite the tissue, and the resulting force and position responses analyzed in the same way as the chirp responses.

### 5.1.2 Sampling and waveform parameters

Once the waveform type has been chosen, the control panel is used to set various parameters related to the trajectory to be generated.

The first two fields permit the user to select the **Sampling Rate** and **Duration** of the tests. The ServoToGo motion controller card can run at a sampling rate of up to 2kHz, though lower sampling rates are available (the setting in figure 5-1 is 500Hz, for example). The duration list options correspond with  $2^n$  samples at the given sampling rate. Typically,  $2^{15}$  samples were chosen at a rate of 2kHz, for a total sampling time of approximately 16.4s This time period is convenient both from the



standpoint of performing FFT analysis (i.e. number of samples must be a multiple of 2), and also from an experimental standpoint; as will be described in section 6.4.3, large organ motions due to breathing can be safely suspended for periods of roughly 20 seconds. Together, the period required to make contact with an organ and a 16 second sampling window make full use of the safe “breathhold” period.

**Amplitude** is self-explanatory, and **Offset** is the DC current which is added to the trajectory to ensure that a preload is applied to the tissue. For sinusoidal and square wave trajectories, the **Start Freq.** field is disabled, while the **End Freq.** field is used to generate the waveform. For chirps, the start and end frequencies define the range spanned by the trajectories. The end frequency need not be greater than the starting value; chirps with decreasing frequency can also be generated if desired.

The **Color** list menu is a feature which determines the appearance of the post-processing output plots. It is useful when comparing multiple data sets, so that the results can be distinguished by color.

### 5.1.3 Function buttons

**Plot waveforms** extracts the user-defined settings then generates and plots the desired trajectory in the plot window. A number of informational plots are generated by **W/F Freq. Plots**, which generates plots of instantaneous frequency versus time, the trajectory plotted against instantaneous frequency, and Bode plots for the trajectory.

**Load data** permits the user to recall archived data for off-line analysis. It opens a separate window which summarizes the details of all stored data and allows basic manipulation of the files. Once a data set has been recalled, the current trajectory which was used to generate it is reconstructed and displayed to the user.

**Start Sampling** performs slightly different functions depending on the settings of the checkboxes above it. With both the **Acquire Data** and **Save Copy** boxes checked, this button calls a function which saves the trajectory to an ASCII file, together with the parameters used to generate the trajectory. It then calls the real-time control program (see section 5.2) which drives the TeMPeST 1-D and records the data. When complete, copies of the data files are saved to an archive (which is

accessed by the **Load Data** function), and post-processing commences.

Plots are shown of the unprocessed position and force offset voltage signals (measured before and after running the desired oscillation), followed by the unprocessed position and force voltage responses. Some basic error correction is performed on the signal<sup>1</sup> and the user is given the option to filter the data. In the current implementation, a simple first-order, low-pass digital filter is used with a break frequency 10 times higher than the instantaneous frequency, to remove high-frequency noise from the force and position response. Since the filter is applied to both signals, when the ratio of the force and position FFTs is taken, the contribution of the filter cancels out, as it exists in both the numerator and denominator of the equivalent transfer function.

After error correction and optional filtering, the position and force are presented in the time domain, converted from voltage to micrometers and millinewtons, respectively. FFTs of both are displayed, as is a plot of the magnitude and phase of the measured compliance. Appendix D show a typical sequence of the output plots.

Since the FFTs include magnitude data for frequency data outside of the range where they have any significance, **Extract F(x/f)** is used to extract values only in the range covered by the start and end frequencies. This is convenient for saving more compact data sets and further post-processing.

With the **Acquire data** checkbox off, **Start sampling** does not call the real-time code, analyzing instead whatever data file is in the working directory (which may have been copied from the archives by using the **Load Data** function). This is

---

<sup>1</sup>The multiplexer, which precedes the ADC on the STG motion controller card, occasionally reads the same channel twice in a given cycle, so similar voltages are measured for both force and position. In addition, the Windows operating system overhead sometimes takes priority over the “real-time” acquisition program, causing some measurements to be skipped. In the former case, the data is checked and flagged when nearly coincident values are found. Linear interpolation is performed using values preceding and following the flagged data points to replace them. This is typically sufficient to correct the data, since two or more close values rarely occur consecutively. The skipped readings are also filled in by linear interpolation. With a high sampling rate compared to the instantaneous frequency of the signal, the errors introduced by linear interpolation are small, and significantly better than the errors generated by mis-reads. In certain cases the errors cannot be corrected in this automatic manner, so a separate GUI was written to permit manual correction of data.

typically used for off-line processing of data.

When the **Save Copy** checkbox is off, no copy of the working data is archived.

## 5.2 T1D.exe: real-time control and data acquisition for the TeMPeST 1-D

This program is called by the T1Dgui. It calls the DAC to send a voltage signal to the current source, and reads the voltage outputs of the LVDT signal conditioner and the force sensor instrumentation amplifier.

The program accesses the ASCII trajectory file generated by the **Start Sampling** function of T1Dgui, and loads it into a dynamically allocated array. At the same time, memory is allocated to accommodate the force and position signals which will be measured.

It then prompts the user to position the TeMPeST 1-D in free space so that the force and position sensor offset voltages can be measured. One second of data is read and saved to a file in ASCII format with timestamp, force and position readings.

Since the current trajectory oscillations all start at zero plus the pre-load offset, the first value in the trajectory, representing only the pre-load, is sent to the current source. This drives the voice coil to some non-zero position. The position is displayed to the user via a simple ASCII cursor. The user brings the TeMPeST 1-D into contact with the tissue using the fine positioning cam (see section 3.6.5). As the indenter makes contact, the actuator is pushed back towards the neutral position, as shown to the user via the ASCII cursor. Once the cursor has returned to the zero position, the actuator is also at the neutral position, so the preload determined by the trajectory is the same as that being exerted by the actuator (i.e. the flexures are at their neutral position and do not contribute to or subtract from the commanded force). With the actuator at neutral, the user starts the real-time control and acquisition part of the code.

By observing an onboard clock, which increments once every sampling period, the

program can regularly measure the force and position signals and update the DAC value to the next point in the trajectory. A hardware interrupt can be generated with the motion controller card, but the available drivers do not provide direct access to this information. The “clock-watching” system performs the same job as an interrupt handler would, but occupies the majority of the system resources while T1D.exe is running. However, since no other operations need to be performed during sampling, this is a satisfactory solution.

When the trajectory has been completed, the DAC is set to zero so that the current source commands zero current, and the arrays in which the force and position data have been stored are written to a text file. A second set of sensor voltage offset data is taken and saved, and control is returned to T1Dgui.

The motion of the actuator is controlled in open loop for simplicity; since the applied force and displacement are measured directly, following any trajectory with frequency components in the range of interest is sufficient for data extraction. As will be shown in the chapter 6, in some cases it would be convenient to perform closed loop control on position or force. For example, as a chirp signal approaches the actuator resonant frequency, oscillation amplitude increases under open loop control, so the commanded values used in a given test must be small enough over the entire range to avoid driving the actuator into its end stops at resonance. An ideal closed loop system would generate constant amplitude vibrations through the resonant regime, and also be sufficient to recognize the limits of the current amplifier, especially above the resonant frequency of the actuator.

However, as mentioned in section 3.1, since the model of the TeMPeST 1-D in contact with an unknown material is approximately known *a priori* at best, it would be difficult to implement a stable classical controller with desirable characteristics like high bandwidth (or equivalently fast response). A pole-cancellation controller was investigated briefly, but the open loop system was found to be more than satisfactory for the level of analysis performed to date. More advanced control schemes such as adaptive control were not pursued, but could be implemented with further development.

## Chapter 6

# Validation Tests and Tissue Property Measurements

As a proof-of-concept demonstration, the TeMPeST 1-D was used to make *in vivo* measurements on organ tissues to demonstrate that it could be used to acquire material properties in a surgical environment. Prior to these tests, the TeMPeST 1-D was used to measure the responses of compliant, inertial, and viscoelastic media to verify that it performed as expected, and could be relied upon to accurately measure their properties.

The first experiments were performed on a series of mechanical springs whose stiffnesses were independently measured. Spring stiffness should be constant over a range of frequencies, with no phase lag between reaction force and displacement. The measured stiffness should also correspond with that determined by an independent testing method.

The second set of experiments were performed on inertial loads. As with spring elements, pure inertial loads will yield frequency responses of known form: a fall in gain by a factor of 100 per decade of increasing frequency, and a phase lag between position and force of  $180^\circ$ . Known masses are easily available by using standard balance masses.

Pure damping experiments were not performed because the force sensor on the TeMPeST 1-D can only measure compressive loading; during half of a cycle of motion

of a plunger driven through a fluid, the sensor would have to support tensile loading. While this would also apply for inertial loads, the weight of the mass due to gravity can be used as a pre-load to ensure that the net force on the sensor remains compressive.

The third series of validation tests dealt with a set of silicone gel samples, prepared from mixtures of different proportions of two component liquids. By varying the proportions, gels with different stiffnesses could be created, and the differences measured both with standard testing machines and with the TeMPeST 1-D. The silicone gel is a material with visco-elastic properties, so measurements of variation in stiffness and phase angle could be made, and compared between the two measurement techniques.

Finally, four sets of *in vivo* measurements on porcine organ tissues, including liver and spleen, were made. The first, third and fourth sets of measurements were made under laparoscopic conditions, while the second was performed during open surgery. These limited tests should be considered proof-of-concept demonstrations rather than a source for precise values of tissue properties. Future tests, and the conditions necessary to make the results meaningful will be discussed in section 7.2

## 6.1 Testing on Mechanical Springs

One of the simplest mechanical elements is the spring, which has a relationship (and its Laplace transform) between applied force,  $f$  and displacement,  $x$  of the form:

$$f(t) = kx(t) \tag{6.1}$$

$$F(s) = kX(s) \tag{6.2}$$

where  $k$  is a constant of proportionality (spring constant). This expression and the behavior of real springs under normal operating conditions are independent of the kind of motion or force imposed, and so are equally valid for static or dynamic conditions<sup>1</sup>. Because of the simple nature of the relationship, it is a good starting

---

<sup>1</sup>Although at high frequencies, the mass and material damping properties of a real spring may

point for validating the performance of the TeMPeST 1-D as a device for measuring the material properties of compliant objects, and eventually tissues.

### 6.1.1 Spring testing apparatus

A array of mechanical springs was arranged, such that the TeMPeST 1-D indenter tip would deflect one or more springs in parallel, thereby permitting a number of different equivalent spring constants to be measured. As shown in figure 6-1, from one to four springs would be deflected and their reaction forces measured.

The spring arrays were independently measured using the custom-made cartilage press (CP) (figure 6-1) at the Cartilage Biomechanics and Imaging Laboratory at the Harvard Institutes of Medicine. This compression testing system, originally designed to apply loads to cartilage samples, was used to apply sinusoidal displacements at 0.1Hz, with amplitudes of 1.0mm, and either 1.2 or 2.0mm offset in the mean position of oscillation. Figure 6-2 shows the force-displacement data and the best fits. The “hysteresis” loop (small for 0.1Hz, larger for 0.4Hz) is due to a 0.11s sample hold of the force measurement (sampling rate is 4Hz), rather than the response of the spring (which ideally should have no hysteresis). From the 0.1Hz data, however, it is clear that the springs behave linearly.

The TeMPeST 1-D was set up as shown in figure 6-1, rigidly mounted so that any resonant excitation of the body due to any flexibility in the vice would occur at frequencies much higher than those which would be used in testing.<sup>2</sup>

The springs were tested at 0.1Hz to match the conditions used with the CP, and over a range of frequencies with the chirp signals described in section 5.1.1. The low frequency sinusoidal stiffness as well as the ratios of the fast Fourier transforms of the measured force and displacement of the chirp signals are shown in figure 6-3. Also included are the CP measurements of stiffness for comparison. Table 6.1 summarizes the stiffnesses measured by the various methods.

---

begin to alter the relationship.

<sup>2</sup>in contrast with the resonant frequency of the TeMPeST 1-D on the Mediflex arm, which occurs around 10Hz, well inside the test range.

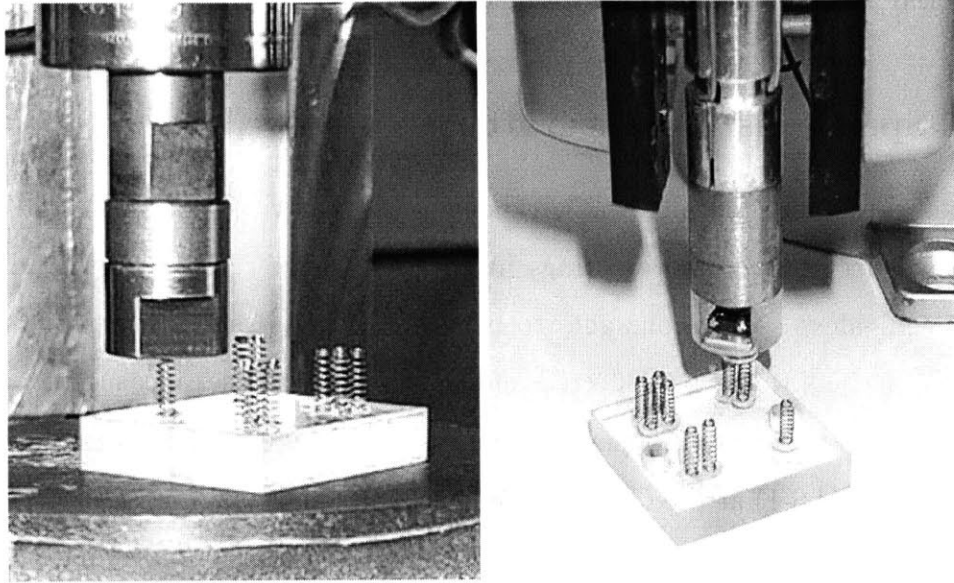


Figure 6-1: Testing of spring array with CBIL cartilage press (left) and TeMPeST 1-D (right)

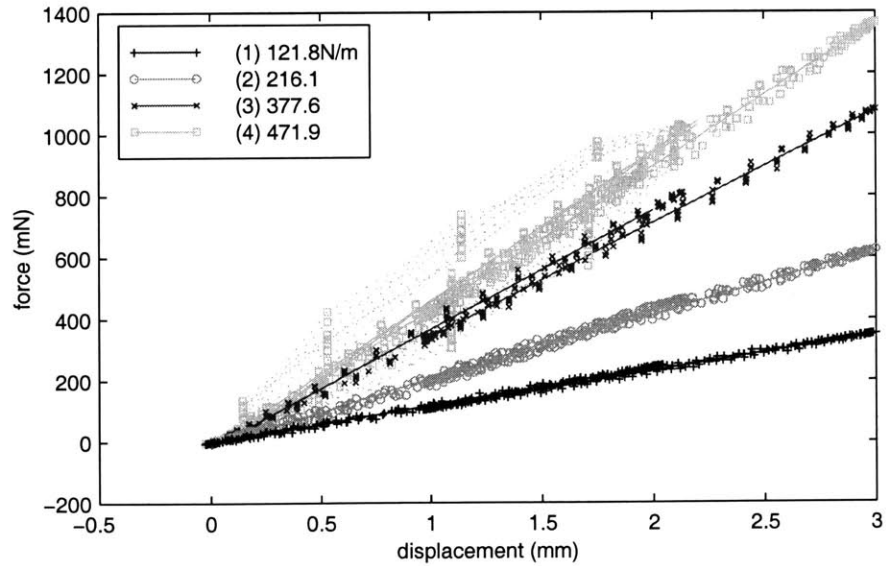


Figure 6-2: Spring testing array force-displacement response using CBIL cartilage press. Hysteretic 4-spring data caused by lags between force and position sensing.



Table 6.1: Measured spring stiffness summary.

# springs	Stiffness $\pm 1\sigma$ (N/m)		
	CP	T1D (0.1Hz)	T1D chirp mean
1	121.8	$120 \pm 8$	$121 \pm 7$
2	216.1	$204 \pm 14$	$196 \pm 9$
3	377.6	$382 \pm 10$	$279 \pm 15$
4	471.9	$419 \pm 32$	$343 \pm 19$

The springs exhibit constant stiffness up to approximately 100Hz, and a no phase difference between measured force and displacement. Above this frequency, additional dynamics at and beyond resonance distort the compliance magnitude and phase, and the time lag between the force and position measurements adds an additional component to the phase difference. As such, for the system in its current form, frequency dependent values above 100Hz are not reliable. Improvements to extend the range and eliminate the time lag problem will be discussed in chapter 7. However, since human motor responses have a bandwidth of  $\mathcal{O}(10\text{Hz})$ , the range covered by the existing device may be sufficient for many purposes.

The 0.1Hz sinusoidal results from the cartilage press and the TeMPeST 1-D agree within one standard deviation for one through three springs. The chirp data for one or two springs are similarly in agreement with 0.1Hz data. However, the sinusoidal data for four springs, and the chirp data for three or four springs undershoot the value determined by the cartilage press. The cause for this disagreement has not been completely determined, but one possible cause is imperfectly matched spring lengths in the three and four spring arrays. If the preload was not sufficient to ensure that all of the springs were being compressed throughout the entire cycle, a lower stiffness would be measured due to loss of contact with one or more springs at the upper limit of motion. Another possibility is some non-linearity in the springs, which had a slight taper at their ends, which might also contribute to erroneous measurements. For the more ideal cases of one or two springs, the results were in good agreement.

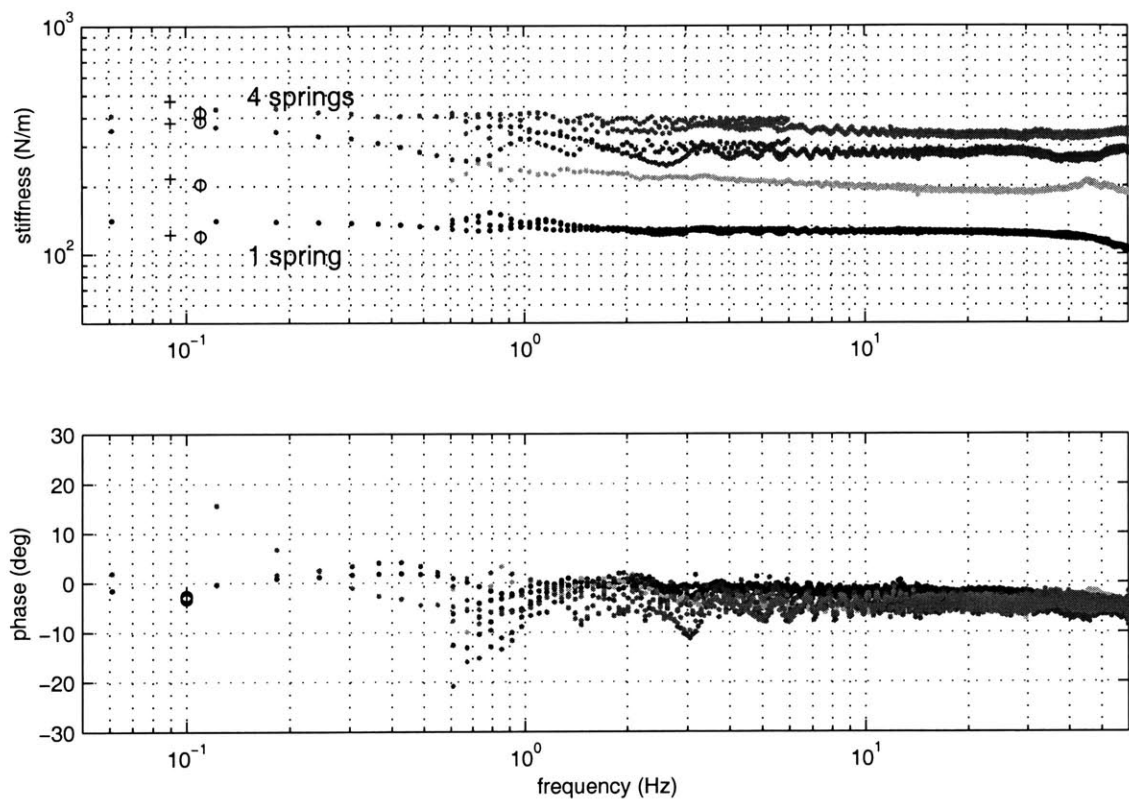


Figure 6-3: Spring array stiffness under 0.1Hz sinusoidal excitation using CBIL cartilage press (CP: +) and TeMPeST 1-D (T1D: o), and chirp excitation with TeMPeST 1-D.

## 6.2 Testing on Inertial Load

As with the springs, inertias have simple forms for the relationship between applied force and position:

$$f(t) = m\ddot{x}(t) \quad (6.3)$$

$$F(s) = ms^2X(s) \quad (6.4)$$

where  $m$  is the mass of the load. Because of the second derivative relating force and position, there is a phase difference of  $180^\circ$  between a sinusoidal applied force and the measured position.

### 6.2.1 Inertial load testing method

The TeMPeST 1-D was inverted and clamped in position. Five and ten gram masses were placed on the indenter tip, and held in place with double-sided adhesive tape to prevent them from sliding off during vibratory testing (figure 6-4). Chirp and pure sinusoidal signals were used to drive the indenter at frequencies from 1 to 400Hz, the results for which are shown in figure 6-5.

As can be seen, at low frequencies, the magnitude of the response falls below the ideal response. This is because at such slow excitation frequencies, the acceleration of the mass, and therefore the applied force, are smaller than detectable by the force sensor. At high frequencies, the amplitude of vibration falls, reducing the signal to quantization noise ratio. This makes the ratio of the force and displacement FFTs noisier at high frequencies.

Since the magnitude of an inertia's frequency response has the form:

$$\left| \frac{X(j\omega)}{F(j\omega)} \right| = \frac{1}{m\omega^2} \quad (6.5)$$

the mass can be calculated at any given frequency from:

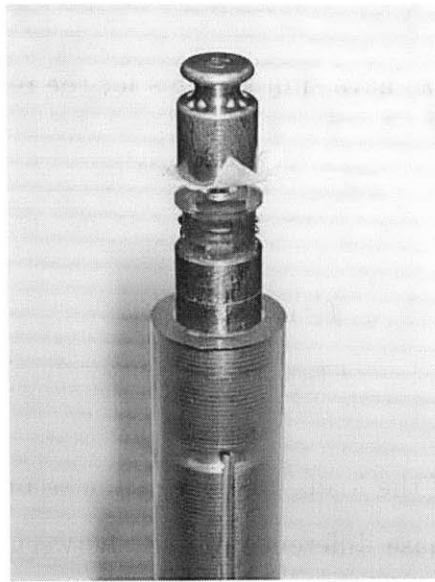


Figure 6-4: Test arrangement for inertial load experiments.

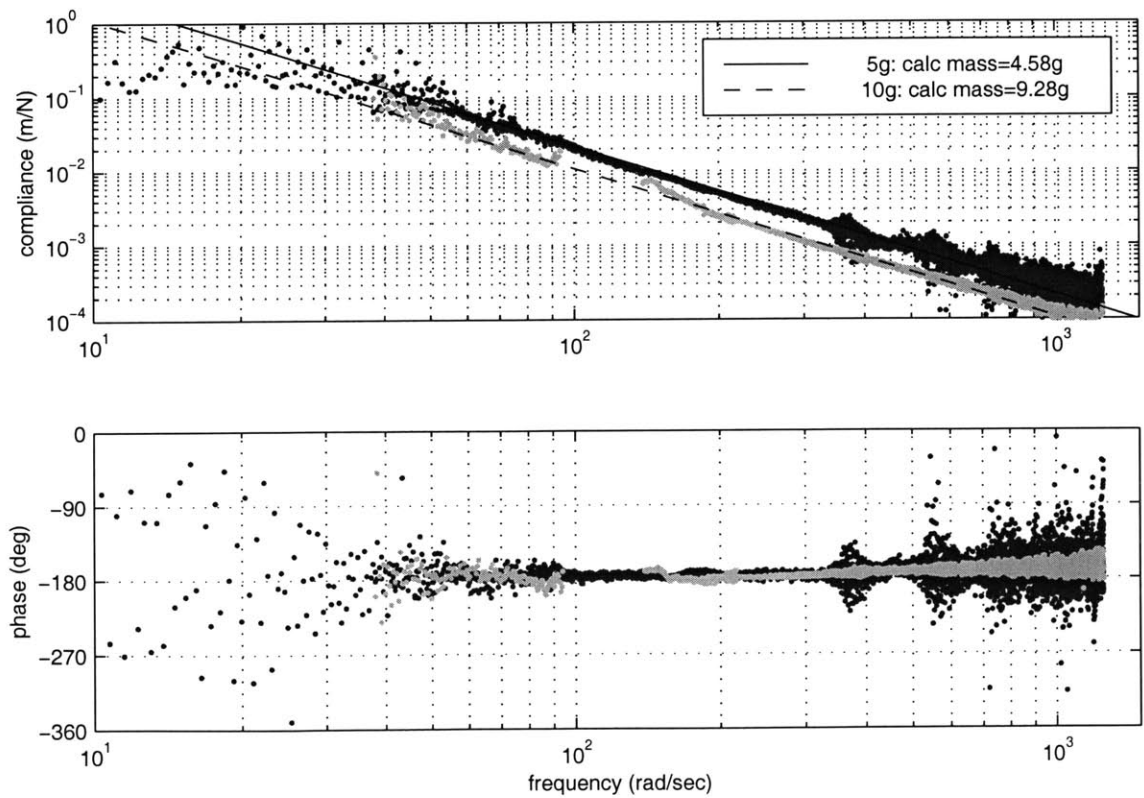


Figure 6-5: Bode plots of response of inertial loads

$$m = \frac{1}{|X(j\omega)/F(j\omega)|\omega^2} \quad (6.6)$$

Fitting a line of slope -2 to the logarithm of the magnitude and frequency, the mass can be read directly as the inverse of the magnitude at one radian per second. This calculation was performed by minimizing the error between the logarithm of the data and a line with -2 slope but unknown intercept at  $\log\omega = 0$ . Table 6.2 summarizes the calculated masses, which are both within 10% of the true values.

Table 6.2: Best fit values for standard masses

True mass	best fit
5g	4.58g
10g	9.28g

### 6.3 Testing on Silicone Gel Samples

A spring-dashpot, such as a shock absorber would have a two parameter ideal model with both compliant and viscous elements. The behavior of such a system is the same as that of a Voigt body, described in section 2.1 (see figure 2-1b). Commercially available products<sup>3</sup>, can be described by such a model, but are not available with both stiffnesses and time constants ( $\tau = b/k$ ) in the range of the TeMPeST 1-D.

As an alternative, and as an example of a material more closely approximating tissue, a silicone gel (GE RTV 6166) was used to make phantoms with different stiffnesses and damping properties. It has been used by other researchers [34] to test devices designed to evaluate the material properties of cancerous tissues. GE RTV 6166 is made of a mixture of two liquid components, parts A and B, which are normally mixed in equal amounts. Mixing them in different proportions yields gels with a range of elastic moduli, over the range expected for living tissue based on the literature.

---

<sup>3</sup>e.g. Airpot Corporation, Norwalk, CT

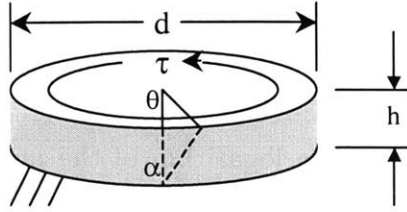


Figure 6-6: Parallel plate shear modulus testing geometry

### 6.3.1 ARES standard testing of gels

To provide a standard measurement of the properties of the gels, thin samples were prepared for testing in a Rheometric Scientific ARES parallel plate rheometer in the MIT Polymer Processing Research Laboratory. Testing with this device involves placing a sample between two circular plates, and rotating one plate relative to the other. This applies a torsional shear loading to the sample, while torque and angular displacement are recorded. Separation between the plates, measured by the rheometer, and the plate diameter fully determine the geometry of the sample (see figure 6-6), and shear modulus,  $G$ , can be found from equation 6.7.

$$\begin{aligned}
 G &= \frac{\tau}{\tan \alpha} \\
 &= \frac{2\tau h}{d\theta}
 \end{aligned}
 \tag{6.7}$$

Four mixtures were prepared, and poured into cylindrical molds, yielding large samples 85mm in diameter and 12.5mm thick, and small samples 30mm in diameter and approximately 2.5mm thick (figure 6-7). The small samples were tested in the rheometer, after being trimmed to the 25mm diameter of the testing plates, except for the 60:40 mixture, which did not solidify completely.

The first test performed on each sample was to determine the range of strain in which the gel has a linear stress-strain relationship. Strain sweeps were performed, in which sinusoidal oscillations with increasing amplitudes were applied to the gel. The shear modulus remained constant at least up to 50% strain for each of the gels tested. The materials were tested at both 1Hz and 50Hz to verify that the linear range did

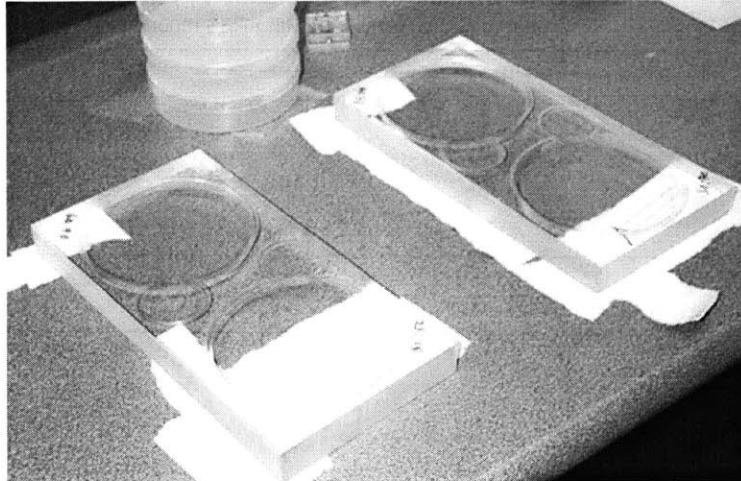


Figure 6-7: RTV silicone solidifying in molds.

not fall below 50% in the range of frequencies of interest.

While all of the samples remained linear at each frequency, the shear modulus was higher at 50Hz, which implies that the gels have a frequency dependent response. This is desirable, because it means that a more complex relationship exists in the frequency range of interest than that of the spring.

After determining a lower bound for the range of linearity, frequency sweeps, with an amplitude of 10% strain and frequency range from 0.01 to 80Hz (the upper limit of the ARES equipment) were performed on the samples to determine the frequency response of the gel. Figure 6-8 shows the frequency responses of the samples, converted from the complex shear modulus output of the ARES system, to shear modulus magnitude/phase plots.

All of the samples exhibit a flat response at low frequency, with phase lag approaching zero. This indicates that the static moduli are likely the same as the value for the minimum frequency tested. Another feature of the behavior is that the harder samples exhibit an increase in stiffness beginning at higher frequencies than the softer samples. The change in phase follows similar trends, with the increase occurring at lower frequencies for the softer samples.

The responses, however, do not correspond with either Kelvin or any of the other models for tissue discussed so far. The changes in stiffness and phase occur over a

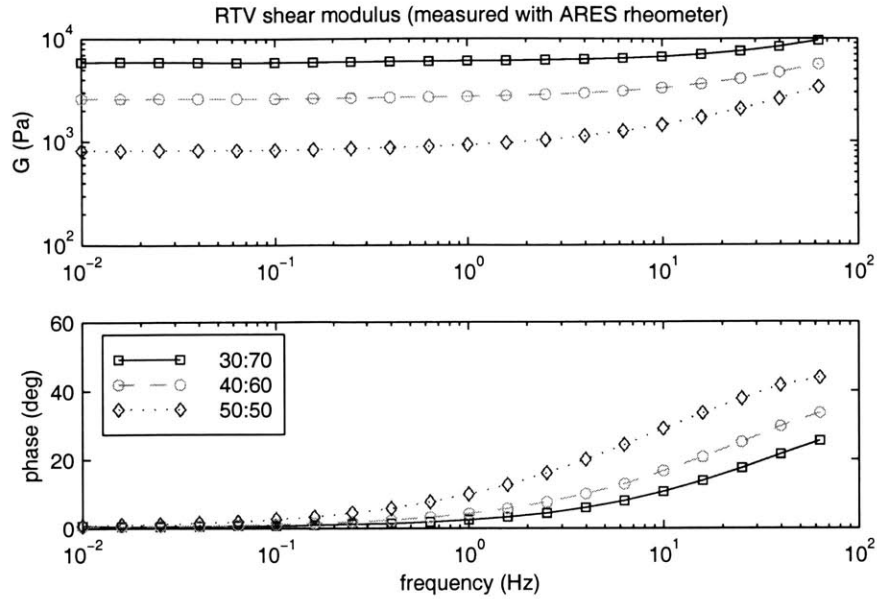


Figure 6-8: Magnitude and phase of shear modulus ( $G$ ) (n.b. modulus is inverse of compliance, hence positive phase)

broader range of frequencies than would be the case for such simple models. Without resorting to more complex models, the gel samples can be approximated as elastic at frequencies below about 10Hz.

The samples were tested first approximately two days after mixing (with a recommended cure time of 24 hours at room temperature), and again at five days, and showed only slight changes in the response. Since both increases and decreases were noted, the changes are more likely due to slight damage to the samples due to handling and imperfect placement of the sample during the second test.<sup>4</sup>

### 6.3.2 Cartilage press standard testing of gels

In addition to the ARES testing, the large gel samples were also tested using the CP, using a 5mm right cylindrical punch (see figure 6-9). The punch was designed to have the same geometry as the tip of the TeMPeST 1-D, to provide an independent test as close to those that would be performed with the instrument as possible. Because the

<sup>4</sup>All of the gels were sticky, the softest gel especially so. Precise re-placement of the samples was impossible, and the softest sample underwent some plastical deformation on removal from the storage container and the parallel plates of the rheometer.



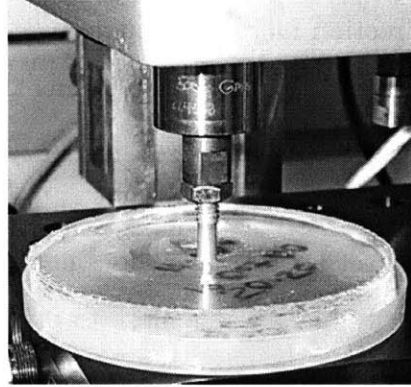


Figure 6-9: CBIL cartilage press being used to test silicone gel sample.

Table 6.3: Cartilage Press quasi-static elasticity data

Gel sample	stiffness (N/m)	Young's modulus (kPa)
30:70	130.9	15.3
40:60	67.1	7.63
50:50	22.0	2.39

Poisson ratio of the gel is unknown<sup>5</sup> the assumption that it has a value of 0.5 could result in errors in converting between shear and Young's modulus.

As with the spring testing (section 6.1), sinusoidal displacements were imposed on the gels at 0.1 and 0.4Hz, with an offset to ensure contact between the punch and the gel. The responses are linear over this range of displacements. This implies that measurements made with the TeMPeST 1-D, which would have smaller amplitudes, will also be linear, and more importantly, that the solutions for linear materials described earlier could be applied to permit extraction of material properties.

Table 6.3 summarizes the stiffnesses of the gels. Because of the time lag between position and force measurements, phase measurements could not be determined from the data.

As discussed in section 2.2, for compliant bodies supported by rigid surfaces, a correction to the semi-infinite body solution can be made to calculate the elastic modulus. For the indenter punch with a radius of 2.5mm, and a thickness of the

---

<sup>5</sup>not reported in the product literature, and might be different for different mixtures.

material of 12.5mm, the correction factor for equation 2.21 rises from 1.24 to 1.42 as indentation depth increases from 1% to 15% [34]. Using this equation, and correction factors for mean indentation equal to the ratio between the mean applied force and the measured spring constant, the elastic modulus values calculated are included in table 6.3. The specification sheet for RTV6166 does not indicate a value for Poisson's ratio; however, rubber typically has a value close to 0.5, so this value is assumed in calculating  $E$ , Young's modulus.

### 6.3.3 TeMPeST 1-D testing of gels

The large gel samples were tested with the TeMPeST 1-D using exponential chirp signals running from 0.04 to 400Hz, with nominal preloads of 90mN for the stiffer gels (40:60 and 30:70) and 45mN for the 50:50 gel. The command amplitudes were 120mN for frequencies away from the resonance, and 60mN around resonance to avoid driving the actuator into the hard end stops. In addition, tests using sinusoidal signals with the same preload and amplitude, at a few fixed frequencies over the range, were performed on the hardest (30:70) gel sample to verify that the chirp signal response corresponded with the fixed frequency sinusoidal response.

As with the spring testing, the TeMPeST 1-D was fixed in a vice to avoid any effects of the resonance of the TeMPeST 1-D on the Mediflex arm. Experiments were also run with the TeMPeST 1-D mounted to the Mediflex arm to verify that no differences in the response appeared at frequencies other than the low frequency resonance.

As mentioned in chapter 2, for indentation there are solutions for both friction-free (equation 2.17) and no-slip (2.18) assumptions, which yield different results for the same measured force-displacement response. Since the friction-free expression is less sensitive to the estimated value of the Poisson ratio, a drop of light instrument oil was placed between the indenter tip and the gel sample to approach this condition. Without the oil, the 30:70 gel is somewhat sticky, and the 50:50 gel extremely so, and would much more closely be described by the no-slip expression.

Figure 6-10 shows the Bode plots for the three gel samples, together with the

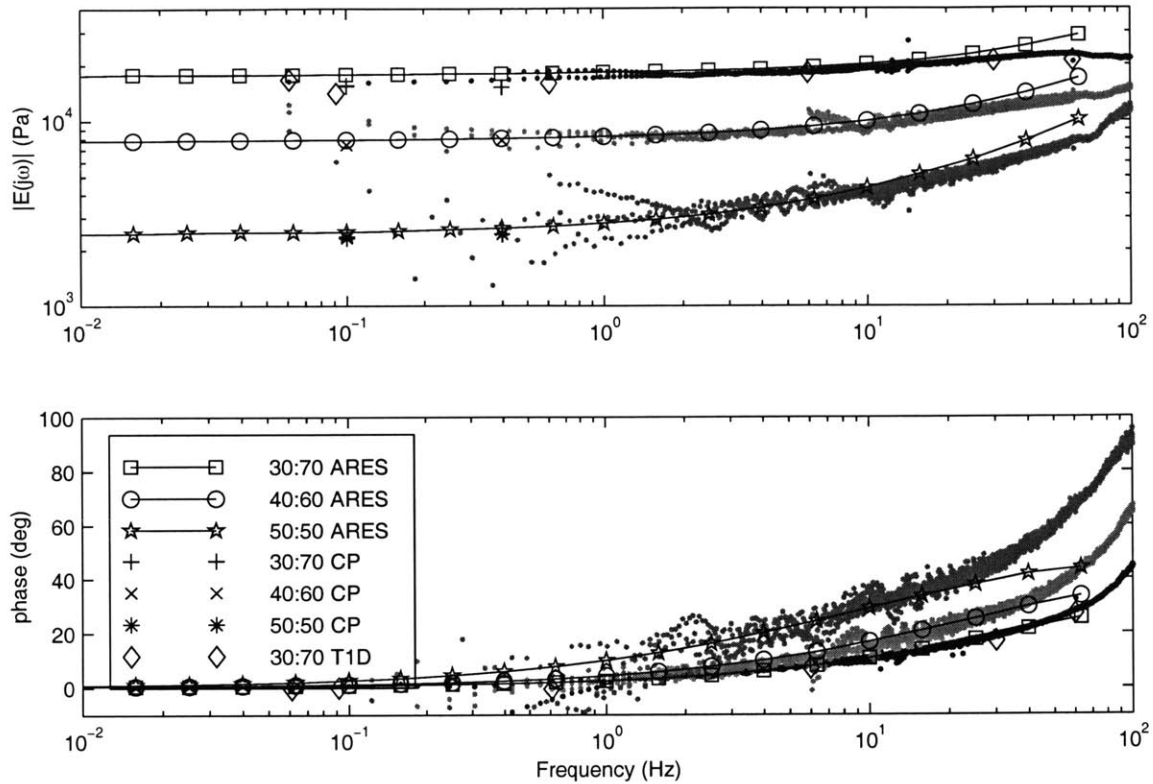


Figure 6-10: Elastic modulus of RTV samples. Includes TeMPeST 1-D chirp, parallel plate rheometer (ARES), cartilage press (CP) data and TeMPeST 1-D fixed frequency sinusoidal response (30:70 sample only).

results from the ARES tests and the CP indentation tests for comparison. The shear modulus ARES data were converted to Young's modulus form using equation 6.8, and an assumed value for  $\nu$  of 0.5<sup>6</sup>

$$E = 2(1 + \nu)G \quad (6.8)$$

There is good agreement between the TeMPeST 1-D and CP tests at low frequencies, showing that even on materials with more complex behavior than lumped elements, the TeMPeST 1-D can reliably measure the same force-displacement response as other systems with the same test geometry. The ARES and TeMPeST 1-D

<sup>6</sup>Provided that  $\nu \geq 0.45$ , E will be overestimated by 3.5% at most

results also correspond well, again especially over frequencies away from the system resonance. This is encouraging, demonstrating that the same properties are measured using two entirely different testing methods.

The small disagreement between the testing methods can have a number of sources. As discussed in the previous section, idealized approximations for a rigid indenter impinging on an elastic medium exist. However, the true experiments do not necessarily meet all of the assumptions used to derive them. For example, the assumed pressure distribution predicts infinite stress at the edges of the indenter [19] and implies a sharp discontinuity in the slope of the surface at the edges, which is clearly non-realistic. In addition, the theoretical development assumed that there was frictionless contact between the indenter tip and the material, which may not be entirely valid, even with the use of the instrument oil.

The largest contribution is likely distortions introduced by the TeMPeST 1-D as the excitation frequency approaches resonance.

## 6.4 In Vivo Solid Organ Measurements

*In vivo* experiments were conducted to test the performance of the TeMPeST 1-D under the conditions of the operating room. An experimental protocol for tests on porcine organs was developed in cooperation with the Animal Resources Center at Dartmouth College, and was approved by the Institutional Animal Care and Use Committee at Dartmouth as well as by the Committee on Animal Care at M.I.T. These tests were performed as an extension to a surgical training protocol, so no additional pigs were used to acquire the data.

Four female Yorkshire pigs<sup>7</sup> were being used for other laparoscopic or open surgical investigations. Anesthesia was induced with 20mg/kg ketamine and 2mg/kg xylazine via intra-muscular injection. 0.04mg/kg atropine was also administered to reduce bradycardia and salivation. The animals were intubated and placed on assisted ventilation using 100% oxygen, with 1-5% halothane or isoflurane to maintain

---

<sup>7</sup>Parson's Farms, Hadley, MA, all approximately 30 kg, fasted overnight

an adequate plane of anesthesia. The animals' depth of anesthesia was monitored continuously by observing heart and respiratory rate, as well as jaw tone and corneal reflex. An intravenous catheter was maintained to administer fluids, and injectible anesthetics and analgesics were available on hand in case depth of anesthesia could not be deepened rapidly enough using only inhalant anesthesia. The base protocol, for which the tissue property measurements were an extension, called for euthanasia of the animals before recovery from anesthesia, accomplished with concentrated KCl solution administered intravenously or by intracardiac injection.

#### **6.4.1 Laparoscopic testing**

In the cases when the tests were performed laparoscopically, the abdominal cavity was insufflated with carbon dioxide, to provide a working space within the body. A 12mm cannula was placed subumbilically and a 30° laparoscope was inserted. Other cannulas were inserted under visual guidance in different locations depending on the procedures scheduled, including at least one other 12mm cannula.

After completion of the surgical exercises, all tools except for the laparoscope were removed. The TeMPeST 1-D, attached to the Mediflex arm was inserted through the second 12mm cannula (see figure 6-11), and under guidance from the laparoscope, the tip was brought to within one half inch of the surface of either the liver, or the spleen, depending on the test being performed. While difficult due to the limited depth perception available through the laparoscope view, positioning of the TeMPeST 1-D perpendicular to the tissue surface was attempted to provide conditions as close to ideal as possible. In addition, as much as possible, contact was made in regions overlying the thickest sections of the organs, again to approximate the semi-infinite body approximation described in section 2.2. The flexible arm was locked in position, and the data acquisition program started.

Because of normal breath motions, the organs shift in response. This is especially true for the liver, which lies on the other side of the diaphragm from the chest cavity. This motion can drive the indenter tip to its limit of motion; to minimize gross motion of the organs caused by breathing, assisted ventilation can be suspended for



Figure 6-11: Exterior view of operating field for laparoscopic sessions

short periods of time. Because the pigs are breathing pure oxygen, their blood oxygen saturation is close to 100%, so this is less stressful than brief breath holding, and does not cause injury. During an approximately 20 second suspension of ventilation, the TeMPeST 1-D was brought into contact with the surface of the organ using the fine adjustment cam, vibration applied and force and position measurements were made. At the end of the measurements, ventilation was restored. Blood oxygen saturation was monitored throughout the testing, and was never observed to fall below 98%.

In addition to the force and displacement measurements, the video image from the laparoscope was recorded for later analysis. Figure 6-11 shows an exterior view of the pig's abdomen showing the TeMPeST 1-D in position and the laparoscope being hand-held in position. Figure 6-12 is a typical image of the view of the interior of the abdomen, with the indenter tip in the holding position before being brought into contact with the liver.

When appropriate, the laparoscope and the TeMPeST 1-D were swapped between ports to provide better access to the organs, or access to different organs. Details on the specific tests performed will be described in section 6.4.3.



Figure 6-12: Typical view of TeMPeST 1-D approaching contact with liver

#### 6.4.2 Open surgical testing

One session afforded the opportunity to take measurements during open surgery. In this case, an incision had been made along the midline of the abdomen, from below the sternum to the area of the umbilicus providing access to the surface of the spleen. While visible, very little of the liver was exposed, and then only the thin edges of the lobes, making highly suspect the “semi-infinite” assumption upon which the calculation of  $E$  is based. Open surgery permitted much simpler positioning of the TeMPeST 1-D with respect to the organs, and was recorded with a digital camcorder only. Data acquisition was performed in the same way as for the laparoscopic testing; positioning of the TeMPeST 1-D, holding ventilation, data acquisition and restoration of ventilation, all within a period of approximately 20 seconds.

Figure 6-13 shows an image of the TeMPeST 1-D in position over the spleen from the recording of the open surgical session.

#### 6.4.3 *In vivo* solid organ test results

As the surgical testing was to be a “trial-by-fire”, the learning experience was to be the most significant result. Some useful liver data were, however, obtained in the last

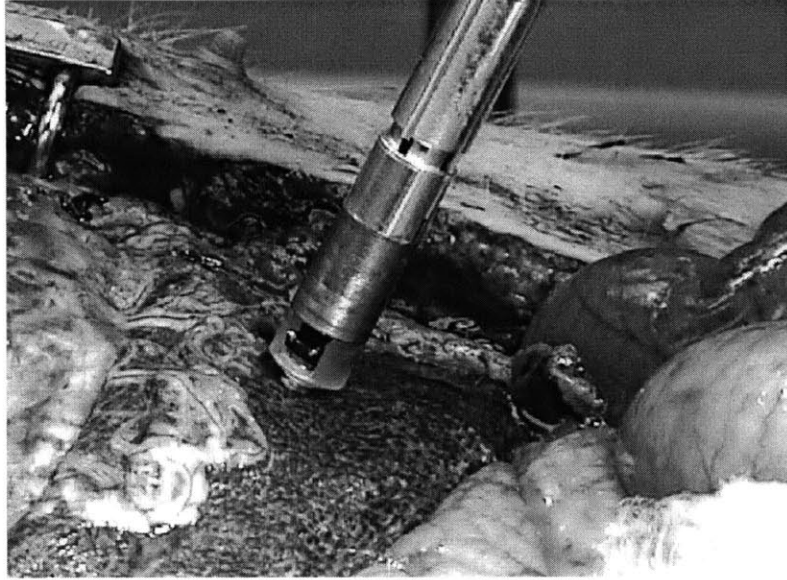


Figure 6-13: View of TeMPeST 1-D used during open surgical measurements of spleen operating room session, under laparoscopic conditions. The previous sessions served to guide a number of small modifications to the TeMPeST 1-D, some of which will be enumerated in table 6.4 and others discussed in chapter 7. The liver data obtained, and comments about the measured response follow.

Figure 6-14 shows the data for the last laparoscopic liver test, performed with a replacement force sensor.<sup>8</sup> Spleen data could not be taken during this session because the placement of the surgical ports did not allow sufficient access to the spleen. Additional testing was not possible due to time and animal lab scheduling constraints.

The elastic modulus is nearly constant over the range from 0.1 to 100Hz, increasing by less than a factor of two, and phase is approximately zero over the frequency range. The spike at 60Hz corresponds with electrical noise, and can be safely ignored. From these results, porcine liver can be approximated as an elastic material, with a Young's modulus of 10–15kPa. In comparing this with the survey of tissue properties of table 2.2, it falls within the range established by other measurements. While there

---

<sup>8</sup>The original force sensor was either damaged early in development or was defective, but was not detected as there was no basis for comparison at the time. The effect was to reduce the signal to noise ratio by roughly two orders of magnitude, compared with the replacement.



Table 6.4: Experimental parameters for *in vivo* tests of solid organs

Experiment	Notes
Laparoscopic 1	<p>liver:  right side port, above umbilical line  4 chirp sets, covering range <math>0.1 &lt; f &lt; 150\text{Hz}</math>  umbilical port  3 chirp sets, <math>0.1 &lt; f &lt; 150\text{Hz}</math></p> <p>spleen:  umbilical port  non-ideal approach  ◦ data degraded by force sensor noise problem</p>
Laparoscopic 2	<p>◦ increased size of indenter tip from 2.5 to 5.0mm to permit application of larger forces with same indentation depth  ◦ angled tip cover back to improve visibility of contact point</p> <p>liver:  7 chirp sets, <math>0.1 &lt; f &lt; 100\text{Hz}</math>  3 square wave tests: pulsatile motion due to cardiac action makes step tests difficult to interpret</p> <p>spleen:  6 chirp sets, <math>0.1 &lt; f &lt; 100\text{Hz}</math>  2 square wave tests: cardiac pulsation</p>
Open 1	<p>spleen:  11 chirp sets, <math>0.06 &lt; f &lt; 200\text{Hz}</math>  ◦ significantly simpler perpendicular alignment without restriction of fixed entry port</p>
Laparoscopic 3	<p>◦ acquired new force sensor with 100x lower noise</p> <p>liver:  7 chirp sets, <math>0.04 &lt; f &lt; 500\text{Hz}</math></p>

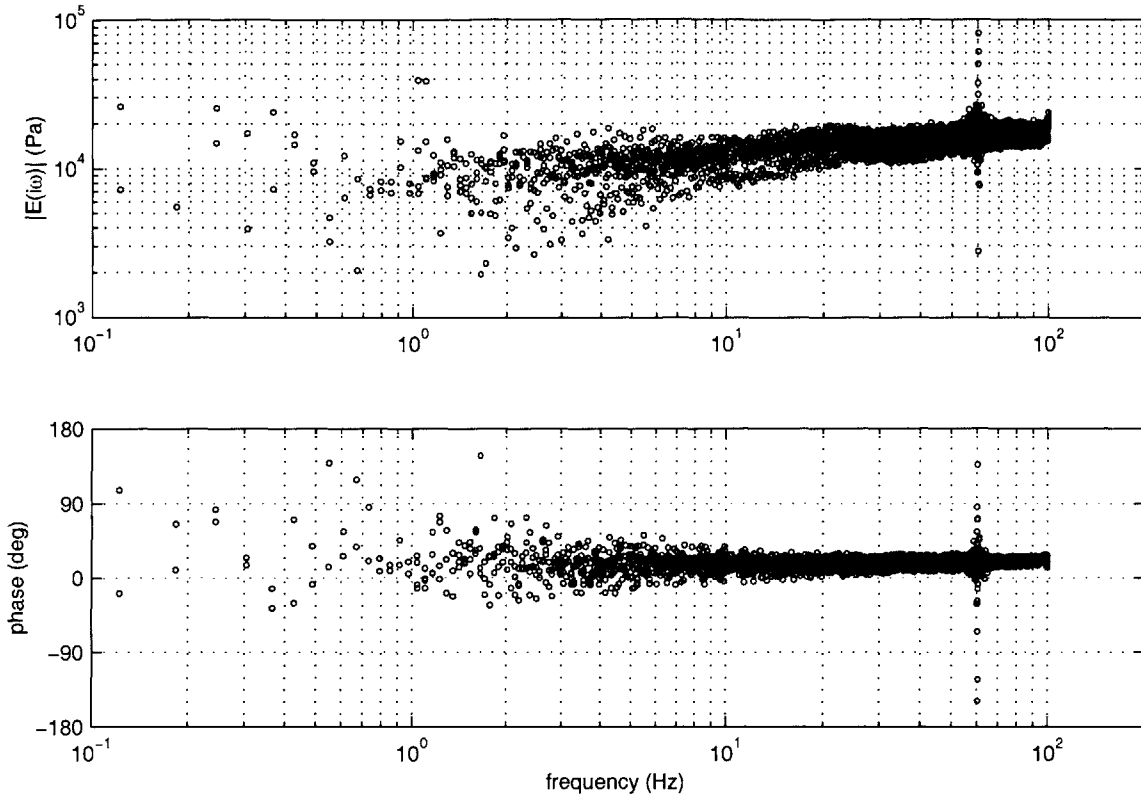


Figure 6-14: Non-parametric elastic modulus of liver. Spike at 60Hz is due to electrical interference in force signal.

is no reason to believe that rabbit, bovine and porcine liver should have the same properties, that the results are similar is valuable from a validation perspective.

Given the accuracy that was achieved with the silicone gel samples however,<sup>9</sup> the increase in modulus with frequency could be viewed as a reliable element of the response, so a more complex tissue model might be employed in simulation. Returning to the Kelvin model introduced in chapter 2, this response might be characteristic of the regime slightly below the transition frequency. If the TeMPeST 1-D was modified to examine frequencies up to about 1kHz, or a different instrument employed, this behavior could be verified. Further comments on the performance of the device and directions for future research will be discussed in the next chapter.

---

<sup>9</sup>especially the medium and hard samples, with stiffness on the same order calculated for the liver

# Chapter 7

## Contributions, Discussion and Further Directions

### 7.1 Summary

The Tissue Material Property Sampling Tool, or TeMPeST 1-D, was conceived to address the need for data on the properties of living organs, to support high fidelity surgical simulation systems. Such systems will eventually become part of the medical curriculum, and have applications beyond the training of new surgeons, such as prototyping of new medical instruments and procedures with reduced use of animal testing.

A key requirement of simulation systems is the availability of accurate models of tissue behavior, and these in turn, depend on measurements of the mechanical properties of living tissue. Some of the simpler models and their parameters were presented in chapter 2. Given the assumption of a particular tissue model, means for extracting the parameters from measurements of applied force and displacement were presented. To provide guidance on the kinds of responses to expect, some of the available literature on tissue properties was investigated, and typical results presented.

Chapters 3 through 5 illustrated the development of the first minimally invasive surgical instrument to look specifically at the frequency response of solid organ tissues.

Given the constraints of the minimally invasive environment in which this device

was meant to be used, and the selection of normal indentation of the tissue surface as a measurement mode, a series of potential design options were considered, converging on a design in which the sensors and actuator are co-located at the tip of the surgical instrument. This design presented several challenges, including the design of a system that could fit within a 12mm envelope, complete with a novel voice coil actuator, and position and force sensors. The design also permits separation of the sensor/actuator package from the amplifier electronics so that it can be sterilized.

Theoretical models, ranging from a second order spring-mass-damper approximation to the system, to a more complete model including contact with tissue and a compliant support structure were developed in parallel with the designs, providing some estimates on performance. The models were also used to demonstrate the relationship between the measurements that would be taken and the parameters of the tissue models presented earlier. The system models were populated with the parameters of the real TeMPeST 1-D through a series of calibration experiments, which included investigations of the static and frequency responses of the sensors and actuator. These experiments permitted the determination of the filtering characteristics of the TeMPeST 1-D, so that measured tissue frequency responses could be corrected for known measurement artifacts.

A graphical user interface was also developed to support the use of the TeMPeST 1-D. It includes means to generate a variety of waveforms which can be used to stimulate the tissue to examine different kinds of responses. Time domain response can be studied with square waves, while the frequency domain can be examined with either fixed frequency sine waves, or chirp signals, which have frequency content spread over a range of interest. A real-time control system was developed to drive the TeMPeST 1-D and acquire force and position data at frequencies up to 2kHz. The output of the system is in the form of force and position trajectories, as well as non-parametric, graphical representations of the tissue properties calculated from the FFTs of the force and position signals.

Through the course of testing on materials with independently measured responses, including springs, masses and silicone gel samples, the ability to accurately

measure force-displacement data was demonstrated. The final phase of the work, namely taking the system into the operating room, demonstrated both the capabilities and the limits of the device, and yielded preliminary data on the elastic properties of porcine liver *in vivo*. The elastic modulus was found to be approximately 12.5kPa, and nearly constant over the frequency range from 0.1 to 100Hz. These data represent perhaps the first frequency response data for porcine liver *in vivo*. The capabilities of the TeMPeST 1-D suggest directions for further development, and its successful use in the operating room is one of the first steps in filling in a comprehensive atlas of the mechanical properties of living tissues.

## 7.2 Instrument and measurement comments

As a functioning prototype for measuring tissue properties, the TeMPeST 1-D, has satisfied many of the criteria that were laid out for it. It is a minimally invasive instrument, so it can be used to sample living tissue properties with minimal trauma, or can be used in open surgery when such opportunities arise.

A number of areas where improvements can be made include the following:

### Perpendicular orientation with respect to tissue

Indentation testing involves making a number of geometric assumptions, including, in this case, perpendicular indentation and semi-infinite extent of the tissue. Positioning of any laparoscopic tool is limited by the fulcrum action of the port through the abdominal wall. As a result, while the tip can be arbitrarily positioned, the pitch and yaw angles of the tip are completely constrained. For example, on an organ with a curved surface, perpendicular contact is only possible at a point where the surface normal vector passes through the pivot location of the cannula. Clearly, creating multiple entry points for many cannulae would be impractical (and not necessarily justifiable) for animal testing. If human tests were to be performed during an operation, they would likely be limited to only those ports needed for the operation.

Adding an “elbow” joint to the shaft of the tool, and making use of the roll axis

of the tool would permit positioning of the tip in five degrees of freedom, sufficient to enable perpendicular contact at any point. Since the tool tip is axisymmetric, it is not necessary to control the roll orientation of the tip. Endoscopes and a number of other minimally invasive instruments are steerable in this manner, and the existing TeMPeST 1-D has significant unused space in the tool shaft so the implementation of an actuated elbow is possible, whether through a manually controlled linkage or a servo controlled joint. One issue that would need to be taken into account in such a system would be the limited space in the abdomen, and the length of the cannula—in the experience of the operating room tests that were performed, often less than one inch of the TeMPeST 1-D extended from the inner end of the cannula before contacting tissue.

### **Rejecting breathing and cardiac rhythm induced motion**

Another problem encountered was that of organ motion due to breathing. With a tool fixed to an external reference frame, breath and cardiac motion are superimposed on the motion due to the applied force. Since tissue may exhibit non-linear behavior under the larger deformations generated by such motion, and because the motion is typically not perpendicular to the axis of the indenter, the additional unmeasured motions can corrupt the measurements. Beyond that, in the case of the TeMPeST 1-D, the breathing motions could easily drive the indenter tip to the limits of its motion.

The solution that was used in these experiments was to suspend ventilation during data acquisition. The animal subjects, which were anesthetized and on ventilators, effectively had their breath held for periods of about 20 seconds, to eliminate breath motion. While harmless to the animals, approval for such a technique would be less likely for human testing.

Cardiac motion was present in the measurements, but by looking at the ratio of FFT's of the position and force, this motion did not appear to affect the calculation of the tissue frequency response. It did, however, make time domain data (from step responses) impossible to interpret.

Decoupling the sensor/actuator package from the external frame could solve the breath motion problem. One solution might make use of a pair of force sensors mounted on a pivot (see figure 7-1). The force sensors would contact the tissue, with a preload applied by an air-bearing mounted carriage. Driving oscillations at the pivot would generate normal indentation of the tissue at both locations, with differential and mean force and differential position as the outputs. Because the pre-loaded carriage would not be rigidly mounted to the external frame, the pivot-mounted sensors would follow the organ motion, and the differential values would provide the desired data.

A more radical approach to decoupling might be to deliver a voice coil or piezo-buzzer package connected to an accelerometer directly to the surface of an organ on the end of a minimally invasive instrument, and deposit it there. The accelerations due to vibration would be measured, and compared with the applied force of the buzzer. Since the response would be modulated by the impedance of the tissue, the impedance of the tissue alone could be separated from the response of the buzzer-package alone. Since the hardware would be mounted directly to the surface of the tissue, gross organ motion would not affect measurements made relative to the surface of the organ.

### **Signal generation and processing**

As was seen especially in the liver data, the use of the ratio of force and position FFTs can introduce significant noise into the measured response of the tissue. This can be reduced by extending the length of time over which sampling is performed, but this conflicts with the limits on the safe length of time during which animal breathing was suspended. The other option is to conduct more tests, each over a short period, so in a more comprehensive protocol, the chirp techniques used might be discarded in favor of performing sine wave responses over a series of fixed frequencies. When such techniques are used, there are powerful tools available to isolate responses only at the desired frequencies (including some which can be implemented in analog hardware). The scope of the current work did not extend to all of the issues involved

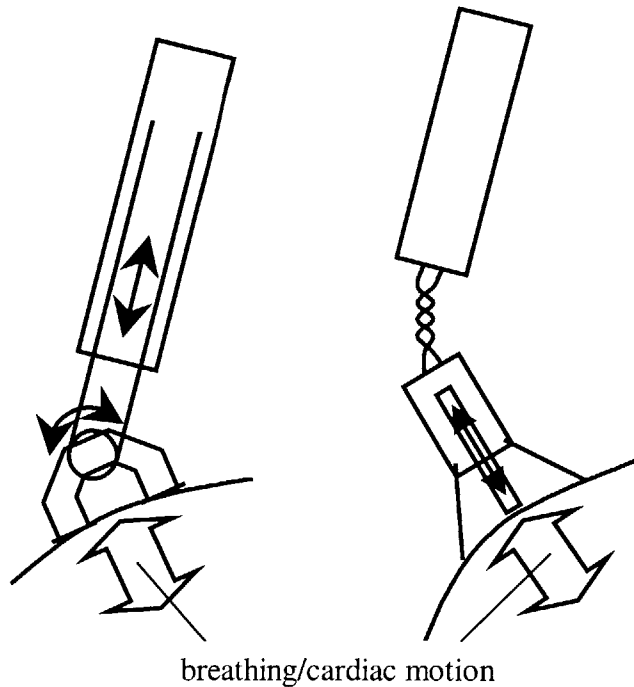


Figure 7-1: Pivot-mounted force sensors with torsional actuator, riding on air-bearing supported carriage (left) deployable, surface mounted sensor/actuator package (right).

in signal processing, but they must be considered before beginning work to acquire more comprehensive sets of data.

Related to this is the choice of data acquisition hardware, and the physical characteristics of the actuator. As was found, at frequencies approaching the resonance of the device, the measured responses begin to deviate from the ideal. One way to extend the range of use of the device would be to increase its resonant frequency. This can be done by stiffening the suspension<sup>1</sup>, or by reducing the mass of the actuator. There are a number of areas where this could be accomplished, but for a significant increase in bandwidth, significant reductions in mass would be necessary. Optical position measurement (e.g. by laser interferometry) could eliminate the mass of the LVDT core and the elements connecting it to the rest of the actuator (about 25% of total), and the force sensor could be replaced with a layer of piezo-electric film (another 15% or so). Further redesign could reduce mass by a total of 50% or more.

---

<sup>1</sup>which can be done by choosing a flexure with a shorter cantilever—the series of flexures that were photo-etched provide a range of stiffnesses.



The phase lag introduced by the lag between position and force sensing could be eliminated through the use of other data acquisition systems, which might also have higher sampling frequencies. However, if human perception cannot distinguish high frequency phenomena very well, then increasing the bandwidth significantly may not be necessary.

## **Experimental protocol**

Because the *in vivo* testing was performed as an extension to an existing protocol, tests on tissue could only be performed during breaks in, or after, prior tests. As a result, testing time was limited, and the approaches to different organs were those determined by the procedure being performed.

Acquisition of a more complete set of data could proceed in two directions. The first would be a set of dedicated animal tests, in which the placement of cannulas was determined to achieve optimal access to the organs in question. In such tests, time would not be as limiting a factor as it was, and sufficient tests could be performed to achieve results with lower uncertainty than was the case shown in chapter 6. As mentioned in reference to signal processing, a series of fixed frequency sinusoids could be performed using the full “breath-hold” period for each frequency.

In addition, with the ability to define the locations for insertion, one could begin to generate a map of the variation of tissue properties across the organs, leading to information about homogeneity. Such tests could also serve to populate a “look-up” table of local stiffnesses, to support some real-time simulations that use simpler schemes than FEM to generate the force-displacement response. In conjunction with this sort of experiment, more detailed descriptions of the geometry of the organ should also be acquired. By using MRI (or other imaging technique) to reconstruct the three-dimensional structure of the organs, better estimates of the geometric factors involved in the conversion from force and displacement to elastic moduli could be made.

The alternate, and ultimately preferred direction, is to redesign the tool so that it would be suitable for use in human testing. Among the changes would be: something like the elbow joint, described above, so that available access ports would be

acceptable, or the use of an alternative form of instrument which supports the same measurements; and reduced instrument diameter, especially since the trend in minimally invasive surgery is to use narrower instruments, so opportunities for sampling with a 12mm tool would grow fewer and fewer. Human experiments should be guided by such issues as the psychophysics of touch, in that there are limits to human perception, so experiments might not need to be done that provide information beyond that level.

### 7.3 Future work

At the outset of this work, development was begun on two tools, which were to be used in complementary fashion. The TeMPeST 1-D was the first, and was to be used to acquire the linear properties of tissues. As shown, it was completed, and can perform this task well.

The second tool, called the TeMPeST 3-D, was intended to look at how tissue responds to larger scale deformations, as might be imposed by a blunt probe, and look at motions in arbitrary directions. A CAD drawing of the concept for the TeMPeST 3-D is shown in figure 7-2.

The TeMPeST 3-D, in its current embodiment, would make use of a cable drive system to cause the blunt probe at the tip to move in pitch and yaw, and would translate an inner carriage along the axis of the tool to provide motion along the  $z$ -axis. The volume of the workspace would be approximately one cubic inch.

Where the TeMPeST 1-D was an instrument for acquiring tissue properties, the TeMPeST 3-D would be useful as a validation tool. For example, one could generate a pre-programmed sequence of motions with the TeMPeST 3-D and record the reaction forces of the tissue. If the geometry of the whole organ and its surroundings were determined (e.g. by MRI), an organ-specific simulation could be generated, using the tissue properties previously determined by the TeMPeST 1-D, or other devices. By simulating the same sequence of motions that the real TeMPeST 3-D had imposed on the tissue, one could generate a set of reaction force data that could be compared



Figure 7-2: Concept for large-scale, 3-D motion force-displacement probe, the TeMPeST 3-D.

with the real data. In this way, the loop of measuring tissue compliance, generating tissue properties, and simulating organs, is closed through validation measurements made by the TeMPeST 3-D. In this way, the verisimilitude of a simulation can be evaluated long before a surgeon uses a simulation only to find that some aspect of the response differs significantly from reality.

Additional images of the components of the TeMPeST 3-D are included in appendix C. As many of the physical components were acquired during the course of this work, it is very likely that the TeMPeST 3-D will be completed in the near future.



# Appendix A

## Nomenclature

variable	definition	units
$\delta$	phase	rad
$\delta_z, \delta_x$	indentation, shear displacement	m
$\epsilon$	strain	
$\zeta$	damping ratio	
$\omega$	angular frequency	rad·s <sup>-1</sup>
$\omega_m, \omega_d, \omega_n$	maximum phase, damped natural, natural frequency	rad·s <sup>-1</sup>
$\nu$	Poisson ratio	
$\rho$	density	kg·m <sup>-3</sup>
$\sigma$	stress	Pa
$\tau$	torque	N·m
$\tau_c, \tau_r$	creep, relaxation time constant	s
$a$	indenter radius	m
$A$	area	m <sup>2</sup>
$b$	damping coefficient	N·s·m <sup>-1</sup>
$B$	magnetic flux density	T
$c$	spring compliance	m·N <sup>-1</sup>

variable	definition	units
$E, E_l, E_h,$	Young's (elastic) modulus, low & high asymptotes,	
$E(i\omega), E_e, E_d$	complex, elastic, dissipative	Pa
$f, f(t), F, F(s)$	force	N
$f_{coil}, f_{meas}, F_{coil}, F_{meas}$	voice coil output, measured force	N
$f_z, f_x$	indentation, shear force	N
$f_0, f_1$	initial, final frequency	Hz
$G$	shear modulus	Pa
$h$	gel sample thickness	m
$H_m, H_v, H_k$	Maxwell, Voigt and Kelvin body transfer functions	
$I(t), I_0, I_1$	electric current, offset, amplitude	A
$k$	spring constant	$\text{N}\cdot\text{m}^{-1}$
$k_r$	relaxed stiffness	$\text{N}\cdot\text{m}^{-1}$
$K$	semi-infinite layer correction factor	
$K_b$	adiabatic bulk modulus	Pa
$l, l_0$	length, original length	m
$m, M$	mass	kg
$P$	power	W
$R$	resistance	$\Omega$
$\mathcal{R}$	characteristic radius	m
$t$	time	s
$v$	velocity of sound	$\text{m}\cdot\text{s}^{-1}$
$V$	voltage	V
$x, x(t), X, X(s)$	position	m
$x_{meas}, x_{lvdt}, X_b$	position: measured, LVDT, base	m
$\dot{x}, \dot{x}(t)$	velocity	$\text{m}\cdot\text{s}^{-1}$
$\ddot{x}, \ddot{x}(t)$	acceleration	$\text{m}\cdot\text{s}^{-2}$
$z, Z, \mathbf{Z}$	indentation depth	m

# Appendix B

## Flexure masks and etch sequence

The flexures used to support the moving coil in the actuator were fabricated by isotropically etching aluminum. Figure B-1 shows a sheet of flexures with a series of stiffnesses, the softest of which is approximately 100N/m. The details of the top and bottom post-etched surface features are shown in figure B-2, and the full mask set is shown in figure B-3. Note that the masks that were created by the manufacturer (Microphoto, Inc., Roseville, MI) and used to create the flexures are mirror images of the designs shown here.

Also included in the masks are the patterns used to make the cantilever elements for a 1-axis force sensor (see figure 3-7c) which was not completed in favor of the Cooper Instruments LPM 562 force sensor.

Figure B-4 shows the sequence of photomask application and isotropic etching through the aluminum, as well as how the thin cantilevers were preserved during the etch.

Figure B-5 shows a CAD model of the flexures. The CAD package used (I-DEAS master series 7, SDRC) could not generate all of the curved surfaces resulting from isotropic etching, but the image shows the essential features of the flexures used in the TeMPeST 1-D.

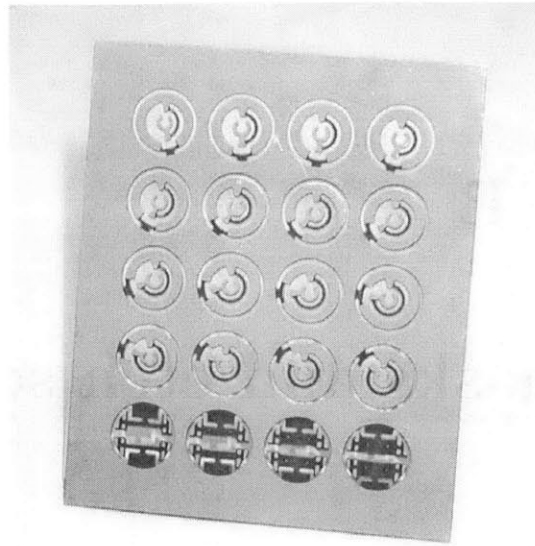


Figure B-1: A completed sheet of flexures. The stiffest flexure is at the top left, the softest at the lower right. Flexures forming the fixed-fixed cantilever beams of a 1-axis force sensor occupy the bottom row.

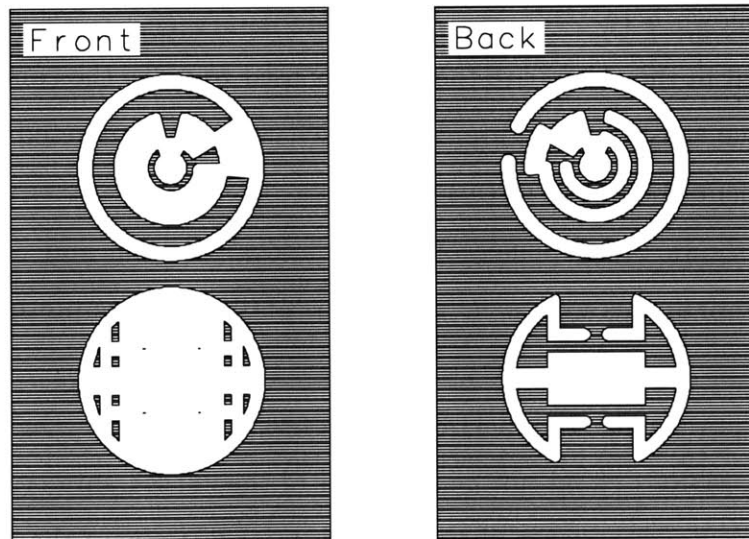


Figure B-2: Front and back sides of typical suspension and force sensor flexures, post-etching (from lower left corner of flexure sheet in figure B-1). Front side shows boss surfaces for clamping to TeMPeST 1-D body and core, back side shows cantilever and break-out tabs.



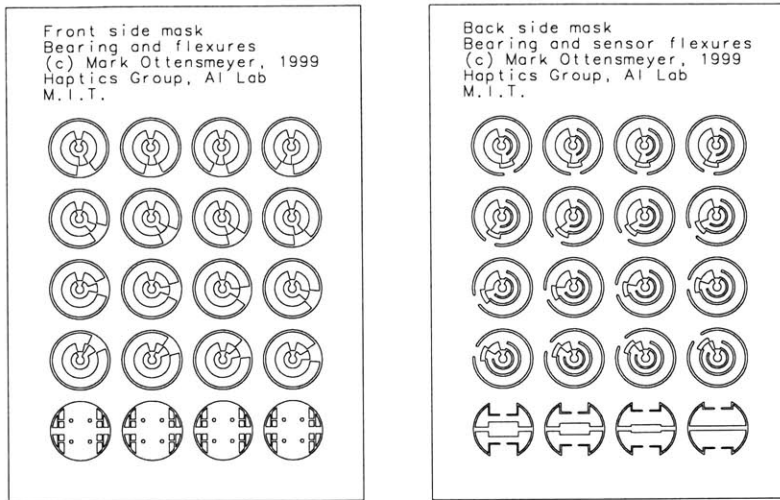


Figure B-3: Complete set of masks, used to generate a series of flexures with different stiffnesses and cantilever beam elements for 1-D force sensor.

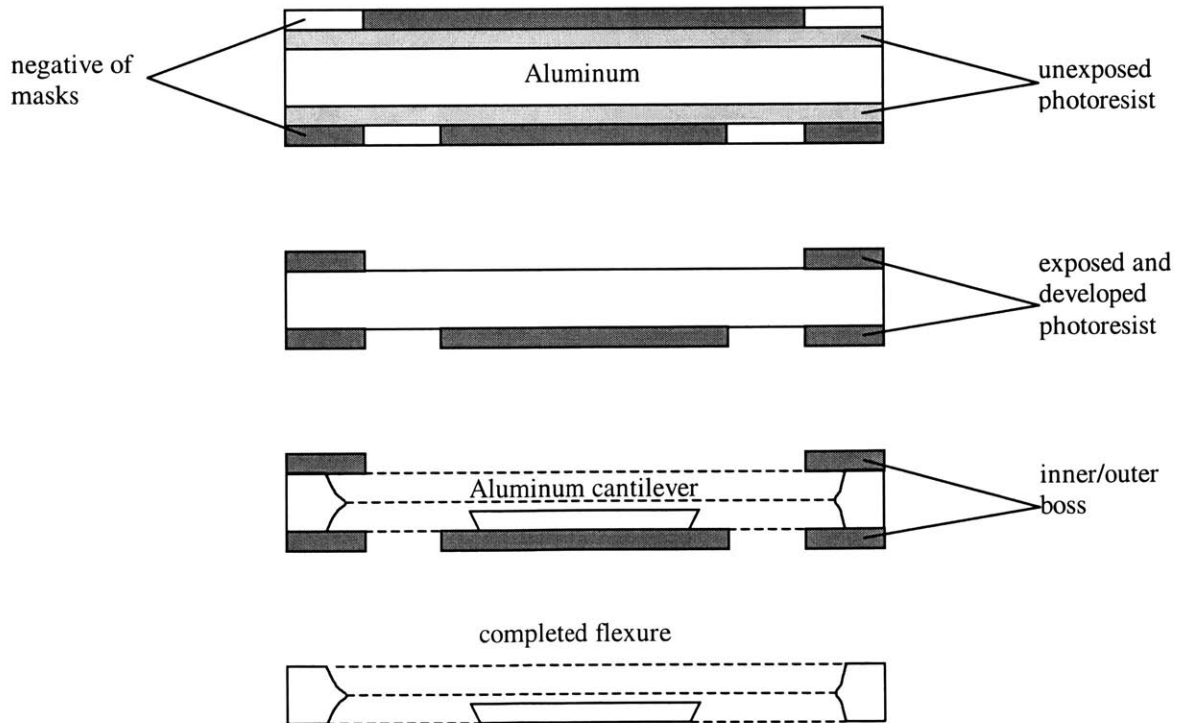


Figure B-4: Photomask and etch sequence for generating flexures

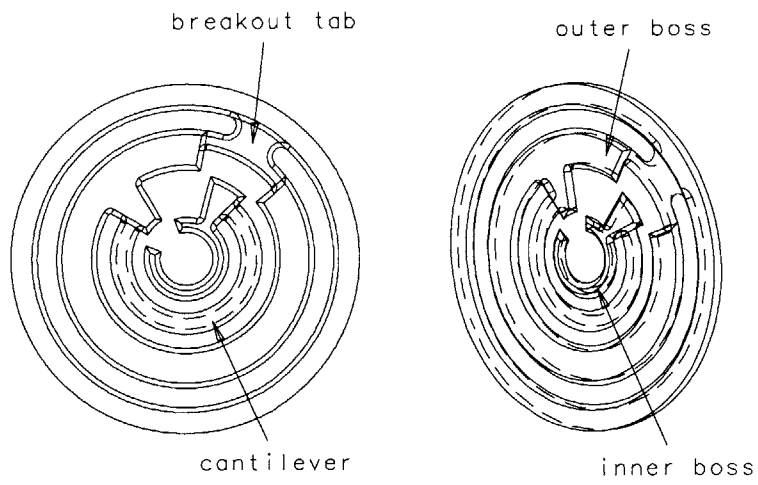


Figure B-5: CAD model of the etched flexures. Note thinner cantilever and break-out tab regions.

# Appendix C

## TeMPeST 3-D

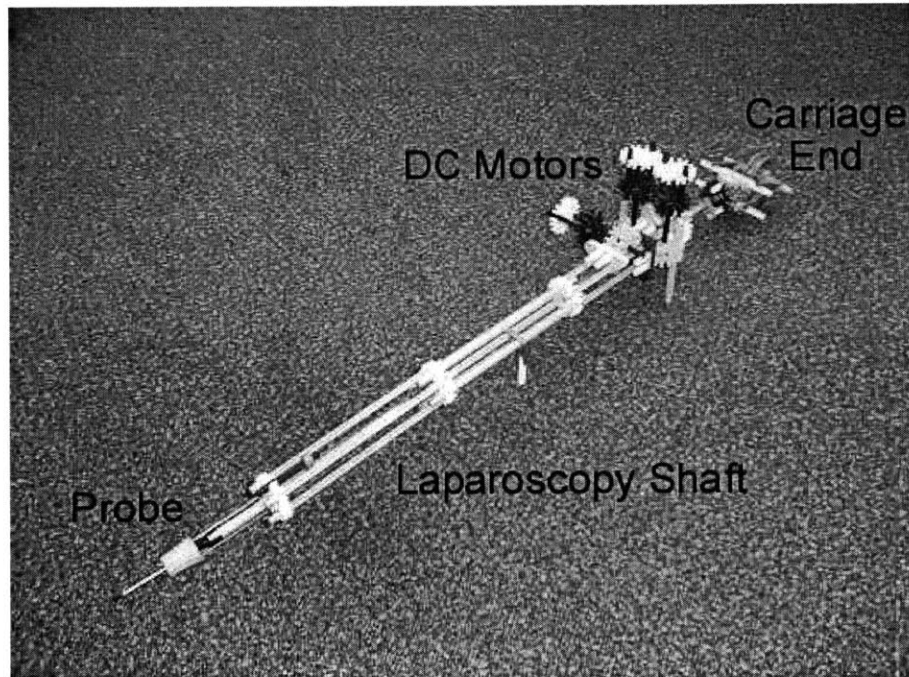


Figure C-1: An early conceptual model for the TeMPeST 3-D. Apart from computer control, this model demonstrated an early concept for the cable drive, with motions in the pitch, yaw and thrust directions.



Figure C-2: A more fully fleshed out version, including motors at the base, a universal joint near the tip, and a 3-axis force sensor behind the blunt probe. Position sensing in this version is done with the encoders on the motors, but redundant sensors closer to the tip would improve accuracy.



Figure C-3: Tip design for the TeMPeST 3-D. A universal joint permits motion in pitch and yaw, but prevents rotation of the tip about the shaft. Linear bearings in the sleeve support the axial motion of the tip. A novel 3-axis force sensor (pitch- and yaw-moment, and axial thrust) measures the reaction forces of the tissue.



Figure C-4: Cable drive system for the TeMPeST 3-D. The top motor controls pitch of the probe, the side motors are redundant in controlling yaw, and all together they move the central carriage along the shaft of the tool. Not shown are linear bearings which would support the shaft at the upper right, and lower left, as well as at the tip of the tube (see figure C-2).

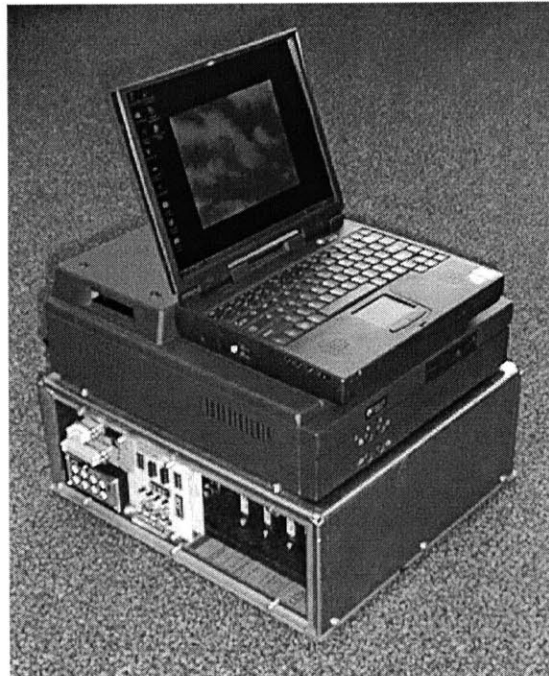


Figure C-5: TeMPeST-power: the interface box underneath the docking station houses a power source, PWM current amplifiers and interface circuitry to support the TeMPeST 1-D, the TeMPeST 3-D, and potentially other devices to be developed later.



# Appendix D

## T1Dgui

The functions of the graphical user interface for the TeMPeST 1-D are described in detail in chapter 5. The following figures show the T1Dgui with typical settings, and a series of output plots. These plots were generated with data acquired from measurements of one of the silicone gel samples.

With the settings shown in figure D-1, the program will generate a chirp signal with frequency increasing exponentially from 0.06 to 6 Hz, an amplitude of 200mA and an offset of 100mA. If the indenter tip is held in place, this corresponds with a force amplitude of 120mN and a 60mN offset. The sampling frequency is 500Hz, and a measurement window of 16.4s has been chosen.

Figures D-2 and D-3 are two auxiliary plots showing the instantaneous frequency vs. time, the output vs. instantaneous frequency, and the magnitude and phase of the FFT of the current that will be sent to the voice coil actuator.

Figures D-4 to D-8 are output plots generated after the real-time data acquisition program has returned control to the graphical user interface.

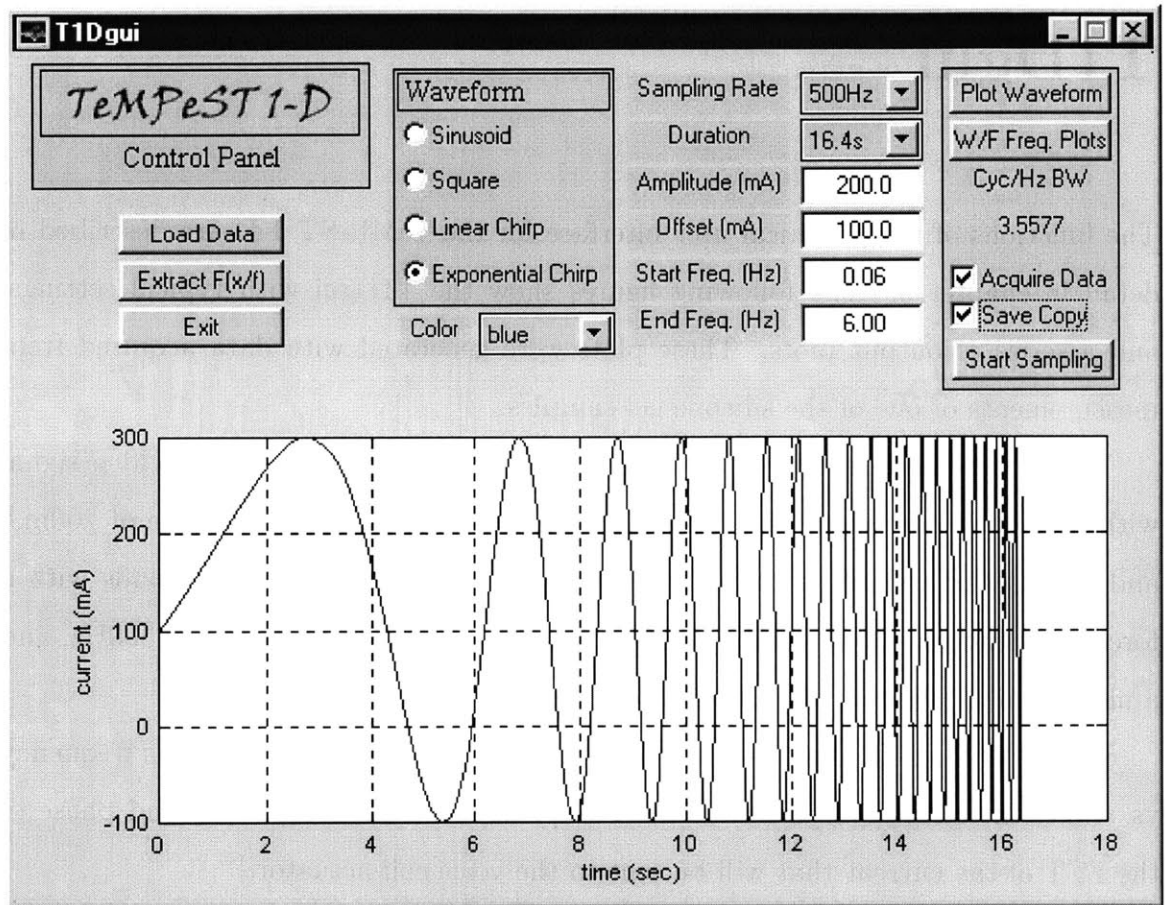


Figure D-1: The TeMPeST 1-D graphical user interface.



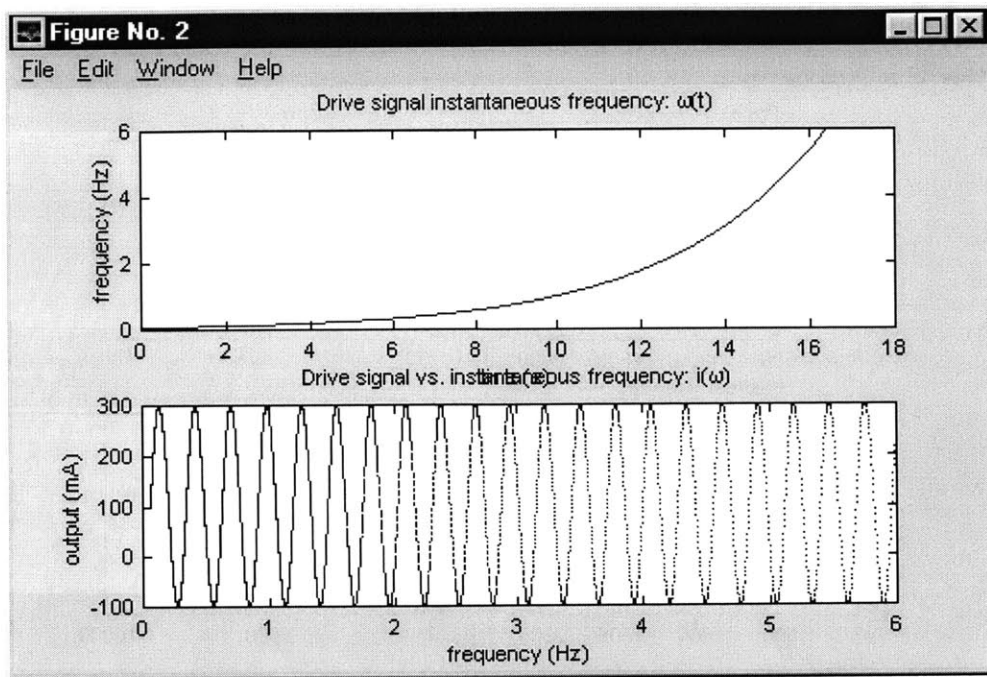


Figure D-2: Instantaneous frequency of chirp vs. time and drive current vs. instantaneous frequency.

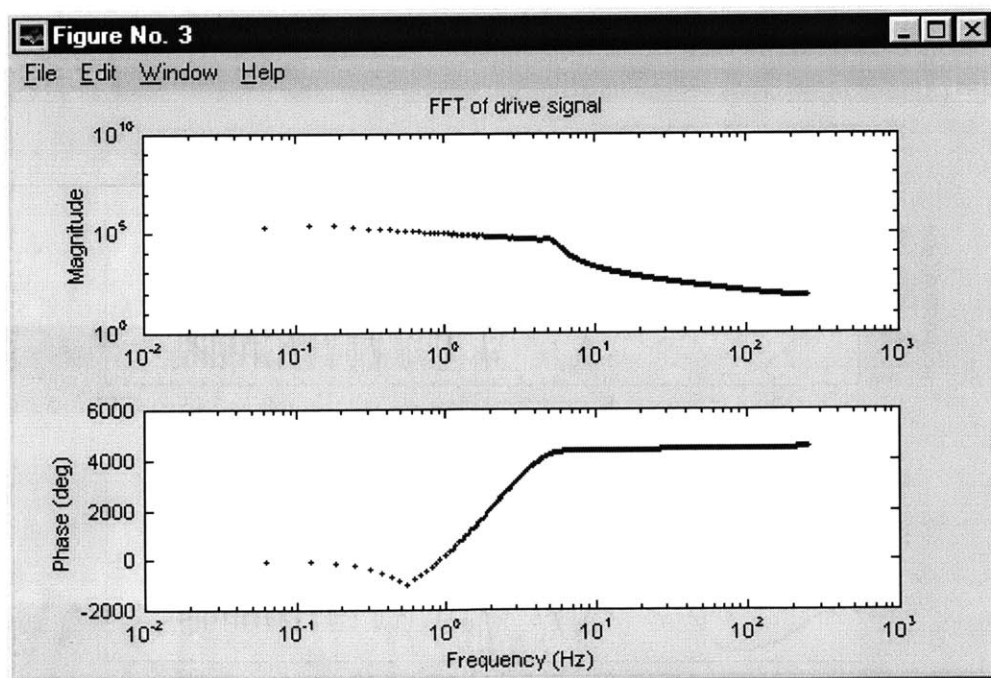


Figure D-3: Fast Fourier transform of the drive current signal. For linear chirp, transform has flat magnitude within chirp frequency range. For exponential chirp,  $\log(\text{magnitude})$  falls with a slope of -0.5 with respect to  $\log(\text{angular frequency})$ .

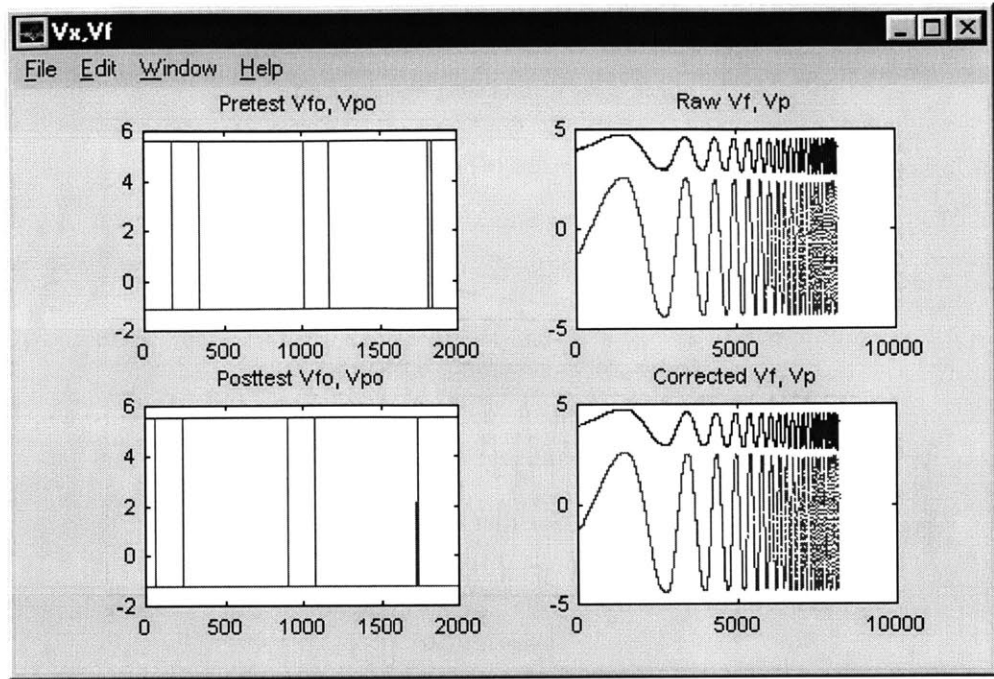


Figure D-4: Raw voltage output from the TeMPeST 1-D, including pre- and post-measurement offset voltages (upper and lower left). Upper traces in each plot are force sensor voltage, lower traces are LVDT voltage.

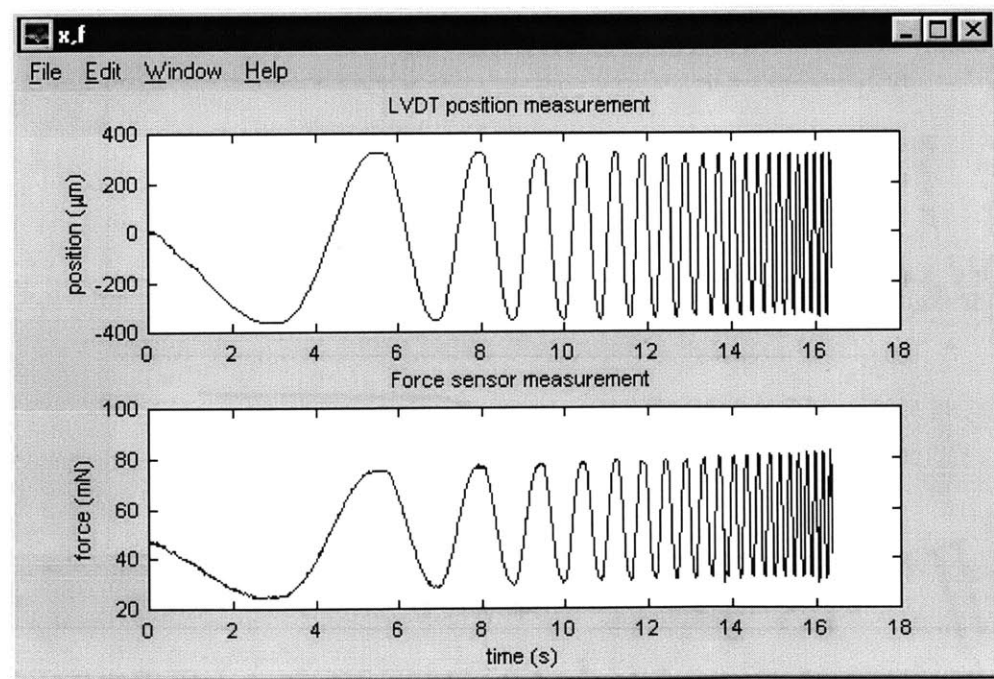


Figure D-5: Processed position and force signals. Position is positive for increasing indentation.

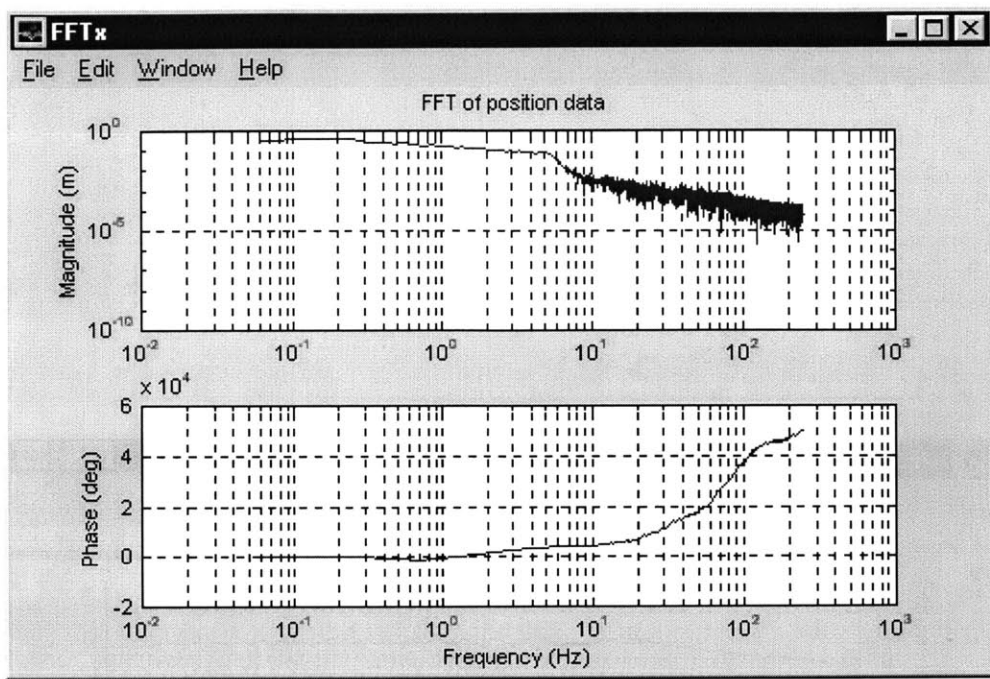


Figure D-6: Fast Fourier transform of position.

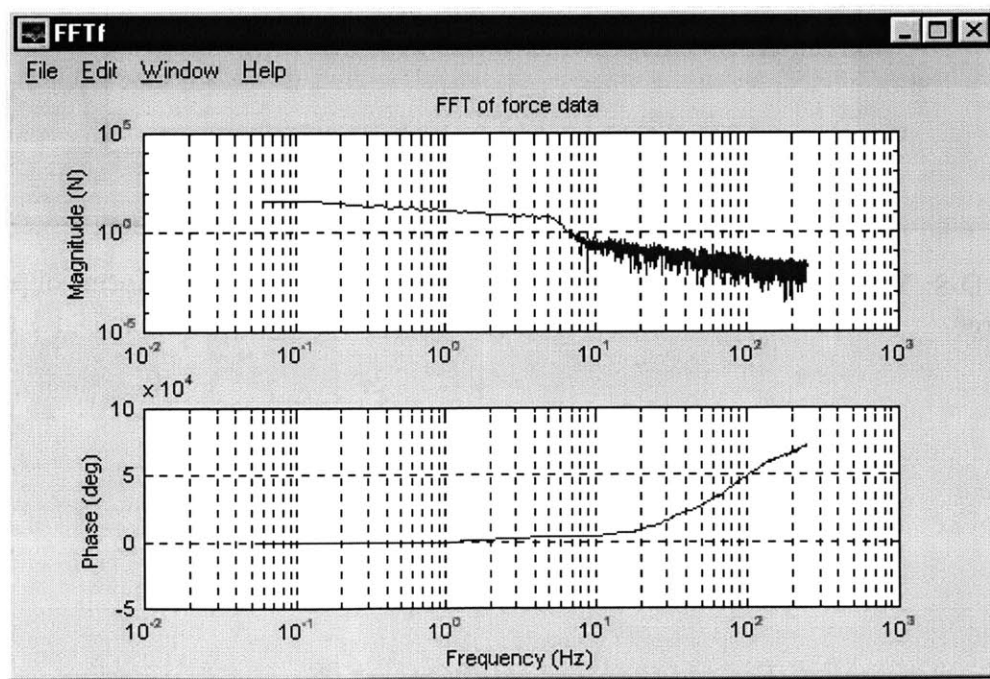


Figure D-7: Fast Fourier transform of force.

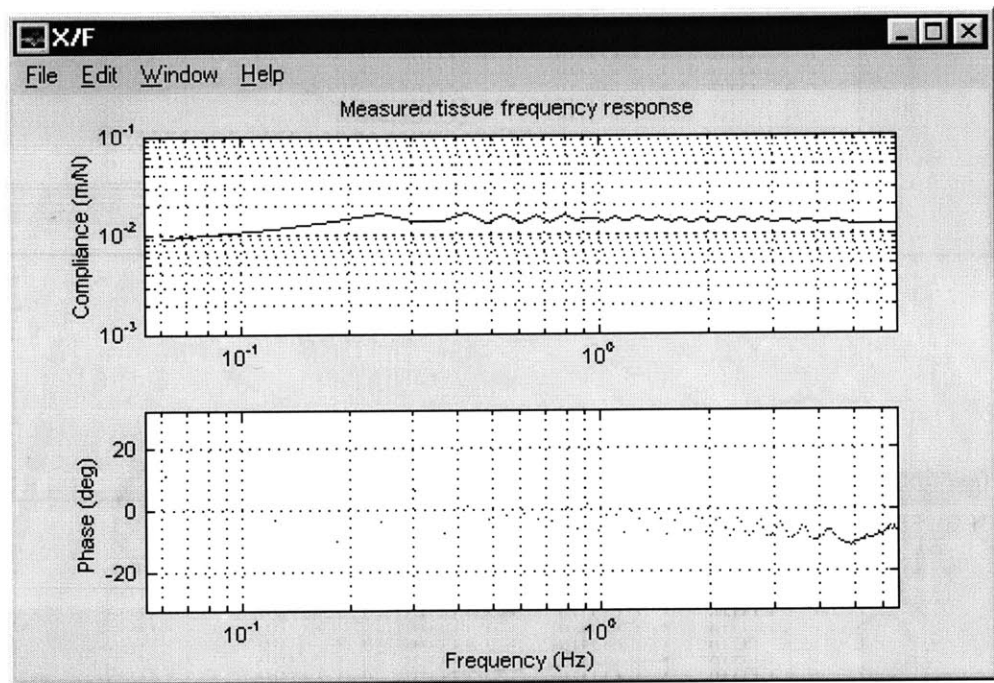


Figure D-8: Measured material compliance: ratio of fast Fourier transforms of position and force.

# Bibliography

- [1] Takahira Aoki, Toshiro Ohashi, Takeo Matsumoto, and Masaaki Sato. The pipette aspiration applied to the local stiffness measurement of soft tissues. *Annals of Biomedical Engineering*, 25:581–7, 1997.
- [2] Automation Creations, Inc. MatWeb, the online materials information resource. <http://www.matweb.com>, January 2001. last modified 21 December 2000.
- [3] A. Bicchi, D. De Rossi, and E.P. Scilingo. A haptic system for minimally invasive surgery: modelling control and perspectives. <http://www.piaggio.cci.unipi.it/surg+hap/sld007.htm>, 11 December 2000. last modified 19 November 1999.
- [4] Grigore C. Burdea. *Force and Touch Feedback for Virtual Reality*. John Wiley & Sons, Inc., New York, NY, USA, 1996.
- [5] Fiona J. Carter. Biomechanical testing of intra-abdominal soft tissue. Surgical Technology Group, University of Dundee. Workshop notes, Medical Image Computing and Computer-Assisted Intervention, MIT, Cambridge, MA, 11–13 October 1998.
- [6] Fiona J. Carter. Dundee single point compliance probe. <http://www.dundee.ac.uk/surgery/surgtech/compprobe/main.htm>, December 2000. last modified 19 April 1999.
- [7] Eric J. Chen, Jan Novakofski, W. Kenneth Jenkins, and Jr. William D. O'Brien. Young's modulus measurements of soft tissues with application to elasticity imag-

ing. *IEEE Transactions on Ultrasonics, Ferroelectrics and Frequency Control*, 43(1):191–4, January 1996.

- [8] Suvranu De and Mandayam A. Srinivasan. Thin walled models for haptic and graphical rendering of soft tissues in surgical simulation. In *Medicine Meets Virtual Reality*, pages 94–99, San Francisco, CA, 1999. IOS Press.
- [9] Francis A. Duck. *Physical Properties of Tissue: A Comprehensive Reference Book*. Academic Press, San Diego, 1990.
- [10] U.S. Federal Aviation Administration. *Federal Aviation Regulations, Part 141, Appendix B–Private Pilot Certification Course*. 1997.
- [11] Gene F. Franklin, J. David Powell, and Michael Workman. *Digital Control of Dynamic Systems*. Addison-Wesley, Menlo Park, CA, third edition, 1998.
- [12] Yuan-Chen Fung. *Biomechanics: Mechanical Properties of Living Tissues*. Springer-Verlag, New York, second edition, 1993.
- [13] Zorach R. Glaser. Special occupational hazard review with control recommendations for the use of ethylene oxide as a sterilant in medical facilities. Technical Report 77-200, National Institute for Occupational Safety and Health, Rockville, MD, August 1977.
- [14] Henry Gray. *Anatomy of the Human Body*. Lea & Febiger, Philadelphia, PA, twenty-seventh edition, 1959.
- [15] Blake Hannaford. Force reflecting endoscopic grasper. <http://rcs.ee.washington.edu/BRL/devices/surgical/freg.html>, 14 February 2000.
- [16] W.C. Hayes, L.M. Keer, G. Herrmann, and L.G. Mockros. A mathematical analysis of indentation tests of articular cartilage. *Journal of Biomechanics*, 5:541–51, 1972.
- [17] Paul Horowitz and Winfield Hill. *The Art of Electronics*. Cambridge University Press, New York, NY, USA, second edition, 1995.

- [18] Jørgen Arendt Jensen, Ole Holm, Lars Jost Jensen, Henrik Bendsen, Henrik Møller Pedersen, Kent Salomonsen, Johnny Hansen, and Svetoslav Nikolov. Experimental ultrasound system for real-time synthetic imaging. In *IEEE Ultrasonics Symposium. Proceedings*, pages 1595–9, Caesars Tahoe, NV, 17–20 October 1999. IEEE.
- [19] Kenneth Langstreth Johnson. *Contact Mechanics*. Cambridge University Press, New York, NY, 1985.
- [20] F. Kallel and M. Bertrand. Tissue elasticity reconstruction using linear perturbation method. *IEEE Transactions on Medical Imaging*, 15(3):299–313, June 1996.
- [21] Kistler Instrument Corp. On-line product catalog, parts 9207 and 9211. <http://www.kistler.com>, January 1 2001. last modified March 9, 1999.
- [22] H. Maaß and U. Kühnapfel. Noninvasive measurement of elastic properties of living tissue. In *CARS'99: Computer Assisted Radiology and Surgery, Proceedings of the 13th international congress and exhibition*, number 1191 in International congress series, pages 865–870, Paris, 23–26 June 1999. Elsevier.
- [23] J. Ophir, S.K. Alam, B. Garra, F. Kallel, E. Konofagou, T. Krouskop, and T Varghese. Elastography: ultrasonic estimation and imaging of the elastic properties of tissues. *Proceedings of the Institute of Mechanical Engineering, part H, Journal of Engineering in Medicine*, 213(H3):203–233, 1999.
- [24] K.J. Parker, L. Gao, R.M. Lerner, and S.F. Levinson. Techniques for elastic imaging: A review. *IEEE Engineering in Medicine and Biology*, 15(6):52–9, November/December 1996.
- [25] Jacob Rosen, Blake Hannaford, Mark P. MacFarlane, and Mika N. Sinanan. Force controlled and teleoperated endoscopic grasper for minimally invasive surgery—experimental performance evaluation. *IEEE Transactions on Biomedical Engineering*, 46(10):1212–21, October 1999.

- [26] Robert L.-Y. Sah, Young-Jo Kim, Joe-Yuan H. Doong, Alan J. Grodzinsky, Anna H.K. Plaas, and John D. Sandy. Biosynthetic response of cartilage explants to dynamic compression. *Journal of Orthopaedic Research*, 7:619–36, 1989.
- [27] Armen Sarvazyan, Mark E. Schafer, and Viktor Ponomarev. Method and device for measuring anisotropic mechanical properties of tissue. United States Patent 5,706,815, 13 December 1998.
- [28] Enzo Pasquale Scilingo, Danilo DeRossi, Antonio Bicchi, and Pietro Iacconi. Haptic display for replication of rheological behaviour of surgical tissues: modelling, control and experiments. In *Proceedings of the ASME Dynamics, Systems and Control Division*, pages 173–6, Dallas, TX, 16–21 November 1997. ASME.
- [29] Alexander H. Slocum. *Precision Machine Design*. Prentice-Hall, Inc., Englewood Cliffs, NJ, USA, 1992.
- [30] Mikio Suga, Tetsuya Matsuda, Jun Okamoto, Osamu Takizawa, Osamu Oshiro, Kotaro Minato, Sadami Tsutsumi, Izumi Nagata, Nobuyuki Sakai, and Takashi Takahashi. Sensible human projects: Haptic modeling and surgical simulation based on measurements of practical patients with mr elastography—measurement of elastic modulus. In *Medicine Meets Virtual Reality 2000*, number 70 in Studies in Health Technology and Informatics, pages 334–40, Newport Beach, CA, 27–30 January 2000. IOS Press.
- [31] Chikayoshi Sumi. Fine elasticity imaging utilizing the iterative rf-echo phase matching method. *IEEE Transactions on Ultrasonics, Ferroelectrics and Frequency Control*, 46(1):158–166, January 1999.
- [32] Chikayoshi Sumi, Akifumi Suzuki, and Kiyoshi Nakayama. Estimation of shear modulus distribution in soft tissue from strain distribution. *IEEE Transactions on Biomedical Engineering*, 42(2):193–202, February 1995.



- [33] Amanda Watson. Ultrasound equipment evaluation project. <http://www.gla.ac.uk/Acad/ClinPhys/UEEP/info.htm>, December 2000. last modified 15 December 2000.
- [34] Parris S. Wellman. *Tactile Imaging*. PhD dissertation, Harvard University, Engineering Sciences, May 1999.
- [35] Hiroshi Yamada. *Strength of Biological Materials*. The Williams & Wilkins Company, Baltimore, 1970.
- [36] Y.P. Zheng and A.F.T. Mak. Extraction of quasi-linear viscoelastic parameters for lower limb soft tissues from manual indentation experiment. *Journal of Biomechanical Engineering*, 121:330-9, June 1999.